Physics of the Nucleon Sea Quark Distributions

R. Vogt [1]

Nuclear Science Division, Lawrence Berkeley National Laboratory, Berkeley, CA 94720
and
Physics Department, University of California at Davis, Davis, CA 95616

Abstract

Sea quark distributions in the nucleon have naively been expected to be generated perturbatively by gluon splitting. In this case, there is no reason for the light quark and anti-quark sea distributions to be different. No asymmetries in the strange or heavy quark sea distributions are predicted in the improved parton model. However, recent experiments have called these naive expectations into question. A violation of the Gottfried sum rule has been measured in several experiments, suggesting that $\overline{u} < \overline{d}$ in the proton. Additionally, other measurements, while not definitive, show that there may be an asymmetry in the strange and anti-strange quark sea distributions. These effects may require nonperturbative explanations. In this review we first discuss the perturbative aspects of the sea quark distributions. We then describe the experiments that could point to nonperturbative contributions to the nucleon sea. Current phenomenological models that could explain some of these effects are reviewed.

1 Introduction

Elastic scattering of the proton with electrons revealed that, unlike the electron, the proton had a finite size [1]. Further experiments with large momentum transfers showed that, in addition to excitation of the proton into resonance states such as the Δ^+, the proton could break up into a large amount of debris. Beyond the resonance region, it appeared as though the virtual photon probe was no longer interacting with the proton as a whole but with point-like constituents of the proton. Early measurements of the structure functions suggested that they were independent of the momentum transfer, Q [2]. Out of these

[1] This work was supported in part by the Director, Office of Energy Research, Division of Nuclear Physics of the Office of High Energy and Nuclear Physics of the U. S. Department of Energy under Contract Number DE-AC03-76SF00098.

data emerged the parton model of the nucleon [3]. In this picture, the proton has three valence quarks, two up, or u, quarks and one down, or d quark. If these valence quarks, bound in the proton, were its only constituents, there would be nothing further to tell. However, there is much more to the story. When later experiments probed lower values of the fraction of the proton momentum carried by the partons, x, Q^2 scaling was found to be violated [4]. Additionally, if the proton only contained valence quarks at all values of Q, each valence quark should carry a third of the total proton momentum. This also proved to be untrue. The average x of the partons was less than 1/3 and the parton density was correspondingly larger in this $x < 1/3$ region. The low charged x partons contributing to the proton structure functions are quark-anti-quark pairs, known as sea quarks.

The sea quarks are perturbatively generated from gluon splitting, the gluons being the mediators of the strong force. Since the gluons are charge-neutral, they do not directly contribute to the proton structure functions. When no interaction occurs, the sea quarks and gluons serve to dress the bare valence quarks. However, an interaction with a high energy probe such as a virtual photon breaks the coherence of the proton wavefunction and hadronizes the sea quarks and gluons. The higher the energy of the probe, the smaller the value of x that can be studied. Currently the smallest values of x have been reached in ep collisions at HERA [5,6] with a center of mass energy of 310 GeV. These data show a strong increase of the sea quark and gluon densities at low x.

Inherently, the generation of sea quarks at low x and Q is a soft process and cannot be calculated in perturbative Quantum Chromodynamics, QCD. Typically a minimum perturbative momentum transfer is chosen at which the valence quarks, sea quarks, and gluons are assigned distributions for further evolution to higher Q^2. Since these distributions are not calculable, certain assumptions are made regarding the sea quarks. Until recently, it was always assumed that the sea quarks were all symmetric– there was no difference between up, down and strange sea quarks and no difference between *e.g.* the up and anti-up quarks in the sea. In the last few years these assumptions have been seriously challenged. These challenges are the subject of this review.

2 Generation of the perturbative sea

2.1 The improved parton model

The parton model can be applied to the calculation of any cross section with large momentum transfer, referred to as a 'hard interaction'. At high energies, the hadron and parton masses are neglected compared to the hard scattering scale Q. Partons from the initial state hadrons participating in the hard scattering have momentum xp^μ where x is the fraction of the parent momentum carried by the parton, $0 \leq x \leq 1$, and p^μ is the four-momentum of the initial hadron. In the hard scattering, $p^2 = 0$ since the

hadron mass has been neglected. A hard cross section calculated in the parton model from collisions of hadrons A and B to make final states C and D is schematically

$$\sigma_{AB\to CD}(p,p') \sim \int dx_1 dx_2 \frac{dz_1}{z_1}\frac{dz_2}{z_2}\widehat{\sigma}_{ij}(x_1 p, x_2 p')\phi_{i/A}(x_1)\phi_{j/B}(x_2)D_k^C(z_1)D_l^D(z_2)\ . \tag{1}$$

Here $\widehat{\sigma}_{ij}(x_1 p, x_2 p')$ is the lowest order partonic cross section for partons i and j to make the final state kl *i.e.* $gg \to q\overline{q}$ for quark jet production. The probability density for finding parton i in hadron h with momentum fraction x is $\phi_{i/h}(x)$. To produce a final state hadron, C, from parton k or l, the partonic cross section is convoluted with a fragmentation function, $D_k^C(z)$, that describes the hadronization of the parton. The functions $\phi_{i/h}(x)$ which underlie all perturbative QCD calculations are the primary focus of this review.

The most transparent picture of the parton model is deep inelastic scattering of an electron with a hadron. In the hadron, partons exist in a virtual state with definite momenta. When the electron approaches the hadron, due to Lorentz contraction and time dilation, the virtual state is frozen during the time it takes for the electron to cross the hadron. When the lepton transfers the squared four-momentum Q^2 to the hadron via the virtual photon, the distance of closest approach between the lepton and hadron is $\sim 1/Q$. The ratio of the "area" of the momentum exchange to the geometric area of the hadron, $(1/Q^2)/\pi R_0^2$, measures the locality of the lepton probe. When Q^2 is large, this ratio is small, implying that the parton density in the hadron is so dilute that only one parton interacts with the lepton. The hadronization time scale of the partons produced in the hard scattering is taken to be long compared to that of the hard scattering. Therefore, both the initial and final states are decoupled from the hard interaction [7].

Most of the existing information on the nucleon sea has been obtained from deep-inelastic scattering, DIS, and lepton pair production by the Drell-Yan process. The DIS and Drell-Yan kinematics are briefly introduced, following the review of Ref. [7]. While the discussion remains at leading order for clarity, higher order calculations are available, see *e.g.* [8,9]. A typical deep-inelastic scattering reaction is

$$l(p_l) + h(p_h) \to l'(p_{l'}) + X \tag{2}$$

where l is a lepton such as an electron, muon or neutrino, h is typically a proton or a nucleon, and X is the hadronic final state. A virtual vector boson such as a photon or a $W^{\pm}$ is exchanged in the intermediate state. DIS is an inclusive process so that the kinematics can be specified by the measurement of the final lepton four momentum, $p_{l'}^{\mu}$. The momentum transfer is space-like, $q^{\mu} = p_l^{\mu} - p_{l'}^{\mu}$ and $-q^2 = Q^2$. The momentum fraction x, the Bjorken scaling variable, is the ratio of the momentum transfer squared to the energy transferred from the lepton to the hadronic system in the scattering,

$$x = \frac{Q^2}{2p_h \cdot q} = \frac{Q^2}{2m_h \nu}\ . \tag{3}$$

The second equality holds in the target rest frame where $\nu = E_l - E_{l'}$ is the energy transferred from the initial lepton. The ratio of the energy transfer to the total lepton energy in the target rest frame, y, is also useful,

$$y = \frac{p_h \cdot q}{p_h \cdot p_l} = \frac{\nu}{E_l} \ . \tag{4}$$

The mass of the hadronic final state, W, can be large when x is fixed and Q^2 is large since

$$W^2 = m_h^2 + \frac{Q^2}{x}(1-x) \ . \tag{5}$$

Depending on the initial lepton and the squared momentum transfer, the exchanged boson can be a photon, γ, or one of the electroweak vector bosons, W^+, W^-, and Z^0. When a γ or Z^0 is exchanged, there is no charge transferred by the virtual vector boson and the reaction is said to be a neutral current process. The exchange of a W^+ or a W^-, on the other hand, is through a charged current. The following discussion applies to both neutral and charged current processes.

The DIS cross section can be separated into leptonic and hadronic components so that

$$d\sigma = \frac{d^3 p_{l'}}{2s|\vec{p}_{l'}|} \frac{c_V^4}{4\pi^2 (q^2 - m_V^2)^2} L^{\mu\nu}(p_l, q) W_{\mu\nu}(p_h, q) \tag{6}$$

where $V = \gamma$, $W^\pm$, or Z^0 with mass m_V. The vector coupling constants are $c_\gamma = e$, $c_{W^\pm} = g/2\sqrt{2}$, and $c_{Z^0} = g/2\cos\theta_W$ where $g = e/\sin\theta_W$ and θ_W is the Weinberg angle. The boson propagator is assumed to be $\propto (q^2 - m_V^2)^{-1}$.

The lepton tensor is

$$L^{\mu\nu}(p_l, q) = \frac{1}{2}\mathrm{Tr}\left[\not{p}_l \Gamma^\mu_{Vl} (\not{p}_l - \not{q}) \Gamma^\nu_{Vl}\right] \tag{7}$$

where the couplings of the vector bosons to the leptons are $\Gamma^\mu_{\gamma l^\pm} = \gamma^\mu$, $\Gamma^\mu_{W^+\nu} = \gamma^\mu(1-\gamma^5)$, $\Gamma^\mu_{W^-\overline{\nu}} = \gamma^\mu(1+\gamma^5)$, and $\Gamma^\mu_{Z^0} = \gamma^\mu(c_V^f - c_A^f\gamma^5)$ where c_V^f and c_A^f are the vector and axial vector couplings for leptons and quarks of flavor f. Since this review focuses on values of Q^2 where the virtual photon contribution is much larger than that of the Z^0, the Z^0 will no longer be discussed. The lepton spin average factor of $1/2$ in Eq. (7) is absent in neutrino scattering.

The hadron tensor is

$$W_{\mu\nu}(p_h, q) = 2\pi^3 \sum_{\sigma,\, X} \langle h^\sigma(p_h)|j_\mu^{V\dagger}(0)|X\rangle\langle X|j_\nu^V(0)|h^\sigma(p_h)\rangle \delta^4(p_h + q - p_X) \tag{8}$$

where the nucleon spin, σ, is averaged over and the final state, X, has been summed over. Symmetries allow the hadron tensor to be written in terms of structure functions describing lepton scattering with point particles so that

$$\begin{aligned} W_{\mu\nu}(p_h, q) = &- \left(g_{\mu\nu} - \frac{q_\mu q_\nu}{q^2} \right) W_1(x, Q^2) \\ &+ \left(p_{h\,\mu} - q_\mu \frac{p_h \cdot q}{q^2} \right) \left(p_{h\,\nu} - q_\nu \frac{p_h \cdot q}{q^2} \right) \frac{W_2(x, Q^2)}{m_h^2} \\ &- i\epsilon_{\mu\nu\lambda\sigma} \frac{W_3(x, Q^2)}{m_h^2} \end{aligned} \tag{9}$$

where parity conservation in strong interactions implies $W_3 = 0$ for virtual photons. In the Bjorken limit, ν, $Q^2 \to \infty$ for fixed x, the structure functions W_i are functions of x alone to within logarithmic corrections in Q^2,

$$\begin{aligned} F_1^{Vh}(x, Q^2) &= W_1(x, Q^2)\,, \\ F_2^{Vh}(x, Q^2) &= \frac{\nu}{m_h} W_2(x, Q^2)\,, \\ F_3^{Vh}(x, Q^2) &= \frac{\nu}{m_h} W_3(x, Q^2)\ . \end{aligned} \tag{10}$$

The DIS cross section can then be expressed in terms of x, y, and F_i^{Vh} as

$$\begin{aligned} \frac{d\sigma^{lh}}{dxdy} = N^{lV} &\left[\frac{y^2}{2} 2x F_1^{Vh}(x, Q^2) + \left(1 - y - \frac{m_h x y}{2E} \right) F_2^{Vh}(x, Q^2) \right. \\ &\left. + \delta_V \left(y - \frac{y^2}{2} \right) x F_3^{Vh}(x, Q^2) \right]\ , \end{aligned} \tag{11}$$

where E is the lepton energy, m_h is the hadron mass, and $\delta_V = 0$ for γ, -1 for W^-, and $+1$ for W^+. The normalizations are

$$N^{l^\pm \gamma} = 8\pi\alpha^2 \frac{m_h E}{Q^4} \tag{12}$$

$$N^{\nu W^+} = N^{\overline{\nu} W^-} = \frac{\pi \alpha^2 m_h E}{2 \sin^4 \theta_W (Q^2 + M_W^2)^2} = \frac{G_F^2}{\pi} \frac{m_h E M_W^4}{(Q^2 + M_W^2)^2} \tag{13}$$

where α is the electromagnetic coupling constant. The lepton-hadron cross section in Eq. (11) is equivalent to lepton scattering from point-like objects. These objects are the partons.

In the parton model, only charged partonic constituents of the hadron, the quarks and anti-quarks, couple to the electroweak currents at leading order. The DIS cross section is then proportional to the

elastic quark-lepton scattering cross section multiplied by the probability of finding a quark or anti-quark of flavor f and momentum fraction ξ,

$$\frac{d\sigma^{lh}(p_h,q)}{dE_{p_l'}d\Omega_{p_l'}} = \sum_f \int_0^1 d\xi \frac{d\sigma^{lf}(\xi p_h,q)}{dE_{p_l'}d\Omega_{p_l'}}(\phi_{f/h}(\xi)+\phi_{\overline{f}/h}(\xi)) \ . \tag{14}$$

The structure functions can then be directly related to the probability densities by

$$F_{1,3}^{Vh}(x) = \sum_f \int_0^1 \frac{d\xi}{\xi} F_{1,3}^{Vf}\left(\frac{x}{\xi}\right)(\phi_{f/h}(\xi)+\phi_{\overline{f}/h}(\xi)) \tag{15}$$

$$F_2^{Vh}(x) = \sum_f \int_0^1 d\xi F_2^{Vf}\left(\frac{x}{\xi}\right)(\phi_{f/h}(\xi)+\phi_{\overline{f}/h}(\xi)) \ , \tag{16}$$

where F_i^{Vf} are the parton-level structure functions calculated at leading order.

The electromagnetic, neutral current scattering, case where $V=\gamma$ is discussed first. Here, Eq. (2) is $lh \to lX$ where $l = e^{\pm}$ or $\mu^{\pm}$. It can be shown [7] that $2F_1^{\gamma f}(x) = F_2^{\gamma f}(x) = Q_f^2\delta(1-x)$ and that, subsequently, the hadronic structure functions are

$$2xF_1^{\gamma h}(x) = F_2^{\gamma h}(x) = \sum_f Q_f^2 x(\phi_{f/h}(x)+\phi_{\overline{f}/h}(x)) \ . \tag{17}$$

The simplified notation $\phi_{u/p}(x) = u_p(x)$, $\phi_{\overline{u}/p}(x) = \overline{u}_p(x)$, *etc.* is now introduced for the partons in the proton. In this case, Eq. (17) is typically written as

$$2xF_1^{\gamma p}(x) = F_2^{\gamma p}(x) = \sum_f Q_f^2 x(f_p(x)+\overline{f}_p(x)) \tag{18}$$

where $f = u,d,s,c,\cdots$. Note that $f(x)$ is the parton probability density while $xf(x)$ is typically referred to as the parton momentum distribution. The u and d quarks are already present in the proton since, in the constituent quark model, the proton is a uud state where the valence quarks carry the bulk of the quark momentum at large x. The sea quarks do not contribute to the baryon number of the hadron since they are always produced in a virtual quark-anti-quark pair. Therefore, for every $\overline{u}_p$ there is a u_p^s (denoted u_p^s to avoid confusion with the total u_p quark density). The u and d quark densities include both valence and sea quark densities so that

$$u_p(x) = u_p^v(x) + u_p^s(x) \tag{19}$$

$$d_p(x) = d_p^v(x) + d_p^s(x) \ . \tag{20}$$

The number of valence quarks in the proton sums to three,

$$\int_0^1 dx\, u_p^v(x) = 2 \tag{21}$$

$$\int_0^1 dx\, d_p^v(x) = 1 \ , \tag{22}$$

two up valence quarks and one down valence quark.

In addition to the proton parton distributions, DIS on targets such as deuterium or other light nuclei measures the neutron distributions. Typically, one assumes that the per nucleon structure function is *e.g.* for a deuterium target

$$F_2^{\gamma \mathrm{D}}(x) = \frac{1}{2}\left(F_2^{\gamma p}(x) + F_2^{\gamma n}(x)\right) \ , \tag{23}$$

where the neutron parton densities are related to those in the proton by charge symmetry so that

$$\begin{array}{ll} u_p(x) = d_n(x) & d_p(x) = u_n(x) \\ \overline{u}_p(x) = \overline{d}_n(x) & \overline{d}_p(x) = \overline{u}_n(x) \\ s_p(x) = s_n(x) & \overline{s}_p(x) = \overline{s}_n(x) \ \cdots \end{array} \tag{24}$$

Charge symmetry is also used to establish the valence quark sum rules for the neutron, as in Eqs. (21) and (22). The structure functions of other baryons are unmeasured but could be inferred from relationships like those of Eq. (24). Parton distribution functions have also been determined with limited statistics for mesons. In general, the valence quark densities of the meson are assumed to be $\int_0^1 dx q_M^v(x) = 2$ where $\overline{u}$ and d are the valence quarks when $M = \pi^-$. In this case, u_{π^-} is a component of the pion sea.

An exchanged photon treats all charged partons identically. Thus the electromagnetic structure function of the proton, Eq. (18), is the sum over all parton flavors. However, in neutrino-induced interactions, to determine the momentum fraction of the proton carried by the interacting parton, the reactions must proceed by charge current scattering for the final-state electron or muon to be detected. Thus, the DIS reactions are *e.g.* $\nu_e h \to e^- X$ with an exchanged W^+ and $\overline{\nu}_e h \to e^+ X$ with an exchanged W^-. Now not all quarks and anti-quarks couple to the W^+ and W^-. In the reaction $\nu_e h \to e^- X$, the incoming ν_e "decays" to W^+ by $\nu_e \to W^+ e^-$. Then $W^+ d \to u$, $W^+ s \to c$, $W^+ \overline{u} \to \overline{d}$, and $W^+ \overline{c} \to \overline{s}$ so that the W^+ couples to the d, s, $\overline{u}$, and $\overline{c}$ quarks in the proton. Similarly, the W^- emitted in the $\overline{\nu}_e \to W^- e^+$ conversion can couple to the $\overline{d}$, $\overline{s}$, u, and c quarks in the proton. Therefore, for a neutrino beam with exchanged W^+, the structure functions are

$$F_2^{W^+ p}(x) = 2x\left[d_p(x) + s_p(x) + b_p(x) + \overline{u}_p(x) + \overline{c}_p(x)\right] \tag{25}$$

$$F_3^{W^+ p}(x) = 2\left[d_p(x) + s_p(x) + b_p(x) - \overline{u}_p(x) - \overline{c}_p(x)\right] \ . \tag{26}$$

Note that the b quark has been included in the proton sea while the still heavier top quark has not. Likewise, the structure functions determined by an anti-neutrino beam with exchanged W^- are

$$F_2^{W^- p}(x) = 2x\left[\overline{d}_p(x) + \overline{s}_p(x) + \overline{b}_p(x) + u_p(x) + c_p(x)\right] \tag{27}$$

$$F_3^{W^- p}(x) = -2\left[\overline{d}_p(x) + \overline{s}_p(x) + \overline{b}_p(x) - u_p(x) - c_p(x)\right] \quad . \tag{28}$$

Some DIS data, particularly with neutrino beams, have been taken on nuclear targets heavier than deuterium. Therefore it is useful to write the electromagnetic, neutrino and anti-neutrino structure functions in terms of an isoscalar nuclear target. (In an isoscalar target, $Z = N = A/2$, where A is the nuclear mass number, Z is the number of protons and N is the number of neutrons.) Assuming no modifications of the parton densities in the nucleus, the resulting structure functions per nucleon are:

$$\begin{aligned} F_2^{\gamma N_0}(x) = \frac{5}{18}x[&u_p(x) + \overline{u}_p(x) + d_p(x) + \overline{d}_p(x) + \frac{8}{5}(c(x) + \overline{c}(x)) \\ &+ \frac{2}{5}(s_p(x) + \overline{s}_p(x) + b_p(x) + \overline{b}_p(x))]\,, \end{aligned} \tag{29}$$

$$F_2^{W^+ N_0}(x) = x[u_p(x) + \overline{u}_p(x) + d_p(x) + \overline{d}_p(x) + 2s_p(x) + 2b_p(x) + 2\overline{c}_p(x)]\,, \tag{30}$$

$$xF_3^{W^+ N_0}(x) = x[u_p(x) + d_p(x) - \overline{u}_p(x) - \overline{d}_p(x) + 2s_p(x) + 2b_p(x) - 2\overline{c}_p(x)]\,, \tag{31}$$

$$F_2^{W^- N_0}(x) = x[u_p(x) + \overline{u}_p(x) + d_p(x) + \overline{d}_p(x) + 2\overline{s}_p(x) + 2\overline{b}_p(x) + 2c_p(x)]\,, \tag{32}$$

$$xF_3^{W^- N_0}(x) = x[u_p(x) + d_p(x) - \overline{u}_p(x) - \overline{d}_p(x) - 2\overline{s}_p(x) - 2\overline{b}_p(x) + 2c_p(x)]\,. \tag{33}$$

Since measurements of the lepton pairs produced in the Drell-Yan process play an important role in the determination of the nucleon sea, the Drell-Yan process [10] is now introduced. At leading order a quark from the projectile annihilates with its corresponding anti-quark in the target, producing a virtual photon which then decays to a lepton pair with invariant mass M, $q\overline{q} \to \gamma^\star \to l^+l^-$. The Drell-Yan cross section involves a convolution of the parton distributions of both the projectile and the target hadrons. The partonic cross section for Drell-Yan production is

$$\frac{d\hat{\sigma}}{dM} = \frac{8\pi\alpha^2}{9M}Q_f^2\delta(\hat{s} - M^2) \tag{34}$$

where $\hat{s} = x_1x_2s$, x_1 is the fractional momentum carried by the projectile parton, x_2 is the fractional momentum of the target parton, and s is the square of the hadron-hadron center of mass four-momentum. To obtain the hadroproduction cross section as a function of pair mass the partonic cross section is convoluted with the quark and anti-quark densities evaluated at scale M,

$$\frac{d\sigma^{\rm DY}}{dM} = \frac{8\pi\alpha^2}{9M}\int_0^1 dx_1dx_2\,\delta(\hat{s} - M^2)\sum_f Q_f^2[f_p(x_1, M^2)\overline{f}_p(x_2, M^2)$$

$$+ \overline{f}_p(x_1, M^2) f_p(x_2, M^2)] \ . \tag{35}$$

Besides deep-inelastic scattering and Drell-Yan pair production, prompt photon, heavy quark, quarkonium, and jet production are among the processes calculable in perturbative QCD. To obtain the hadronic cross sections, the partonic cross section must convoluted with the projectile and target parton densities. For such a convolution to be reliable, the hadronic cross sections must be factorizable into the process specific short-distance cross section and the parton distributions which cannot be obtained from a first principles calculation and must be assumed to be universal [11], as in Eq. (1). Since the parton distributions are properties of the hadron wavefunction and thus nonperturbative in nature, a universal set of parton densities for a given hadron is typically obtained from fits to DIS and other data. How this is generally done is described in the next sections.

2.2 Q^2 Evolution

Deep inelastic scattering data are available over a wide range of x and Q^2 [4–6]. In the naive parton model, scaling was assumed, *i.e.* the parton distributions were thought to be independent of the Q^2 of the virtual vector boson [2]. However, further measurements [4] soon showed that this was not the case. To obtain a reliable set of parton densities at all x and Q^2, a description of their evolution in x and Q^2 must be available. While this is relatively simple at fixed x when Q^2 is large, the small x behavior of the parton densities is more challenging, as will be discussed later.

Only tree-level (leading order) calculations have been described so far. However, many processes have now been calculated at least to next-to-leading order in QCD. Next-to-leading order calculations involve both real and virtual corrections to the leading order diagrams. At any order in perturbation theory, the hadronic cross section factorizes into a perturbatively calculable partonic cross section and the parton distributions in the hadron, as in Eq. (1). Factorization provides a scheme for separating the short distance partonic cross section from the nonperturbative parton distribution functions, generally referred to as a factorization scheme. The momentum scale at which the separation occurs is the factorization scale.

There are two commonly used factorization schemes, the DIS and the $\overline{\rm MS}$ schemes. In the DIS scheme, F_2^{Vh} is defined so that all corrections are absorbed into the quark and anti-quark distributions order-by-order in perturbation theory. Thus F_2^{Vh} is trivial. However, only F_2^{Vh} enjoys this simplicity while all other structure functions must be corrected order-by-order in α_s. Additionally, the gluon distribution is not fixed in this scheme. The more commonly used $\overline{\rm MS}$ or minimal subtraction scheme defines the parton distributions in terms of parton creation and annihilation operators acting on the hadron wavefunction. The next-to-leading order corrections to the hard scattering are somewhat more complex but the $\overline{\rm MS}$ scheme is more physical and includes the gluon through evolution.

In addition to the factorization scheme and scale dependence, another scale, the renormalization scale, is required to remove the ultraviolet divergences that occur in the calculation of the partonic cross section. In the $\overline{\rm MS}$ scheme, a uniform mass or energy scale is assigned to all diagrams required to calculate the cross section, helping to regulate the divergences. Such a scale assignment automatically introduces a running coupling $\alpha_s(\mu_R^2)$ which allows the cross section to remain independent of the renormalization scale μ_R.

There is no reason why the factorization and renormalization scales should be different and they are indeed usually chosen to be the same. Choosing the two scales to be equal in *e.g.* the $\overline{\rm MS}$ scheme ensures that the parton distributions can be calculated with the local operators and divergences in the cross sections can be handled simultaneously. The cross section, a physical quantity, should not depend on the choice of scheme or scale and would not if it could be calculated to all orders in perturbation theory. However, since the expansion of the cross section in powers of the strong coupling constant is truncated at finite order, a dependence on the scale and scheme remains. The scale at which the hard scattering occurs is then generally the one at which the parton distributions are evaluated.

An important byproduct of factorization is that masuring an observable such as $F_2^{\gamma p}$ at one value of Q^2 such as Q_0^2 enables one to predict the behavior of $F_2^{\gamma p}$ at another value of Q^2 via evolution. In the evolution from Q_0^2 to Q^2, a parton of momentum fraction x, probed by a virtual photon with momentum transfer Q_0^2, can split into two partons with lower momentum fractions, y and z, with $y+z=x$. For a virtual photon to resolve a charged parton of momentum y, $y<x$, it must have a larger momentum transfer than Q_0^2, $Q^2 > Q_0^2$. When x and Q^2 are not too small, the Dokshitzer-Gribov-Lipatov-Altarelli-Parisi (DGLAP) equations [12] describe how the parton distributions are determined at $Q^2 > Q_0^2$ starting from an initial distribution at a low scale Q_0^2. Evolution in Q^2 links the charged quark and anti-quark distributions with the neutral partons, or gluons, since quarks emit gluons while gluons can split into $q\overline{q}$ pairs or into two gluons. The gluon is thus defined through its evolution in the $\overline{\rm MS}$ scheme. At leading order, the DGLAP equations are

$$\frac{dq_i(x,Q^2)}{d\log Q^2} = \frac{\alpha_s(Q^2)}{2\pi}\int_x^1 \frac{dy}{y}\left[q_i(y,Q^2)P_{qq}\left(\frac{x}{y}\right) + g(y,Q^2)P_{qg}\left(\frac{x}{y}\right)\right] \tag{36}$$

$$\frac{dg(x,Q^2)}{d\log Q^2} = \frac{\alpha_s(Q^2)}{2\pi}\int_x^1 \frac{dy}{y}\left[\sum_i q_i(y,Q^2)P_{gq}\left(\frac{x}{y}\right) + g(y,Q^2)P_{gg}\left(\frac{x}{y}\right)\right] \quad , \tag{37}$$

where the sum $i = 1 \ldots 2n_f$ runs over quarks and anti-quarks of all flavors. The probability that parton i has emitted parton j is proportional to the splitting functions P_{ij}. The strong coupling constant, α_s, appears because of the quark-gluon and gluon-gluon vertices. The parton distributions in Eqs. (14) - (28) all have had the Q^2 dependence suppressed. The suppression of the Q^2 argument of the parton distribution functions is common throughout this review.

While the evolution of the parton distributions can be described by perturbative QCD, some initial set

of parton distributions must be defined at scale Q_0^2. This initial scale is somewhat arbitrary but can be thought of as the boundary between perturbative and nonperturbative physics. The initial scale is usually in the range $0.5 < Q_0^2 < 5$ GeV^2.

2.3 Experimental studies

Although a great deal of precise information is generally obtainable from DIS, particularly since the parton densities of only one hadron are involved, DIS does not distinguish between quark flavors. Other processes are also needed to identify the effects of individual parton flavors. A large collection of data are used to fit the parton distributions at the initial scale Q_0. The DGLAP equations then evolve the parton densities to higher scales. A list of some relevant measurements and which parton distributions they illuminate is given below:

- $F_2^{\gamma p}(x,Q^2)$ from $e^{\pm}p$ interactions at the HERA collider [5,6], charged partons at small x;
- $F_2^{\gamma p}(x,Q^2)$ and $F_2^{\gamma \mathrm{D}}(x,Q^2)$ from μ beams by NMC [13] and BCDMS [14], charged partons;
- $F_2^{W^{\pm}N}(x,Q^2)$ and $xF_3^{W^{\pm}N}(x,Q^2)$ from ν beams on nuclear targets [15–17], charged partons;
- prompt photons, $qg \to \gamma q$, gluon distribution;
- Drell-Yan production, $q\overline{q} \to \gamma* \to l^+l^-$, sea quark distributions;
- $W^{\pm}$ and Z^0 production in $p\overline{p}$ colliders, u and d distributions — *e.g.* $\sigma_{W^{\pm}}/\sigma_{Z^0} \propto d/u$;
- Z^0 pole measurements in e^+e^- collisions [18], intrinsic scale, Λ_{QCD}, of α_s.

Note that combinations of F_2^{Vh} and F_3^{Vh} can pick out certain parton densities. For example, using Eqs. (25)-(28), $xF_3^{W^+p} + xF_3^{W^-p} + F_2^{W^+p} - F_2^{W^-p} = xd_p^v(x,Q^2)$. In fact, if both p and n targets are used with the assumption of charge symmetry and an SU(3) flavor symmetric sea, $\overline{u}_p = \overline{d}_p = \overline{s}_p$ with $\overline{c}_p = \overline{b}_p = 0$, the parton distributions are overdetermined and consistency checks can be made. It turns out, as discussed in this review, that there is no sea quark SU(3) flavor symmetry.

Some characteristic data on $F_2^{\gamma p}$ from muon beams at 120, 200, 240, and 280 GeV on hydrogen targets at CERN and the neutrino structure functions $F_2^{W^{\pm}N}$ and $xF_3^{W^{\pm}N}$ from ν and $\overline{\nu}$ beams on an iron target at Fermilab are shown in Figs. 1 and 2 respectively. Several values of x are selected and the Q^2 dependence of each x bin is shown. Note that in the intermediate x range, $0.125 < x < 0.35$, little Q^2 dependence is observed, prompting the scaling assumption from the early data taken in this x region [2]. More recently, the HERA ep collider at $\sqrt{s} = 310$ GeV has provided data over a wider range of x and Q^2 than previously available. A sample of the HERA data is shown in Fig. 3. The scaling violations only somewhat apparent in the fixed target experiments are more obvious at HERA.

Since pure neutrino beams are unavailable, neutrino experiments with secondary beams collect data from both neutrino and anti-neutrino-induced events from all possible neutrino energies. The resulting measured structure functions are a weighted average of the ν and $\overline{\nu}$ induced events, *e.g.* $F_2^{W^+N_0}$ and

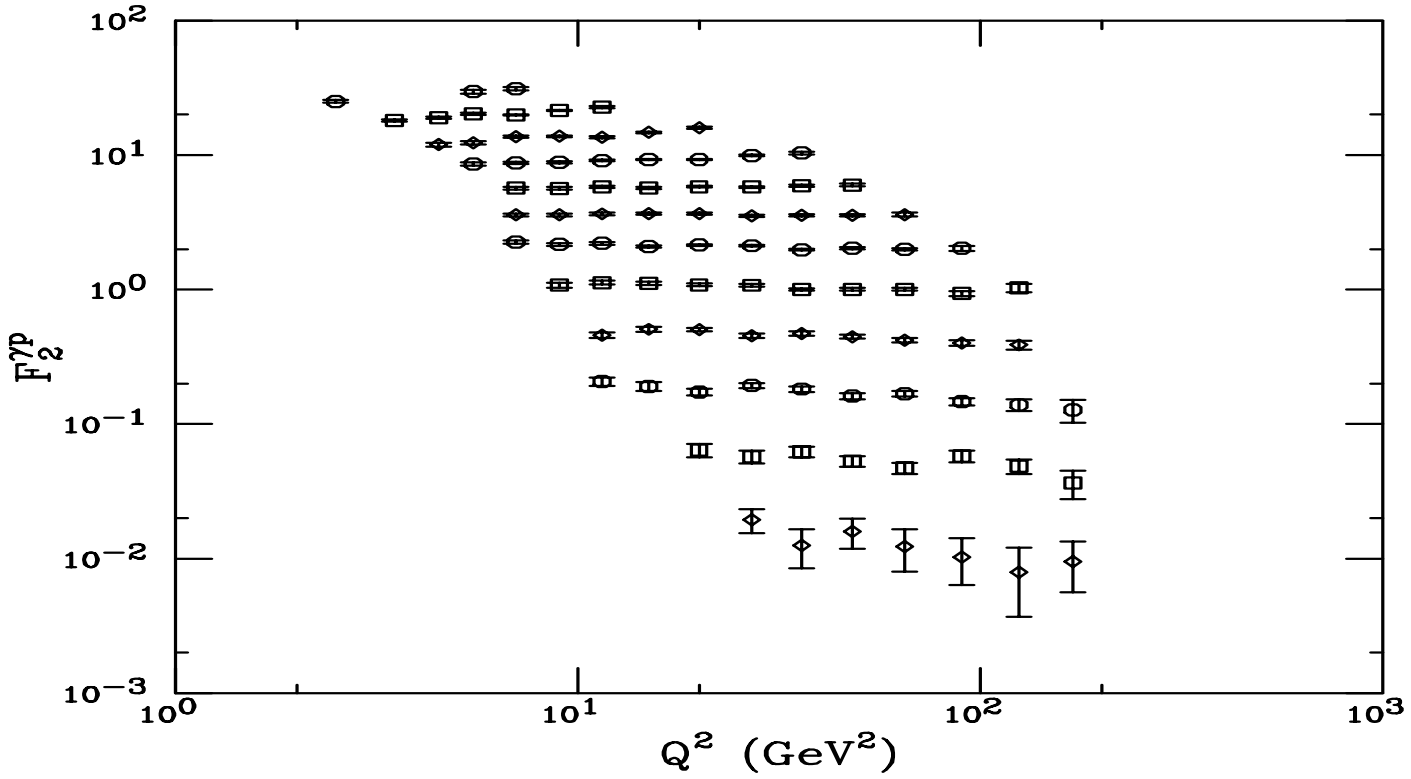

Fig. 1. The proton structure function $F_2^{\gamma p}$ as a function of Q^2 for muon beams with energies 120, 200, 240, and 280 GeV measured by the European Muon Collaboration [19]. From top to bottom the values of the x bins are: 0.0175, 0.03, 0.05, 0.08, 0.125, 0.175, 0.25, 0.35, 0.45, 0.55, 0.65, and 0.75. To separate the data, $F_2^{\gamma p}$ in each x bin is scaled by a factor of 1.5 from the next higher x bin. Therefore, only the highest x data (lowest points) have the correct scale. Only the statistical uncertainty is shown.

$F_2^{W^- N_0}$. If $\beta \equiv N_\nu/(N_\nu + N_{\overline{\nu}})$ is the fraction of DIS events induced by neutrinos, the experimentally determined structure function is

$$\begin{aligned} F_2^{W^\pm N_0}(x) &= \beta F_2^{W^+ N_0}(x) + (1-\beta) F_2^{W^- N_0}(x) \\ &= \frac{1}{2}[F_2^{W^+ N_0}(x) + F_2^{W^- N_0}(x)] \\ &\quad + \frac{1}{2}(2\beta - 1)[F_2^{W^+ N_0}(x) - F_2^{W^- N_0}(x)] \ . \end{aligned} \tag{38}$$

If $\beta = 1/2$ or $F_2^{W^+ N_0} = F_2^{W^- N_0}$, implying $s_p(x) = \overline{s}_p(x)$, the second term in Eq. (38) vanishes. From the CCFR data [20], $\beta = 0.83$ [21] so that $F_2^{W^\pm N_0}$ is dominated by $F_2^{W^+ N_0}$ or neutrino-induced production. In an analysis of opposite sign dilepton production, they found that to next-to-leading order, $s_p(x) = \overline{s}_p(x)$ within their experimental errors [22]. (These results will be discussed in more detail in Sec. 3.2.1.) However, since $\beta > 1/2$, the associated uncertainties are significant. By comparing the neutrino and

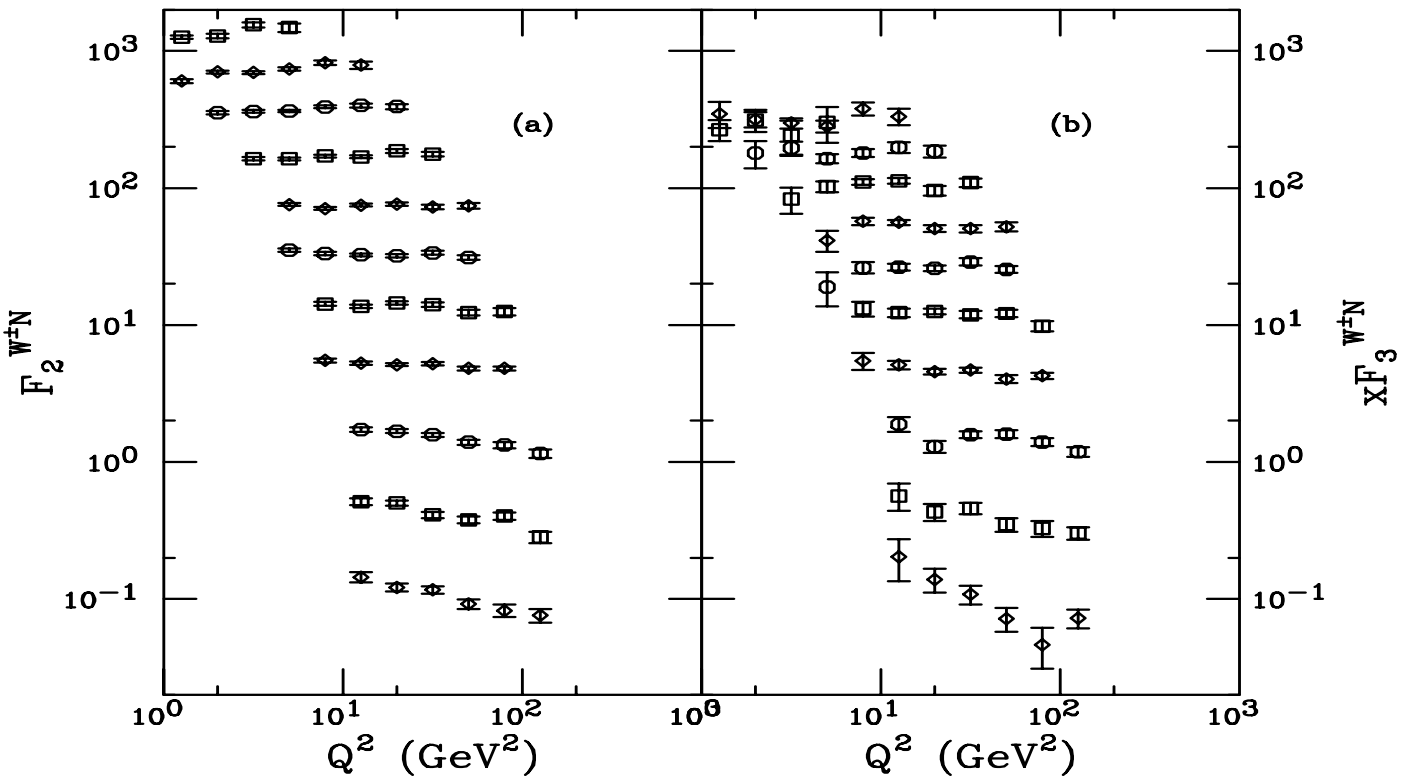

Fig. 2. The nucleon structure functions $F_2^{W^\pm N}$ (a) and $xF_3^{W^\pm N}$ (b) as a function of Q^2 [15] from neutrino-iron deep-inelastic scattering. The x bins from top to bottom are: 0.015, 0.045, 0.08, 0.125, 0.175, 0.225, 0.275, 0.35, 0.45, 0.55, and 0.65. To separate the data, the structure functions in each x bin are scaled by a factor of 2 from the next higher x bin. Therefore, only the highest x data (lowest points) have the correct scale. Only the statistical uncertainty is shown.

electromagnetic structure functions, one can form the relation,

$$\frac{5}{6}F_2^{W^\pm N_0}(x) - 3F_2^{\gamma N_0}(x) = \frac{1}{2}x[s_p(x) + \overline{s}_p(x)] + \frac{5x}{6}(2\beta - 1)[s_p(x) - \overline{s}_p(x)] \ . \tag{39}$$

If $s_p(x) = \overline{s}_p(x)$, then Eq. (39) could be used to determine the strange quark distribution. However, the strange quark distribution extracted in this fashion does not agree with independent experimental results [21].

To obtain the parton densities, a global analysis of all available data is performed. This analysis involves taking data from many different processes measured over a range of x and Q^2 and making a multi-parameter fit to all the data, as described below. First, it is necessary to solve the coupled integro-differential evolution equations, Eqs. (36) and (37) and at leading order or their next-to-leading order,

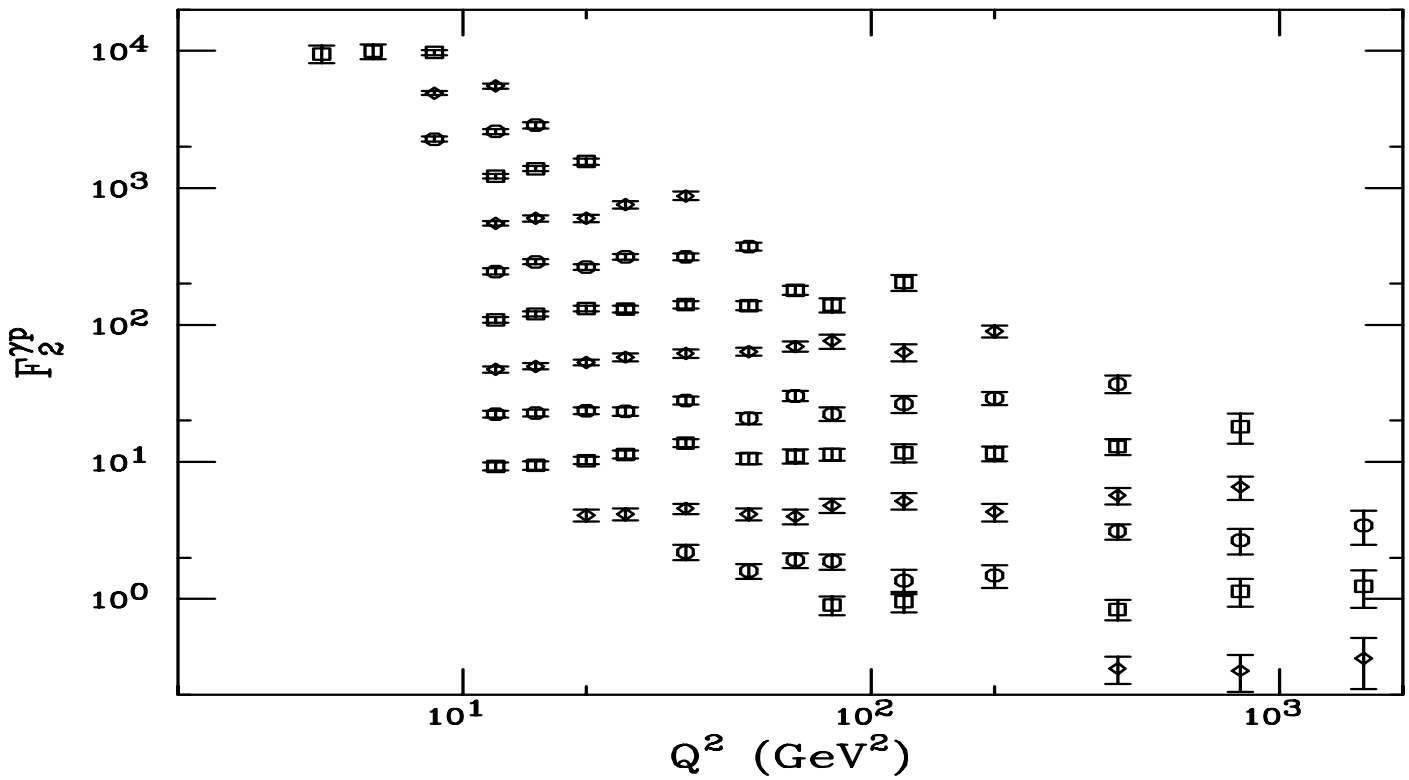

Fig. 3. The proton structure function $F_2^{\gamma p}$ as a function of Q^2 at the HERA collider (26.7 GeV electrons on 820 GeV protons) [6]. From top to bottom the values of the x bins are: 0.000178, 0.000261, 0.000383, 0.000562, 0.00075, 0.000825, 0.00133, 0.00237, 0.00421, 0.0075, 0.0133, 0.0237, 0.0421, 0.075, and 0.133. To separate the data, the structure function in each x bin is scaled by a factor of 2 from the next higher x bin. Therefore, only the highest x data (lowest points) have the correct scale. Only the statistical uncertainty is shown.

NLO, counterparts, numerically to be able to calculate the parton densities at the Q^2 appropriate to the measurement. The data to be used in the fit are then chosen. Typically only data sets that can provide the best constraints on the parton densities are included except when the data indicate significant new physics at work. Since the evaluation is done at fixed order in perturbation theory, a factorization scheme is chosen and all the evaluations of the parton densities are done for the same order of perturbation theory. It is very important that this be done consistently when calculating all processes considered. A starting distribution at scale Q_0^2, typically of the form

$$xf(x,Q_0^2) = A_0 x^{A_1}(1-x)^{A_2} P(x) \tag{40}$$

is assumed where $P(x)$ is a smooth polynomial function, the exponent A_1 determines the small x behavior, and A_2 governs the large x behavior. These initial distributions are then evolved to the appropriate scale of the data and used to calculate the cross section or structure function at the same x and Q^2 as the data. The goodness of the fit, its χ^2, is calculated from a comparison to all the data in the

fit and the parameters in *e.g.* Eq. (40) adjusted in each iteration to minimize the χ^2. The final fits are generally made available either in tables with some interpolation formula used to obtain the densities at any x and Q^2 or as parameterized functions of x and Q^2. Parton distribution functions determined in this manner are only as good as the data they fit and may fail to match new data outside the x and Q^2 range of the old measurements. As new data are taken, the parton distribution functions are thus continually updated.

An example of updating the parton distribution functions as new data appear is the changing starting assumption regarding the degree of flavor symmetry in the sea. In early global analyses, an SU(3) flavor symmetric sea was assumed, see *e.g.* Ref. [23]. However, it was shown that the strange sea is smaller than the light quark sea so that $2\overline{s}_p/(\overline{u}_p + \overline{d}_p) \sim 0.5$ [17,24]. Thus, the sea could at most be SU(2) flavor symmetric. It has been further shown that the SU(2) flavor symmetry may not hold, as discussed in the next section. Newer fits of the parton distribution functions such as those in Refs. [25–27] include these results in the sea quark analysis.

Several different groups have been involved in the global analysis of the parton distributions. The CTEQ (Coordinated Theoretical-Experimental Project on QCD) collaboration [25] and Martin, Roberts, and Sterling (MRS) and their collaborators [26] have produced a variety of parton distribution functions which improve with each round of data. Glück, Reya, and Vogt (GRV) [27] have taken a rather different route, beginning at a low initial scale with valence-like sea quark and gluon distributions without trying to make a comprehensive fit. A library of all available parton distribution functions can be found in the program package PDFLIB available from the CERN program libraries [28]. Care must be taken however to use only the most recent sets, matching the appropriate order of the parton densities and hard scattering cross section in scale and scheme.

In Figs. 4, 5 and 6, the parton distributions obtained in recent global fits to NLO by CTEQ [25], MRST [26], and GRV [27] are shown as a function of x for two different values of Q^2. In each case, the sea quark and gluon evolution is stronger than the valence evolution. The evolution is faster at low x than at intermediate and large x. While the $\overline{u}_p$ and $\overline{d}_p$ distributions are different for $x > 0.01$, as discussed shortly, they are nearly equal at low x. The strange quark distributions are generally smaller than the light quark distributions but by $x \sim 10^{-4}$, $\overline{s}_p \approx \overline{u}_p$. The gluon distribution, least constrained by data, evolves more rapidly in Q^2 than do the charged parton distributions.

2.4 Aspects of the small x sea

As already discussed, the parton distributions are determined in practice from fits to DIS and related data by parameterizing the distributions at a Q_0 large enough for perturbative QCD to be applicable. Then the distributions are evolved to higher Q^2 using the DGLAP equations, Eqs. (36)-(37). Evolution to higher Q^2 when x is not too small should give reliable results. However, extrapolation to small x

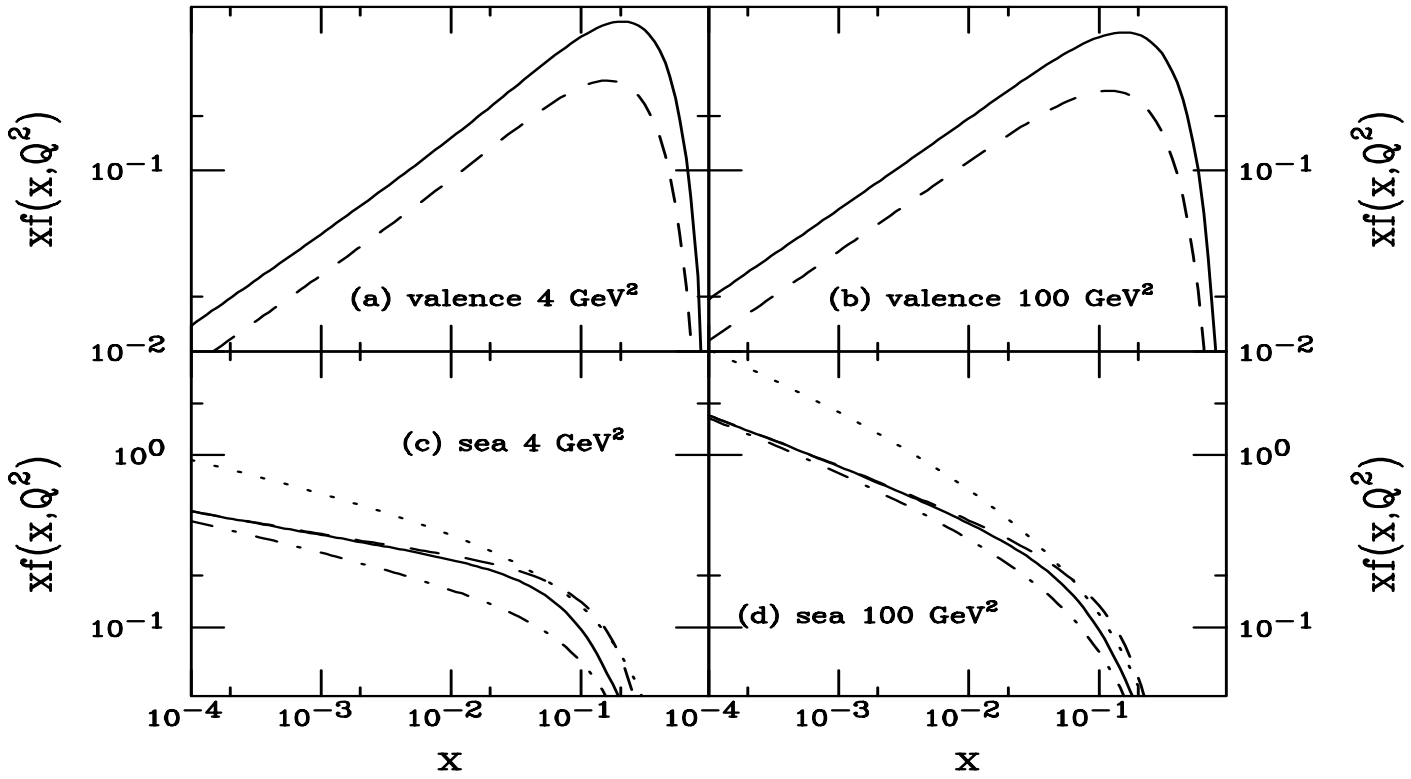

Fig. 4. The CTEQ5 NLO $\overline{\rm MS}$ scheme proton parton distributions are given at $Q^2 = 4$ and 100 GeV^2. The up and down valence distributions are shown in the solid and dashed lines respectively in (a) and (b). The up, down and strange sea distributions and the gluon distributions are given in the solid, dashed, dot-dashed and dotted curves respectively in (c) and (d).

is more difficult. Early expectations based on Regge theory suggested that the sea quark and gluon distributions should become constant as $x \to 0$. The HERA data have clearly shown that this is not true, as seen in Fig. 3. In this section, the way this behavior can arise is explained.

Gluon ladder diagrams such as the one in Fig. 7, taken from Ref. [29], represent the behavior of DIS scattering. In the regime of finite x and large Q^2, the DGLAP equations hold and the dominant contribution to the evolution of the sea and gluon distributions come from the region of strongly ordered transverse momentum, $Q^2 \gg k_T^2 \gg k_{nT}^2 \gg \cdots \gg k_{1T}^2 \gg Q_0^2$.

When x is small and Q^2 remains large, strong ordering in the longitudinal momentum, $x \ll \xi_n \ll \cdots \ll \xi_1$, is as important as the transverse momentum ordering. The probability of emitting the $i^{\rm th}$ gluon on the ladder is proportional to $\alpha_s[dx_i/x_i][dk_{iT}^2/k_{iT}]^2$. The nested integrations over x and k_T generate the leading order behavior of the sea quark and gluon distribution, assuming α_s is constant,

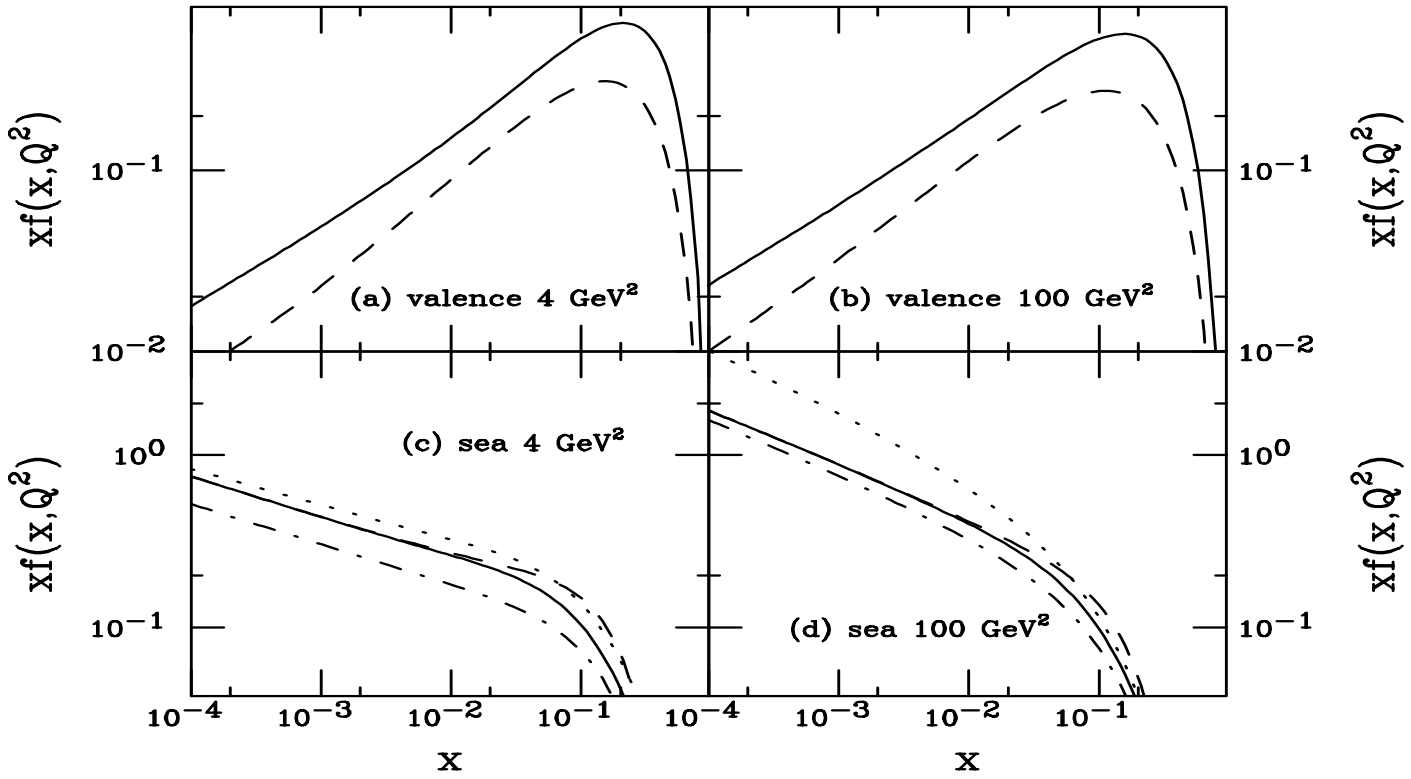

Fig. 5. The MRST NLO $\overline{\rm MS}$ scheme proton parton distributions are given at $Q^2 = 4$ and 100 GeV^2. The up and down valence distributions are shown in the solid and dashed lines respectively in (a) and (b). The up, down and strange sea distributions and the gluon distributions are given in the solid, dashed, dot-dashed and dotted curves respectively in (c) and (d).

$$xf(x,Q^2) \simeq \exp\left[2\left[\frac{3\alpha_s}{\pi}\ln\left(\frac{1}{x}\right)\ln Q^2\right]^{1/2}\right] \ , \tag{41}$$

known as the double leading logarithm approximation, DLLA. The name DLLA implies that only the terms proportional to $\ln(1/x)\ln Q^2$ multiplying each power of α_s are kept in the expansion of Eq. (41). In this case, $xf(x,Q^2)$ increases as $x \to 0$. The increase is faster than any power of $\ln(1/x)$ but slower than any power of x.

In the case of small x and finite Q^2, only the longitudinal momentum is now strongly ordered and the full k_T phase space must be integrated over rather than retaining only the leading terms in $\ln Q^2$. A counterpoint to the DGLAP equations at small x is the Lipatov or BFKL [30] equation that evolves a starting distribution $f(x_0,k_T^2)$ at x_0 downwards in x by integrating over the k_T phase space,

$$x\frac{\partial f(x,k_T^2)}{\partial x} = \int dk_T'^2 K(k_T,k_T')f(x,k_T'^2) \ . \tag{42}$$

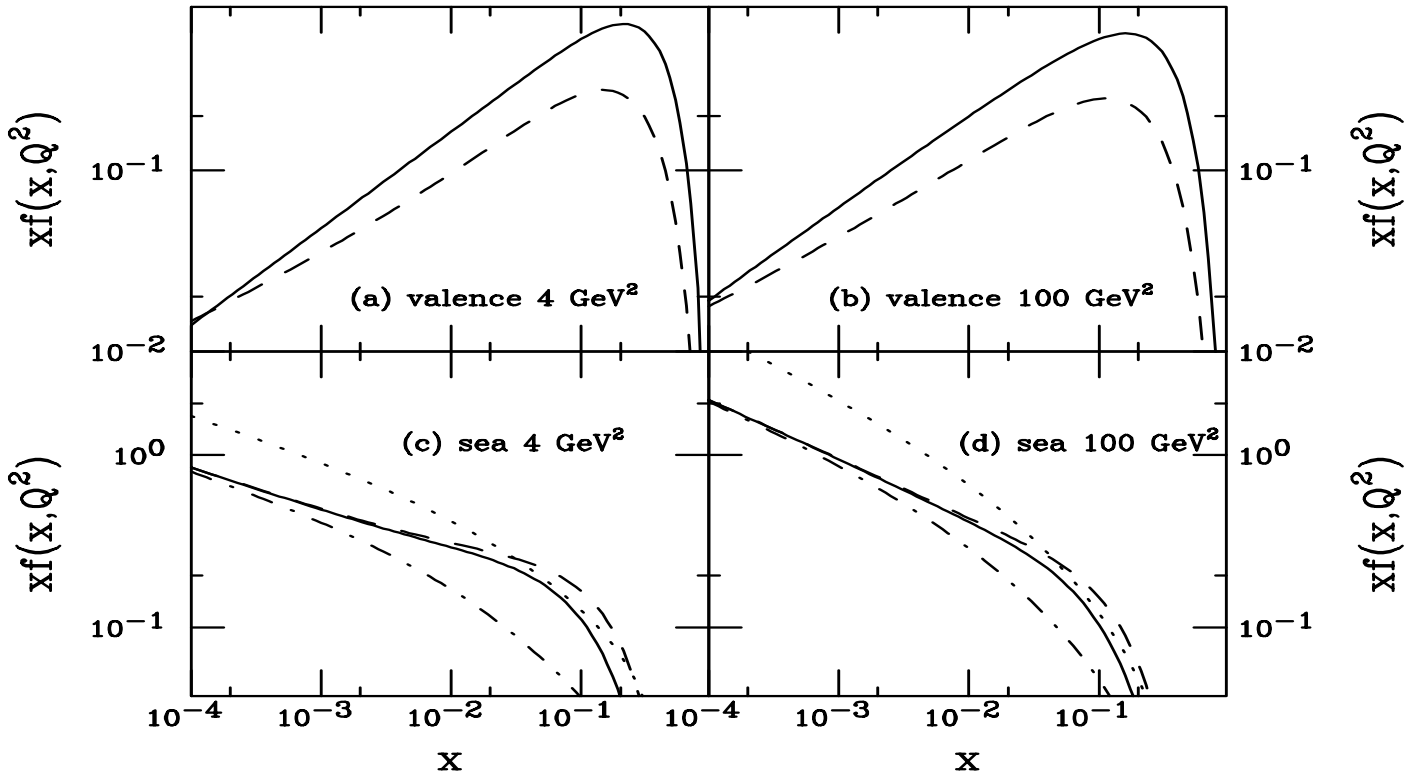

Fig. 6. The GRV 94 HO NLO $\overline{\rm MS}$ scheme proton parton distributions are given at $Q^2 = 4$ and 100 GeV^2. The up and down valence distributions are shown in the solid and dashed lines respectively in (a) and (b). The up, down and strange sea distributions and the gluon distributions are given in the solid, dashed, dot-dashed and dotted curves respectively in (c) and (d).

The kernel K includes real and virtual gluon emission. The Lipatov equation is related to the sea quark or gluon distribution before the integration over transverse momentum has been performed, $f(x,k_T^2) = \partial(xg(x,Q^2))/\partial \ln Q^2|_{Q^2=k_T^2}$. The hadronic cross section is typically the partonic cross section convoluted with an x-dependent parton distribution, as in Eq. (1). However, in this case, the partonic cross section is convoluted with a k_T-dependent parton density so that $\sigma \sim \int dx\,[dk_T^2/k_T^2] f(x,k_T^2)\hat{\sigma}$. If α_s is fixed, an approximate analytical solution may be found for $x \to 0$,

$$xf(x,Q^2) \sim h(Q^2) x^{-\lambda} \; ; \quad \lambda = \frac{12\alpha_s}{\pi} \ln 2 \; . \tag{43}$$

The predicted value of λ is ~ 0.5 when α_s is fixed. Allowing α_s to run with Q^2 introduces a dependence on the cutoff of the k_T^2 integration.

The increase in the sea quark and gluon distributions at small x in Eq. (43) cannot continue indefinitely because the hadron will become so dense that the partons can no longer be considered to be free. The growth must eventually be suppressed, most likely by gluon recombination [31]. It is unknown at what

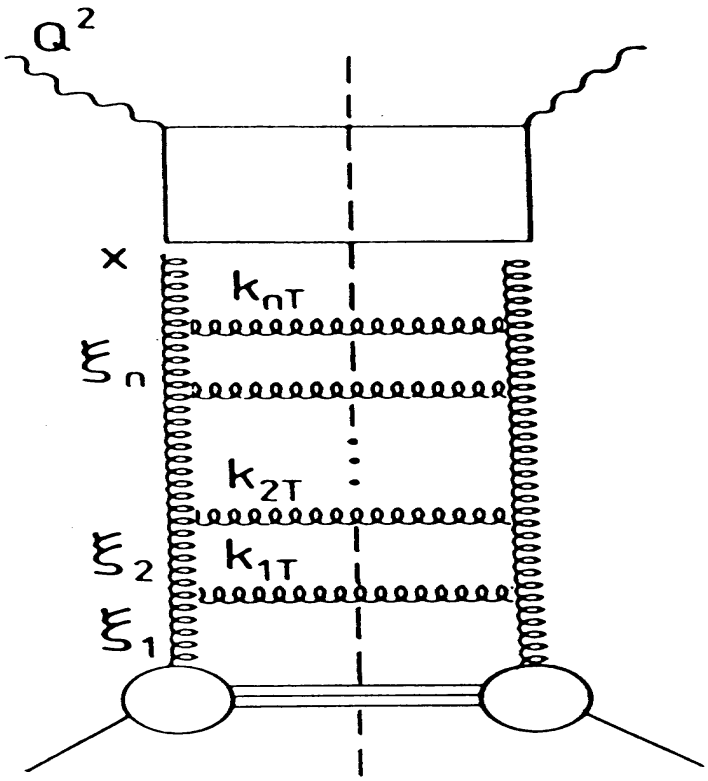

Fig. 7. Ladder diagram corresponding to evolution of parton distribution functions. At large Q^2, DGLAP evolution sums diagrams with strong ordering in k_T, $Q^2 \gg k_T^2 \gg k_{nT}^2 \gg \cdots \gg k_{1T}^2 \gg Q_0^2$. At small x, the leading contribution comes from ordering in ξ, $x \ll \xi_n \ll \cdots \ll \xi_1$ but with the gluon k_T unordered. Reproduced from Ref. [29] with permission of the publisher.

value of x this "shadowing" becomes important. For example, an anti-quark with distribution $\overline{q}(x, Q^2)$ has an apparent transverse size of $1/Q$ but a smaller longitudinal size $1/xp$ with proton momentum p in a frame where $xp \gg Q$. The scattering cross section of the sea quarks and gluons is proportional to the square of the transverse size, $\hat{\sigma} \sim \alpha_s(Q^2)/Q^2$. When the area covered by the total number of sea quarks and gluons, n, scattering with the cross section $\hat{\sigma}$, approaches the transverse area of the proton, πr_p^2, or $n\hat{\sigma} \sim \pi r_p^2$, shadowing is no longer negligible and introduces an additional term in the evolution equations [32,33].

In practice, the parton distributions are only fit with DGLAP evolution with A_1 chosen in accord with the BFKL behavior. The starting sea quark and gluon distributions in Eq. (40) have been found to have $A_1 \sim -0.3$. While this is a faster growth than Regge theory suggested, it is lower than the idealized BFKL result of $A_1 \sim -0.5$. It is difficult to see from these results whether or not shadowing is important because a full next-to-leading order evolution scheme incorporating DGLAP, DLLA, and BFKL is not available over the entire x and Q^2 range.

2.5 Perturbative sea summary

The naive parton model and its extensions have been extremely successful in describing a large number of processes. Both the data and the NLO perturbative calculations used to model the data are now extremely precise over a wide range of x, from 2×10^{-4} to 0.75. The parton distribution functions extracted from global analyses by a number of groups agree well with the data and with each other over their range of validity and will continue to be refined as new data are taken.

3 Possible nonperturbative contributions to the sea

So far, only the generation of the perturbative sea has been discussed. However, since the parton distributions are fit rather than derived from first principles and the perturbative evolution cannot go backwards and remain stable, the true nature of the nucleon sea is, at its heart, unknown. While the valence and sea quark distributions have been measured as a whole in DIS, and the valence and sea quark distributions can be separated from one another, the individual sea quark distributions are more difficult to tease out from bulk measurements. Therefore, simplifying assumptions have been made about the proton sea. Recently, experiments have been challenging the standard assumptions of the parton model such as SU(2) flavor and charge symmetry. The rest of this review is devoted to some of these results and their interpretations.

3.1 The Gottfried sum rule–$\overline{u}$ vs. $\overline{d}$

Assuming flavor symmetry, proton and neutron parton distributions can be related. Valence quark counting suggests that the neutron d distribution and the proton u distribution should be equal, $d_n = u_p$ at all x and Q^2. Similar assumptions can be made for the other parton distributions, see Eq. (24). Therefore, unless flavor symmetry breaking is discussed, u, d, $\cdots$ can be assumed to refer to the proton parton distributions. The difference between the proton and neutron structure functions can then be written as

$$\frac{1}{x}\left(F_2^{\gamma p}(x) - F_2^{\gamma n}(x)\right) = \frac{1}{3}\left[u^v(x) - d^v(x)\right] + \frac{2}{3}\left[\overline{u}(x) - \overline{d}(x)\right] \ . \tag{44}$$

Using Eqs. (21) and (22) for the proton valence quark distributions, after integrating both sides of Eq. (44) over x, one obtains

$$\int_0^1 \frac{dx}{x}\,[F_2^{\gamma p}(x) - F_2^{\gamma n}(x)] = \frac{1}{3} + \frac{2}{3}\int_0^1 dx\,[\overline{u}(x) - \overline{d}(x)] \quad . \tag{45}$$

If the sea is flavor symmetric, $\overline{u} = \overline{d}$ and the second term vanishes. This is the Gottfried sum rule [34]:

$$\int_0^1 \frac{dx}{x}\,[F_2^{\gamma p}(x) - F_2^{\gamma n}(x)] = \frac{1}{3} \quad . \tag{46}$$

The assumption of light anti-quark flavor symmetry is a serious one and if the sum rule is found to be violated, the nucleon sea could be SU(2) flavor asymmetric.

3.1.1 Current experimental studies

Because the integral of Eq. (46) is over all x, the small x region could have a significant contribution to the sum rule. Therefore the determination of any possible violation is only partial and depends strongly on the extrapolation of the parton distributions to low x. This was especially true when the proton parton distribution functions were not well constrained at low x by other measurements. The minimum x is restricted by the lepton-beam energy, E, to be $x_{\rm min} = Q^2/2ME$, where Q^2 should not be smaller than a few GeV^2 in order for the parton model to be applicable. To quantify the discussion, the Gottfried integral can be defined as

$$I_G(x_{\rm min}, x_{\rm max}) \equiv \int_{x_{\rm min}}^{x_{\rm max}} \frac{dx}{x}\,[\,F_2^{\gamma p}(x) - F_2^{\gamma n}(x)\,] \ . \tag{47}$$

Generally two values of I_G are given for each measurement, one with $x_{\rm min}$ and $x_{\rm max}$ limited by the experiment, the other extrapolated over the entire x range. The integral over all x depends on how the missing small x region is accounted for. The results are summarized in Table 1. When the Gottfried integral is given more than once for the same collaboration, the second result is obtained from a reanalysis of the earlier data.

Typical DIS targets used to measure the structure functions are hydrogen and deuterium. The neutron distribution is then generally extracted taking into account the momentum smearing effects due to Fermi motion in the deuteron. However, the NMC analysis obtained the difference from the relation

$$F_2^{\gamma p} - F_2^{\gamma n} = 2\,F_2^{\gamma {\rm D}}\,\frac{1 - F_2^{\gamma n}/F_2^{\gamma p}}{1 + F_2^{\gamma n}/F_2^{\gamma p}} \quad , \tag{48}$$

Measurement	$x_{\min}$	$x_{\max}$	$I_G(x_{\min}, x_{\max})$	$I_G(0,1)$
SLAC [35]	0.02	0.82	0.20 ± 0.04	–
EMC [36]	0.03	0.65	$0.18 \pm 0.01 \pm 0.07$	$0.24 \pm 0.02 \pm 0.13$
EMC [37]	0.02	0.80	$0.197 \pm 0.011 \pm 0.083$	$0.235\,^{+0.110}_{-0.099}$
BCDMS [14]	0.06	0.80	$0.197 \pm 0.006 \pm 0.036$	–
NMC [38]	0.004	0.80	$0.227 \pm 0.007 \pm 0.014$	0.240 ± 0.016
NMC [39]	0.004	0.80	$0.221 \pm 0.008 \pm 0.019$	0.235 ± 0.026

Table 1
Deep inelastic scattering measurements of the Gottfried sum rule. The Gottfried integral, Eq. (47), is given for each measurement and for the full x range when available.

where the ratio $F_2^{\gamma n}/F_2^{\gamma p} = 2F_2^{\gamma \mathrm{D}}/F_2^{\gamma p} - 1$ is determined from the NMC data [38,39]. The absolute value of $F_2^{\gamma \mathrm{D}}$ is fit from data. Nuclear corrections such as Fermi motion were not taken into account. The difference measured by NMC is shown in Fig. 8.

The data in Table 1 indicate $I_G(0,1) < 1/3$, a clear violation of the Gottfried sum rule. When the first data appeared, the low x parton distribution functions were not known from other sources. Therefore attempts were made to satisfy SU(2) flavor symmetry by changing the shape of the valence u and d distributions in the unmeasured region, see *e.g.* Ref. [43]. However, the lower x NMC data [38,39] showed that this idea was untenable. Other attempts to understand the sum rule violation centered around the extraction of the neutron distribution from deuterium or other light nuclear data. The nuclear parton distribution functions are different from free proton distributions [44]. At small x, there is a depletion of $F_2^{\gamma A}$ in nuclear targets, known as shadowing, which was typically neglected in deuterium. The effect has been studied in a variety of models including vector meson dominance, Pomeron and meson exchange models and has been found to contribute only $\delta I_G(0,1) = -0.02$ [45,46] to the Gottfried sum rule. Note that since the shadowing contribution, $\delta I_G(0,1)$ above, is negative, correcting for the effect in deuterium increases the Gottfried sum rule violation. Therefore, an SU(2) flavor asymmetry in the nucleon sea is the most likely explanation of the observed effect with $\overline{d} > \overline{u}$.

Unfortunately DIS data can only address the difference between the light anti-quark distributions, usually written as $\overline{d} - \overline{u}$ for a positive quantity. The individual anti-quark distributions cannot be studied separately. An independent measurement of $\overline{d}/\overline{u}$ is needed. The Drell-Yan process provides an elegant way to obtain the ratio $\overline{d}/\overline{u}$ by comparing Drell-Yan production on proton and deuterium targets [47]. Then

$$\begin{aligned} \sigma_{p\mathrm{D}}^{\mathrm{DY}} &= \sigma_{pp}^{\mathrm{DY}} + \sigma_{pn}^{\mathrm{DY}} \\ &\propto \frac{1}{9}\left[(4u(x_1) + d(x_1))(\overline{u}(x_2) + \overline{d}(x_2))\right. \end{aligned} \tag{49}$$

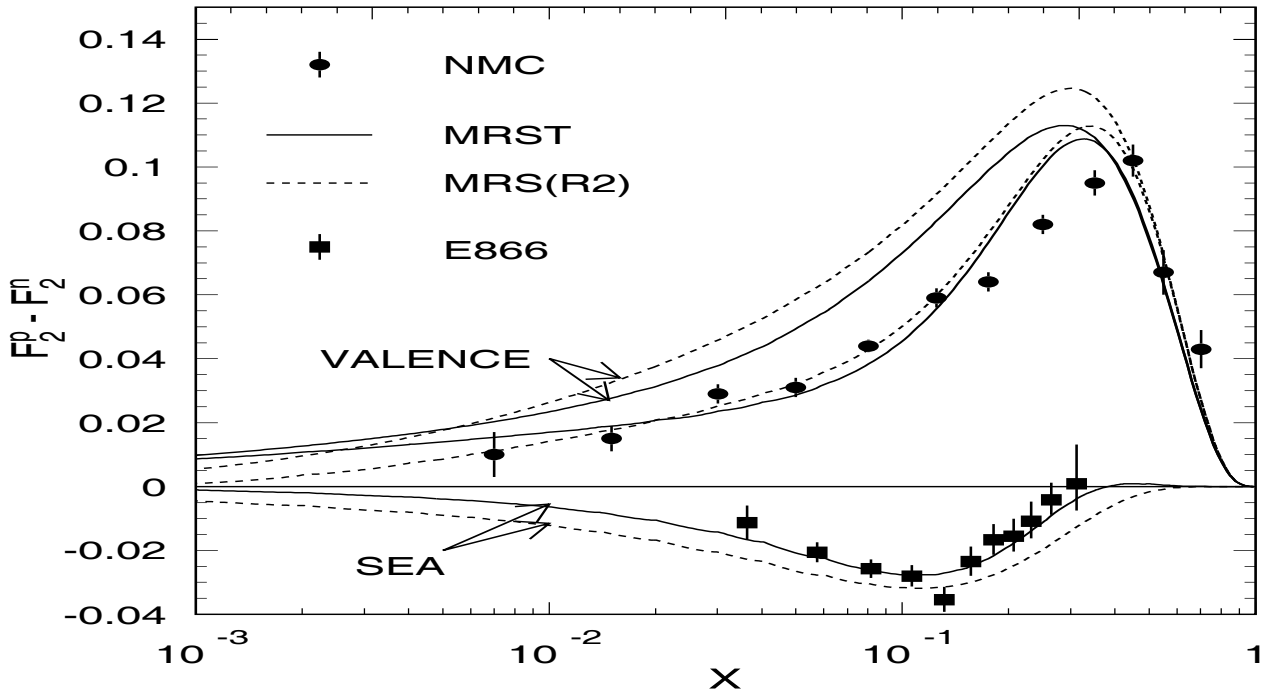

Fig. 8. The difference $F_2^{\gamma p} - F_2^{\gamma n}$ measured by NMC [39] at $Q^2 = 4$ GeV^2 compared with calculations using the MRS (R2) [40] (dashed) and the MRST [26] (solid) parton distributions. The E866 [41] Drell-Yan results on the sea quark contribution to the difference are shown at the same Q^2. For each set of parton distributions, the upper curve is the valence contribution to the difference, the lower curve is the sea contribution to the difference and the center curve is the sum of the two. Reproduced from Ref. [42] with permission from the *Annual Review of Nuclear and Particle Science*, Volume 49 © 1999 by Annual Reviews.

$$+ (4\overline{u}(x_1) + \overline{d}(x_1))(u(x_2) + d(x_2))\Big] \tag{50}$$

assuming charge symmetry. When x_1 is large, $\overline{u}(x_1), \overline{d}(x_1) \approx 0$ so that

$$\sigma_{p\mathrm{D}}^{\mathrm{DY}} \approx \frac{1}{9}(4u(x_1) + d(x_1))(\overline{u}(x_2) + \overline{d}(x_2)) \tag{51}$$

$$\sigma_{pp}^{\mathrm{DY}} \approx \frac{1}{9}(4u(x_1)\overline{u}(x_2) + d(x_1)\overline{d}(x_2)) \ . \tag{52}$$

The ratio of the pD and pp Drell-Yan cross sections when $x_1 \gg x_2$ is

$$\left.\frac{\sigma_{p\mathrm{D}}^{\mathrm{DY}}}{2\sigma_{pp}^{\mathrm{DY}}}\right|_{x_1 \gg x_2} \approx \frac{1}{2}\,\frac{1 + \frac{1}{4}\left[d(x_1)/u(x_1)\right]}{1 + \frac{1}{4}\left[d(x_1)/u(x_1)\right]\left[\overline{d}(x_2)/\overline{u}(x_2)\right]}\left(1 + \frac{\overline{d}(x_2)}{\overline{u}(x_2)}\right). \tag{53}$$

$\langle x_2 \rangle$	$\langle x_F \rangle$	$\langle x_1 \rangle$	$\langle p_T \rangle$	$\langle M_{\mu^+\mu^-} \rangle$	$\sigma_{pD}^{DY}/2\sigma_{pp}^{DY}$	$\overline{d}(x_2)/\overline{u}(x_2)$
0.036	0.537	0.573	0.92	5.5	1.039 ± 0.017	1.091 ± 0.037
0.057	0.441	0.498	1.03	6.5	1.079 ± 0.013	1.194 ± 0.031
0.082	0.369	0.451	1.13	7.4	1.113 ± 0.015	1.298 ± 0.039
0.106	0.294	0.400	1.18	7.9	1.133 ± 0.020	1.399 ± 0.057
0.132	0.244	0.376	1.21	8.5	1.196 ± 0.029	1.664 ± 0.096
0.156	0.220	0.376	1.21	9.3	1.124 ± 0.035	1.494 ± 0.119
0.182	0.192	0.374	1.20	9.9	1.091 ± 0.043	1.411 ± 0.142
0.207	0.166	0.373	1.19	10.6	1.098 ± 0.055	1.476 ± 0.195
0.231	0.134	0.365	1.18	11.1	1.055 ± 0.067	1.397 ± 0.250
0.264	0.095	0.359	1.18	11.8	0.967 ± 0.067	1.178 ± 0.239
0.312	0.044	0.356	1.12	12.8	0.881 ± 0.141	0.937 ± 0.539

Table 2
Ratio of Drell-Yan cross sections in deuterium to hydrogen, $\sigma_{pD}^{DY}/2\sigma_{pp}^{DY}$ and the ratio $\overline{d}/\overline{u}$ as a function of x_2. The average of the kinematic variables for each bin is also tabulated. The units of $\langle p_T \rangle$ and $\langle M_{\mu^+\mu^-} \rangle$ are GeV. Note that $\langle x_1 \rangle = \langle x_F \rangle + \langle x_2 \rangle$. Only statistical errors are shown. There is a 1% systematic uncertainty in all points. Modified from Ref. [41].

When $\overline{d} = \overline{u}$, the ratio is 1.

The first test of SU(2) flavor symmetry with the Drell-Yan process was made by the Fermilab E772 collaboration. They compared the production of Drell-Yan muon pairs from isoscalar targets to that from a neutron-rich target and set constraints on the difference between $\overline{u}$ and $\overline{d}$ in the range $0.04 \leq x \leq 0.27$ [48]. Later, the CERN NA51 collaboration [49] carried out a comparison of the Drell-Yan yield from hydrogen and deuterium at a single value of x with a 450 GeV proton beam and found

$$\left.\frac{\overline{u}_p}{\overline{d}_p}\right|_{\langle x \rangle = 0.18} = 0.51 \pm 0.04 \pm 0.05. \tag{54}$$

The most recent test has been made by the Fermilab E866 collaboration. They measured the Drell-Yan yield from an 800 GeV proton beam on liquid deuterium and hydrogen targets and extracted $\overline{d}/\overline{u}$ and $\overline{d} - \overline{u}$ in the proton for $0.020 < x < 0.345$. The resulting ratio of the Drell-Yan cross section per nucleon, Eq. (54), is given in Table 2 as a function of x_1 and x_2 [50,51]. The J/ψ and Υ resonance regions, $M_{\mu^+\mu^-} < 4.5$ GeV and $9.0 < M_{\mu^+\mu^-} < 10.7$ GeV respectively were excluded from the analysis. The data show that the Drell-Yan cross section per nucleon in pD interactions exceeds the Drell-Yan pp cross section over a range of x_2.

Since all the data do not satisfy $x_1 \gg x_2$, as necessary for Eq. (53) to hold, the ratio $\overline{d}(x_2)/\overline{u}(x_2)$ was extracted iteratively by calculating the leading order Drell-Yan cross sections using a set of parton distribution functions as input and adjusting $\overline{d}/\overline{u}$ until the calculated ratio agreed with the measured one. In this analysis the light anti-quark sum, $\overline{d}+\overline{u}$, the valence, and heavy quark distributions obtained in global analyses of CTEQ 4M [52] and MRS (R2) [40] were assumed to be valid. The extracted $\overline{d}/\overline{u}$ ratio is shown in Fig. 9 along with the corresponding CTEQ 4M and MRS (R2) ratios. For consistency,

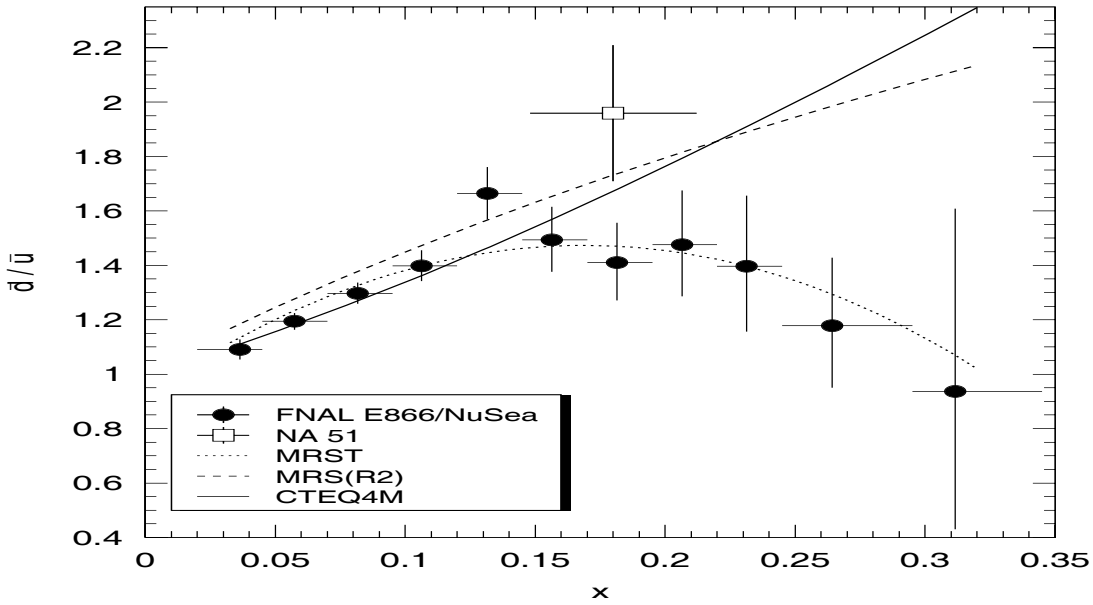

Fig. 9. The ratio of $\overline{d}/\overline{u}$ in the proton as a function of x extracted from the Fermilab E866 cross section ratio [41] along with the NA51 result [49]. The solid curve shows the CTEQ 4M ratio and the dashed curve is the MRS (R2) ratio. The MRST ratio is shown in the dotted curve. The E866 error bars are statistical only with an additional systematic uncertainty of ± 0.032 not indicated. Reproduced from Ref. [42] with permission from the *Annual Review of Nuclear and Particle Science*, Volume 49 © 1999 by Annual Reviews.

when $x_1 \leq 0.345$, the projectile ratio $\overline{d}(x_1)/\overline{u}(x_1)$ was assumed to be equal to that in the target proton while for $x_1 > 0.345$, $\overline{d}(x_1)/\overline{u}(x_1) \equiv 1$ was assumed. When this high x_1 assumption was relaxed, there was a negligible difference in the low x_2 results and only a 3% change in the largest x_2 bin. No significant dependence on the parton distribution set was observed.

A qualitative feature of the data, which contradicts the parton distributions studied, is the rapid decrease of $\overline{d}(x)/\overline{u}(x)$ to unity beyond $x = 0.2$. At the same value of x as measured by NA51, $x = 0.18$, the $\overline{d}/\overline{u}$ ratio is somewhat smaller than that obtained by NA51 [49]. Although the average value of $M^2_{\mu^+\mu^-}$ is different for the two data sets, the effects of evolution on the ratio is expected to be small.

To address the Gottfried sum rule violation, the extracted $\overline{d}/\overline{u}$ ratio is used with the CTEQ4M value of $\overline{d}+\overline{u}$ to obtain $\overline{d}-\overline{u}$ at the average $M_{\mu^+\mu^-}$ of the entire data set, $M_{\mu^+\mu^-} = 7.35$ GeV,

$$\overline{d}(x) - \overline{u}(x) = \frac{\overline{d}(x)/\overline{u}(x) - 1}{\overline{d}(x)/\overline{u}(x) + 1} \left[\overline{u}(x) + \overline{d}(x)\right] \ . \tag{55}$$

The integral of $\overline{d} - \overline{u}$ between $x_{\rm min}$ and 0.345 is calculated. Both the difference $\overline{d} - \overline{u}$ and the integral are shown in Fig. 10. The integral of the data is

$$\int_{0.02}^{0.345} dx[\overline{d}(x) - \overline{u}(x)] = 0.068 \pm 0.007 \pm 0.008 \ , \tag{56}$$

compared to 0.076 and 0.1 for the CTEQ 4M and MRS (R2) sets integrated over the same region. When the range $10^{-4} < x < 1$ is considered, CTEQ 4M gives a value of 0.108 for the integral while the MRS (R2) result is 0.160. Above $x = 0.345$, both the CTEQ 4M and MRS (R2) distributions contribute less than 0.002 to the total integral. However, significant contributions to the integral from the parton distribution functions arise in the unmeasured region below $x = 0.02$, 30-50%, depending on the set. Such a large $\overline{d}/\overline{u}$ asymmetry cannot arise from perturbative effects [53], especially since global fits to the parton distribution functions are tuned to accommodate the NMC, NA51, and, most recently, the E866 results (*e.g.* the MRST distributions [26] shown in the dotted curve in Fig. 9).

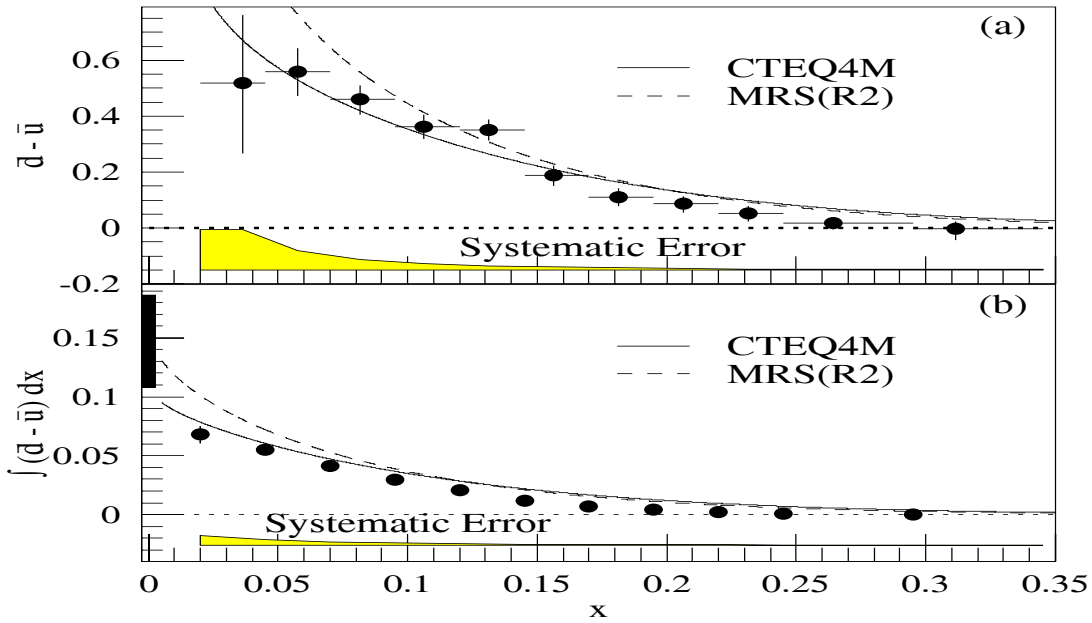

Fig. 10. Fermilab E866 values for (a) $\overline{d} - \overline{u}$ and (b) the integral $\int_x^{0.345} \left(\overline{d} - \overline{u}\right) dx'$ in the proton as a function of x. The curves represent the corresponding CTEQ 4M (solid) and MRS (R2) (dashed) results. The bar at 0.147 ± 0.039 on the left axis in (b) shows the value obtained by NMC for the integral from 0 to 1. Reproduced from Ref. [41]. Copyright 1998 by the American Physical Society.

A more complete picture of the individual contributions to $F_2^{\gamma p} - F_2^{\gamma n}$ emerges from the NMC and E866 data. Equation (44) gives the decomposition of the difference into valence and sea components. Figure 8 shows the NMC data on the total difference as a function of x along with the E866 contribution to the difference, $\propto \overline{u} - \overline{d}$. The curves show the total difference, the valence difference, $\propto u_p^v - d_p^v$, and the sea difference for two sets of parton distributions: MRS (R2), available before the E866 data, and MRST, which included the E866 data in the fit. Other relevant data in the MRST fit include an improved α_s determination from the CCFR data, the final NMC data on $F_2^{\gamma p}$, $F_2^{\gamma \mathrm{D}}$, and $F_2^{\gamma \mathrm{D}}/F_2^{\gamma p}$, and more precise information on the u/d ratio at large x from the Fermilab Tevatron [26]. The effect of these improvements on the global analysis is clear from the plot. While both parton distributions fit the NMC data, only the MRST set agrees with the E866 data. Note that reducing the sea contribution to Eq. (44) also significantly reduces the valence difference.

The most recent experimental study of flavor asymmetries and the Gottfried sum rule is by the HERMES collaboration [54] at HERA. They measured the charged pion yields in semi-inclusive DIS with a 27.5 GeV positron beam on hydrogen, deuterium, and ^{3}He gas jet targets in the kinematic range $0.02 < x < 0.3$ and $1 < Q^2 < 10$ GeV^2. Final-state hadron production requires the fragmentation function, $D_i^h(z)$, for parton i to produce hadron h with momentum fraction z of the initial parton momentum. The fragmentation functions $D_i^{\pi^\pm}(z)$ were extracted from the ^{3}He data and assumed to be independent of the target. The HERMES collaboration determined the ratio

$$\frac{\overline{d}(x) - \overline{u}(x)}{u(x) - d(x)} = \frac{J(z)\,[1 - r(x,z)] - [1 + r(x,z)]}{J(z)\,[1 - r(x,z)] + [1 + r(x,z)]} \tag{57}$$

where

$$r(x,z) = \frac{d\sigma_p^{\pi^-}(x,z)/dz - d\sigma_n^{\pi^-}(x,z)/dz}{d\sigma_p^{\pi^+}(x,z)/dz - d\sigma_n^{\pi^+}(x,z)/dz} \tag{58}$$

$$J(z) = \frac{3}{5}\left(\frac{1 + D_u^{\pi^-}(z)/D_u^{\pi^+}(z)}{1 - D_u^{\pi^-}(z)/D_u^{\pi^+}(z)}\right) \ . \tag{59}$$

The ratio $r(x,z)$ was determined from the hydrogen and deuterium data. No z dependence was observed in the measurement of the ratio in Eq. (57). Using the GRV 94 LO [27] parameterization of $u(x) - d(x)$, they found

$$\int_{0.02}^{0.3} dx\,(\overline{d}(x) - \overline{u}(x)) = 0.107 \pm 0.021 \pm 0.017 \ , \tag{60}$$

consistent with the E866 results, Eq. (56), even though the E866 results are obtained at $\langle M^2_{\mu^+\mu^-}\rangle = \langle Q^2\rangle = 54$ GeV^2 while $\langle Q^2\rangle = 2.3$ GeV^2 in HERMES, as shown in Fig. 11. The model calculations will be described later.

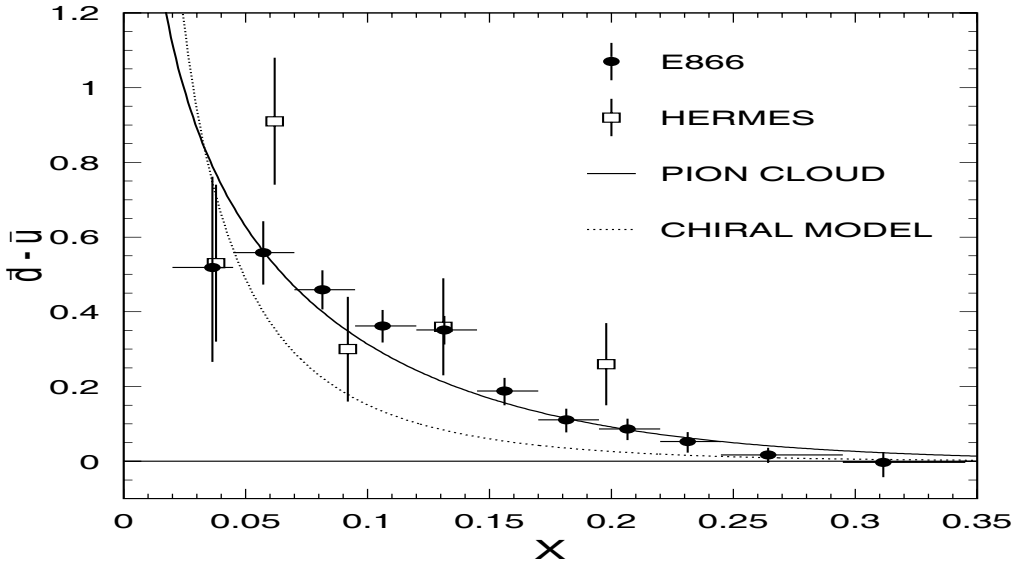

Fig. 11. The E866 difference $\overline{d} - \overline{u}$ at $\langle Q^2 \rangle = 54$ GeV^2 [41] is compared with predictions of meson cloud and chiral models. The HERMES data [54] are also shown. Reproduced from Ref. [42] with permission from the *Annual Review of Nuclear and Particle Science*, Volume 49 © 1999 by Annual Reviews.

An experiment following up the E866 results but with a lower energy proton beam, 120 GeV, has been proposed at Fermilab [55]. This experiment would be able to increase the statistics at $x > 0.1$ and obtain results at larger x than available with the higher energy beam.

Models which might account for SU(2) flavor asymmetry include meson clouds, Pauli blocking, chiral models, and charge symmetry breaking. These models will be discussed in the following sections. For a more extensive review of Gottfried sum rule violating mechanisms, see Ref. [56].

3.1.2 Meson cloud models

Clouds of virtual mesons were shown to play a role in the dynamics of chiral models of nucleon structure such as the cloudy bag. In these models, the proton wavefunction can fluctuate into *e.g.* $\pi^+ n$ and $\pi^0 p$. These virtual pion states have been used to explain the Δ decay width and the charge square radius of the neutron [56]. While the proton wavefunction is in the virtual πN state, the valence quarks and anti-quarks of the virtual state can contribute to the proton parton distributions. The original model [57] has been developed further recently to include a number of meson-baryon fluctuations with different form factors and meson-baryon-nucleon couplings at each vertex. Applications not only include the $\overline{d}/\overline{u}$ asymmetry but also quark and anti-quark asymmetries between strange and heavier quarks. We introduce the model here and will discuss other applications in later sections.

The amplitude of the Sullivan process is obtained from the DIS amplitude by replacing the $\gamma^\star p$ vertex in the DIS formalism by *e.g.* a πNN vertex

$$\mathcal{M}_\mu = < X|eJ_\mu(0)|\pi > \frac{1}{p_\pi^2 - m_\pi^2} F_{\pi NN}(t)\,\overline{u}(p')\,i\,g_{_{\pi NN}}\,\widetilde{\phi}_\pi^* \cdot \widetilde{\tau}\,\gamma_5\,u(p) \quad , \tag{61}$$

including the form factor, $F_{\pi NN}(t)$, coupling constant, $g_{_{\pi NN}}$, and $\pi - N$ isospin coupling $\widetilde{\phi}_\pi^* \cdot \widetilde{\tau}$. Replacing p by p_π and M with m_π in Eq. (9), one obtains

$$\begin{aligned} F_2^{\gamma\pi}(x) &= |\widetilde{\phi}_\pi^* \cdot \widetilde{\tau}|^2 \frac{g_{_{\pi NN}}^2}{16\pi^2} \int\limits_x^1 dy\, y\, F_2^\pi\left(\frac{x}{y}\right) \int\limits_{-\infty}^{t_m^N} \frac{-t\,dt}{(t-m_\pi^2)^2}\ |F_{\pi NN}(t)|^2 \\ &= |\widetilde{\phi}_\pi^* \cdot \widetilde{\tau}|^2 \int\limits_x^1 dy\, F_2^\pi\left(\frac{x}{y}\right) f_{MB}(y)\ , \end{aligned} \tag{62}$$

where $t_m^N = -m_N^2 y^2/(1-y)$. Thus $F_2^{\gamma\pi}$ is the convolution of the pion structure function with the light-cone momentum distribution of the pion, $f_{MB}(y)$ [58–62], normalized by the isospin coupling. The same formalism is used for quark and anti-quark distributions.

The direct interaction of a photon with the meson cloud surrounding a nucleon does not contribute to the Gottfried sum. However, it does not necessarily follow that the mesons do not contribute to the Gottfried sum and the $\overline{u} - \overline{d}$ distribution, as discussed below. Two general approaches have been used depending on whether [58,59] or not [60–62] the interaction of the recoil baryon with the virtual photon is included. Both are in principle the same. The main differences are in the number of meson and baryon states included.

The largest number of contributions has been considered in Ref. [59]. They include πN, ρN, ωN, σN, ηN, $\pi\Delta$, $\rho\Delta$, $K\Lambda$, $K^*\Lambda$, $K\Sigma$, $K^*\Sigma$, KY^*, and K^*Y^* states coupling to the nucleon. In most models however, only the πN [60] and $\pi\Delta$ [61] nucleon couplings are included. Since the pions alone do not contribute to the Gottfried sum rule directly, the πNN and $\pi N\Delta$ contributions to the sum rule can be written as [58]

$$F_2^{\gamma p}(x) - F_2^{\gamma n}(x) = Z\left\{\frac{x}{3}[u^v(x) - d^v(x)]\right. \tag{63}$$

$$\left. -\frac{1}{3}\int\limits_0^{1-x} \frac{dy}{1-y}\left(\frac{x}{3} f_{\pi N}(y)\,[u^v(y') - d^v(y')] - \frac{1}{2}\frac{10x}{3} f_{\pi\Delta}(y) d^v(y')\right)\right\} \quad . \tag{64}$$

where $y' = x/(1-y)$ and $f_{\pi N(\Delta)}(y)$ are meson-baryon light-cone momentum distributions. The valence normalization Z is defined as $Z = 1/(1 + N_\pi + \Delta_\pi)$ where the probability of finding a pion in *e.g.* the πNN state is $N_\pi = \int_0^1 dy f_{\pi N}(y)$.

The light-cone momentum distribution of the virtual meson in the nucleon is the sum over the meson-baryon momentum distributions

$$f_M(y) \;=\; \sum_B f_{MB}(y) \quad , \tag{65}$$

with

$$f_{MB}(y) = \frac{g^2_{MNB}}{16\pi^2}\, y \int\limits_{-\infty}^{t_m^B} dt\, \frac{\mathcal{I}(t, m_N, m_B)}{(t - m_M^2)^2}\, [F_{MNB}(t)]^2 \tag{66}$$

as defined from Eq. (62). The meson-baryon momentum distributions $f_{MB}(y)$ are the probabilities of finding meson M in an MB configuration in the nucleon with fraction y of the nucleon momentum in the infinite momentum frame. These distributions must be related to the baryon distributions in the nucleon in the same configuration, $f_{BM}(y)$, by

$$f_{MB}(y) = f_{BM}(1 - y) \tag{67}$$

to conserve probability [63]. The t-dependent function $\mathcal{I}(t, m_N, m_B)$ has two forms,

$$\mathcal{I}(t, m_N, m_B) = \begin{cases} -\,t + (m_B - m_N)^2 & \text{for } B \in \mathbf{8} \\ \frac{\left[(m_B+m_N)^2 - t\right]^2 \left[(m_B - m_N)^2 - t\right]}{12\, m_N^2\, m_B^2} & \text{for } B \in \mathbf{10}\ , \end{cases} \tag{68}$$

depending whether the baryon B is part of the octet or the decuplet. The upper limit of the integral when $B \neq N$ is given by

$$t_m^B = m_N^2\, y - \frac{m_B^2\, y}{1 - y}\ . \tag{69}$$

Several functional forms, including monopole, dipole, and exponential, have been assumed for the meson-baryon vertex form factor,

$$F_{MNB}(t) = \begin{cases} \frac{\Lambda_m^2 - m_M^2}{\Lambda_m^2 - t} & \text{monopole} \\ \left(\frac{\Lambda_d^2 - m_M^2}{\Lambda_d^2 - t}\right)^2 & \text{dipole} \\ e^{(t - m_M^2)/\Lambda_e^2} & \text{exponential}\ . \end{cases} \tag{70}$$

It has recently been pointed out that in the covariant formulation of Eq. (66) with t-dependent form factors, the probability conservation of Eq. (67) could not always be achieved [63]. However, if the calculation is done with light-cone wavefunctions, *e.g.* the dipole form of $F_{MNB}(t)$ above is replaced by

$[(\Lambda_d^2 + m_M^2)/(\Lambda_d^2 + s_{\pi N})]^2$ where $s_{\pi N}$ is the square of the pion-nucleon center of mass energy, probability conservation is satisfied [63].

Studies have been made of the hardness of the form factor. A hard form factor with a monopole cutoff $1.0 < \Lambda_m < 1.4$ GeV is needed to explain the deuteron D-state admixture and nucleon-nucleon scattering [56] although more recent NN potential models allow for softer cutoffs, $\Lambda_m \sim 0.8$ GeV [64]. Softer cutoffs are also generally obtained in quark models, $\Lambda_m \approx 0.6$ GeV in the cloudy-bag model [65] and $0.7 < \Lambda_m < 1.0$ GeV in flux-tube type models [66]. An even softer cutoff, $\Lambda_m < 0.5$ GeV [67], arises from analyses of the flavor asymmetric distribution $(\overline{u} + \overline{d})/2 - \overline{s}$. However, later analyses of this flavor asymmetric distribution with more recent data resulted in a slightly larger cutoff, $\Lambda_m \approx 0.6$ GeV [61], which could be consistent with the quark model estimates. As more mesons and baryons are added to the calculation, the cutoff becomes larger, $\Lambda_m \approx 0.74$ GeV, because the probability to find the bare nucleon is reduced due to the presence of the meson clouds. The dipole and exponential cutoffs are related to the monopole cutoff by $\Lambda_m = 0.62\Lambda_d = 0.78\Lambda_e$ [61].

Mesonic contributions to an anti-quark distribution in the nucleon are given by the convolution of the corresponding valence anti-quark distribution in a meson with the light-cone momentum distribution of the meson in the MB state. The contributions are given by the equation

$$x\,\overline{q}_N(x,Q^2) = \sum_{MB} \alpha^q_{MB} \int_x^1 dy\, f_{MB}(y)\, \frac{x}{y}\, \overline{q}_M\left(\frac{x}{y}, Q^2\right) \quad , \tag{71}$$

where the summations are over combinations of meson $M = (\pi,\, K)$ and baryon $B = (N,\, \Delta,\, \Lambda,\, \Sigma,\, \Sigma^*)$ states and α^q_{MB} are spin-flavor SU(6) Clebsch-Gordon coefficients. Equation (71) corresponds to Eq. (62) for $F_2^{\gamma\pi}$.

From Eq. (64), the Gottfried sum becomes $I_G = (Z/3)(1 - N_\pi/3 + 5\Delta_\pi/3)$. According to this equation, the failure of the sum rule is due not to the photon interaction with the virtual pion but to the interaction with the recoil baryons.

When contributions from light meson and baryon states beyond πN and $\pi\Delta$ are included in Eq. (64), the Gottfried integral becomes

$$I_G = \frac{1}{3}\,(Z + \sum_i A_i)\ , \quad \text{with} \quad A_i = \int_0^1 dx\,(u_i + \overline{u}_i - d_i - \overline{d}_i)_{\rm Sull} \tag{72}$$

where A_i are the x integrated meson and baryon contributions to the quark and anti-quark distributions in the nucleons. These results, given in Table 3, should be multiplied by the probabilities of finding the meson-baryon states in the nucleon. Although the nucleon "core" satisfies the valence quark sum $\int dx(u^v - d^v) = 1/3$, its probability is reduced by the normalization factor Z due to the presence of the virtual MB states. In this approach, no contribution from pions or rho mesons enters the sum and the

violation comes from the normalization factor Z and the baryon contributions because $u + \overline{u} - d - \overline{d}$ vanishes in the pion.

MB	A_i^M	A_i^B	B_i^M	B_i^B
πN	0	$-1/3$	$-2/3$	0
$\pi\Delta$	0	$5/3$	$1/3$	0
ρN	0	$-1/3$	$-2/3$	0
$\rho\Delta$	0	$5/3$	$1/3$	0
ωN	0	1	0	0
σN	0	1	0	0
ηN	0	1	0	0
$K\Lambda$	1	0	0	0
$K^*\Lambda$	1	0	0	0
$K\Sigma$	$-1/3$	$4/3$	0	0
$K^*\Sigma$	$-1/3$	$4/3$	0	0
KY^*	$-1/3$	$4/3$	0	0
K^*Y^*	$-1/3$	$4/3$	0	0

Table 3
Coefficients A_i and B_i in two different descriptions [59]. Reproduced from Ref. [56] with permission from Elsevier Science.

The sum could be written in a different form to satisfy the valence quark sum exactly. Part of the meson and baryon contributions can be factored into the valence sum, 1/3, and the deviation from 1/3 is identified with the flavor asymmetry due to the Sullivan processes from the meson cloud, $\int dx(\overline{u}-\overline{d})_{\rm Sull}$ [61,59,62]. The Gottfried integral then becomes

$$I_G = \frac{1}{3}\left(1 + \sum_i B_i\right) , \quad \text{with} \quad B_i = \int_0^1 dx\,(\overline{u}_i - \overline{d}_i)_{\rm Sull} \quad . \tag{73}$$

The coefficients B_i in Eq. (73) are also given in Table 3. The virtual πB states contribute to the renormalization of the valence-quark distributions. Therefore the pionic renormalization contributions may be factored into the valence quark sum factor in Eq. (73) [61]. Then the pion contributes to the deviation from the Gottfried sum. Because flavor symmetry is assumed in the MB states, only the pions and rho mesons contribute to the violation. Thus the two different mesonic descriptions are equivalent.

Although there are slight model differences, the meson-cloud approach is successful in explaining the

major part of the NMC and E866 results. The solid curve in Fig. 11 shows a calculation with the meson-cloud model with πNN and $\pi N\Delta$ contributions. A dipole form factor is used with $\Lambda_d = 1$ GeV for the πNN coupling and 0.8 GeV for the $\pi N\Delta$ coupling, corresponding to $\Lambda_m = 0.62$ GeV and 0.5 GeV respectively. Reasonably good agreement with the E866 $\overline{d} - \overline{u}$ data is found [42].

Even though meson cloud models, such as the calculation shown in Fig. 11, may successfully explain the difference $\overline{d} - \overline{u}$, they usually have trouble reproducing the ratio $\overline{d}/\overline{u}$. An approach that has had relative success in obtaining agreement with both the difference and the ratio is the inclusion of a perturbative component in the meson cloud [68,69]. The analysis of Ref. [68], based on the assumption that the proton is composed of three dressed quarks or valons in the infinite momentum frame [70], is discussed in more detail here. One of the valons may emit a gluon which subsequently decays into a $q\overline{q}$ pair. This $q\overline{q}$ pair can then nonperturbatively rearrange itself with the valons of the proton into a meson-baryon bound state. The flavor symmetric GRV distributions [71] are assumed to be the underlying perturbative sea.

The ratio $\overline{d}/\overline{u}$ is computed assuming two components in the sea, the nonperturbative meson cloud and a perturbative contribution,

$$\frac{\overline{d}(x,Q^2)}{\overline{u}(x,Q^2)} = \frac{\overline{d}^{\rm NP}(x,Q^2) + \overline{q}^{\rm P}(x,Q^2)}{\overline{u}^{\rm NP}(x,Q^2) + \overline{q}^{\rm P}(x,Q^2)} \ . \tag{74}$$

The difference $\overline{d} - \overline{u}$ is extracted from the $\overline{d}/\overline{u}$ ratio according to Eq. (55), as also done in the E866 analysis [41], rather than from the difference between the numerator and denominator of Eq. (74). The perturbative anti-quark distribution in Eq. (74) is taken from the GRV LO symmetric sea [71].

The nonperturbative $\overline{u}$ and $\overline{d}$ distributions are calculated in the meson cloud model assuming that the $\overline{d}$ is generated from $\pi^+ n$ and $\pi^+\Delta^0$ fluctuations while the $\overline{u}$ arises from $\pi^-\Delta^{++}$ fluctuations,

$$\overline{d}^{\rm NP}(x,Q_V^2) = \int_x^1 \frac{dy}{y}\left[P_{\pi^+ n}(y) + \frac{1}{6}P_{\pi^+\Delta^0}(y)\right]\overline{d}_\pi\left(\frac{x}{y},Q_V^2\right) \tag{75}$$

$$\overline{u}^{\rm NP}(x,Q_V^2) = \int_x^1 \frac{dy}{y}\frac{1}{2}P_{\pi^-\Delta^{++}}(y)\overline{u}_\pi\left(\frac{x}{y},Q_V^2\right) \ . \tag{76}$$

The fluctuations containing π^0 mesons, *e.g.* $\pi^0\Delta^+$, are not included because flavor singlets such as $\pi^0 \sim d\overline{d} - u\overline{u}$ are assumed to be more likely to annihilate than to recombine with the valons in the proton. The $\overline{d}_\pi$ and $\overline{u}_\pi$ valence distributions are taken from the GRV LO pion distributions [72]. The pion probability densities from πB states are calculated by the convolution of a recombination function associated with pion formation, $R(x,y,z)$,

$$R(x,y,z) = \gamma\frac{yz}{x}\delta(x-y-z) \ , \tag{77}$$

and a valon quark distribution function, $F(y,z)$,

$$F(x,y) = \beta y v(y) z\overline{q}(z)(1-y-z)^a \ , \tag{78}$$

so that

$$P_{\pi B}(x) = \int_0^1 \frac{dy}{y} \int_0^1 \frac{dz}{z} F(y,z) R(x,y,z) \ . \tag{79}$$

In Eq. (78), the exponent a is fixed by requiring that the pion and baryon in the fluctuation have the same velocity, resulting in $a = 12.9$ for $\pi^+ n$ and 18 for the $\pi\Delta$ fluctuations. The quark distribution is calculated from the decays of the valon to gluons, $v \to v + g$ and gluon splitting to $q\overline{q}$, $g \to q + \overline{q}$,

$$q(x,Q_V^2) = \overline{q}(x,Q_V^2) = N \frac{\alpha_s^2(Q_V^2)}{4\pi^2} \int_x^1 \frac{dy}{y} P_{qg}\left(\frac{x}{y}\right) \int_y^1 \frac{dz}{z} P_{gq}\left(\frac{y}{z}\right) v(z) \tag{80}$$

where $Q_V^2 = 0.64$ GeV^2 [70,73] and P_{qg} and P_{gq} are the valon and gluon splitting functions for QCD evolution, as in Eqs. (36) and (37). The valon distribution, independent of Q^2, is $v(x) = (105/16)\sqrt{x}(1-x)^2$. The normalization constants N, γ, and β are fixed from the difference $\overline{d} - \overline{u}$ in Eq. (55).

The results for the ratio, Eq. (74), and the difference, Eq. (55), are shown in Fig. 12. The solid curve is the result at the valon scale $Q^2 = 0.64$ GeV^2 while the dashed line is a pseudo-evolved result at $Q^2 = 54$ GeV^2 [68]. Both calculations are in reasonable agreement with the measurements due to the presence of the perturbative component. The calculation describes the ratio as well as the difference because the valon model fixes the normalization of the perturbative component while the meson cloud model shifts the contributions to $\overline{d}$ and $\overline{u}$ between the meson and baryon components. Thus the meson cloud model alone can only describe the difference. Even better agreement is obtained if the valence distribution in the pion in Eqs. (75) and (76) is multiplied by an additional power of x [68]. This modified pion valence distribution is not excluded because the low x pion parton distributions are not well known.

3.1.3 Effects of Pauli blocking

The Pauli exclusion principle forbids two fermions from having identical quantum numbers. Thus, if a quark in the nucleon wavefunction has a certain set of quantum numbers, a q in a virtual $q\overline{q}$ state cannot be generated in the sea if it has the same quantum numbers as an already existing q. The new q is Pauli blocked. Because the proton has two valence u quarks and one valence d quark, $u\overline{u}$ pair creation is more likely to be Pauli-blocked than the $d\overline{d}$ pair, resulting in a difference between $\overline{u}$ and $\overline{d}$, as first suggested by Field and Feynman [74].

Pauli blocking effects in the nucleon have been calculated in $1+1$ dimensions using the MIT bag model

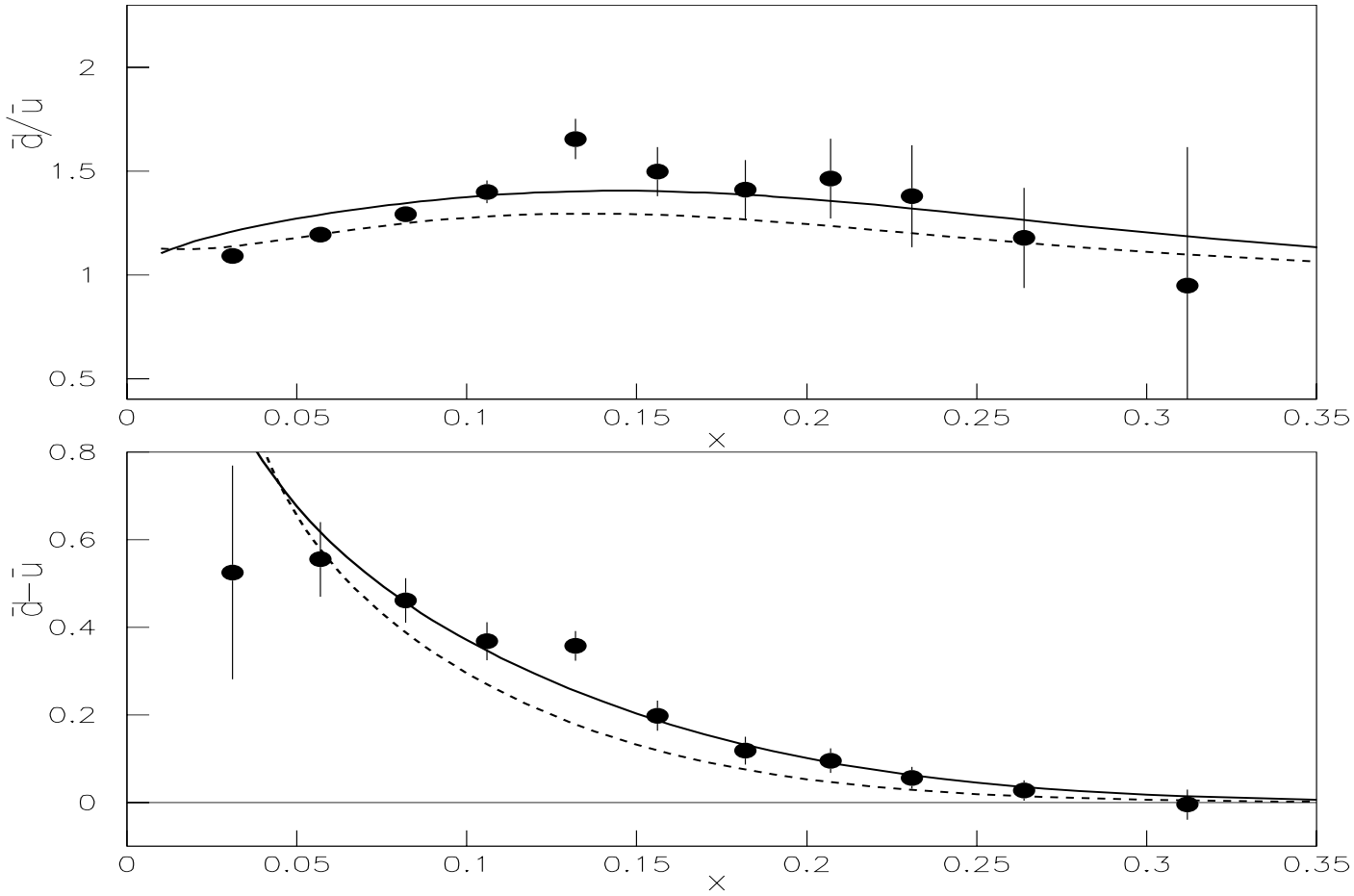

Fig. 12. The E866 ratio $\overline{d}/\overline{u}$ and difference $\overline{d}-\overline{u}$ are compared to calculations at $Q^2 = 54$ GeV^2 [41] with the meson cloud model of Ref. [68]. The solid curves show the $\overline{u}^{\rm NP}$ and $\overline{d}^{\rm NP}$ distributions without Q^2 evolution (solid curves) and with pseudo-evolution (dashed curves). Reproduced from Ref. [68]. Copyright 2000 by the American Physical Society.

[58,75]. In $1+1$ dimensions, there are three color states for each flavor. In the ground state, two of the three u-quark states and one of the three d-quark states are occupied. Only one more u quark can be added to the ground state, but two more d quarks can be accommodated. Since the additional u or d quarks in the ground state would be accompanied by $\overline{u}$ and $\overline{d}$ anti-quarks, the expected sea quark asymmetry is rather large, $\overline{d} = 2\overline{u}$.

No $3+1$ dimensional calculation exists at this time so that the Pauli blocking effects are obtained from a naive counting estimate. In the $3+1$ dimensional case, there are six states, three color and two spin, in the ground state. There are four available ground states for u quarks and five states for d quarks, so that $\overline{d} = 5\overline{u}/4$. Because no valence anti-quarks exist in the bag, the sea quark contribution comes from a quark being inserted, interacting in the bag, and then being removed. Therefore, the $\overline{d}$ excess is

related to the distribution of a four-quark intermediate state $f_4(x)$

$$\int_0^1 dx\,[\overline{d}(x) - \overline{u}(x)] = \int_0^1 dx f_4(x) = 1 - P_2 \quad , \tag{81}$$

where P_2 is the integral of a distribution associated with a two-quark intermediate state. Because the $\overline{u}$ and $\overline{d}$ distributions have not been calculated, the Pauli contributions were assumed to be $x^A(1-x)^B$ in Ref. [58,63]. The constant A is chosen to match the small x behavior of the valence distributions used, and a large exponent, $B = 7$, was chosen so that Pauli blocking contributes only at small x. This value of B is consistent with counting rules for sea quarks [76]. The overall normalization is not determined theoretically but $1 - P_2$ is expected to be ≈ 0.25 because of the naive counting estimate in $3 + 1$ dimensions.

Pauli blocking effects could in principal, produce the $\overline{d}$ over $\overline{u}$ excess. Unfortunately, the qualitative x dependence of the effect is only calculated in 1+1 dimensions. It was suggested that a 10% Pauli-blocking effect combined with pionic contributions from the meson cloud could explain the difference $F_2^{\gamma p} - F_2^{\gamma n}$ [58] and the E866 $\overline{d}/\overline{u}$ ratio and $\overline{d} - \overline{u}$ difference relatively well [69]. However, if antisymmetrization of the quark wavefunctions is included, the conclusion could change dramatically [75]. The same u-valence excess which suppresses the $u\overline{u}$ pair creation produces extra $u\overline{u}$ pairs in the antisymmetrization of the second u. This additional source of $\overline{u}$ could cause $\overline{u} > \overline{d}$, in contradiction to the NMC and E866 results [75].

3.1.4 Chiral models

Several different types of chiral models have been proposed to explain the Gottfried sum rule violation. In a chiral field theory with quarks, gluons, and Goldstone bosons (pions) [77–80], flavor asymmetries arise from virtual photon interactions with the pions. On the other hand, in chiral soliton models [81–83] a portion of the isospin of the nucleon is carried by pions. The Gottfried sum rule violation is then determined from the moments of inertia of the nucleons and pions. An extension of the linear sigma model to the Gottfried sum rule has also been proposed [84–86]. In this section, only the chiral field theory approach is briefly described. For more details, see Ref. [56].

Because chiral symmetry is spontaneously broken, any description of low energy hadron properties should include this symmetry breaking. The effective Lagrangian in chiral field theory is [56]

$$\mathcal{L} = \overline{\psi}(iD_\mu + V_\mu)\gamma^\mu\psi + ig_{_A}\overline{\psi}A_\mu\gamma^\mu\gamma_5\psi + \cdots \quad , \tag{82}$$

where ψ is the quark field and D_μ is the covariant derivative. The vector and axial-vector currents are

defined in terms of Goldstone bosons so that

$$\begin{pmatrix} V_\mu \\ A_\mu \end{pmatrix} = \frac{1}{2}(\xi^\dagger \partial_\mu \xi \pm \xi\, \partial_\mu \xi^\dagger) \quad , \tag{83}$$

where $\xi = e^{(i\Pi/f)}$ and the +-sign goes with the vector current. The meson matrix $\Pi = q \otimes \overline{q}$ is

$$\Pi = \frac{1}{\sqrt{2}} \begin{pmatrix} \pi^0/\sqrt{2} + \eta/\sqrt{6} & \pi^+ & K^+ \\ \pi^- & -\pi^0/\sqrt{2} + \eta/\sqrt{6} & K^0 \\ K^- & \overline{K}^0 & -2\eta/\sqrt{6} \end{pmatrix} \quad . \tag{84}$$

Expanding V_μ and A_μ in powers of Π/f gives $V_\mu = O(\Pi/f)^2$ and $A_\mu = i\partial_\mu \Pi/f + O(\Pi/f)^2$. Then the quark-boson interaction, proportional to A_μ, becomes $\mathcal{L}_{\Pi q} = -(g_{_A}/f)\overline{\psi}\partial_\mu \Pi \gamma^\mu \gamma_5 \psi$.

The Gottfried sum rule violation arises from $q \to q\pi$ splittings where the final-state pion is massless. The u quark can split into either $u \to \pi^+ d \to u\overline{d}d$ or $u \to \pi^0 u \to u(\overline{u}u)$, $u(\overline{d}d)$. Thus if a is the splitting probability for $u \to \pi^+ d$,

$$u \to a\pi^+ + ad + \frac{a}{2}\pi^0 + \frac{a}{2}u = \frac{a}{4}\left[7u + 5d + \overline{u} + 5\overline{d}\right] \quad . \tag{85}$$

Likewise,

$$d \to a\pi^- + au + \frac{a}{2}\pi^0 + \frac{a}{2}d = \frac{a}{4}\left[5u + 7d + 5\overline{u} + \overline{d}\right] \quad . \tag{86}$$

The probability a is determined from the splitting function, $P_{\Pi q' \leftarrow q}$, defined as

$$P_{\Pi q' \leftarrow q}(z) = \frac{g_{_A}^2}{f^2} \frac{(m_q + m_{q'})^2}{32\pi^2} z \int_{-\Lambda^2}^{t_m} dt \, \frac{(m_q - m_{q'})^2 - t}{(t - M_\Pi^2)^2} \quad , \tag{87}$$

where, as in the meson-cloud model, $t_m = m_q^2 z - m_{q'}^2 z/(1-z)$, similar to Eq. (66), and $\Lambda \approx$1.169 GeV. This large value of Λ is assumed to be the scale at which chiral symmetry is broken. Integrating over t for the process $u \to \pi^+ d$ gives

$$\begin{aligned} a = & \frac{g_{_A}^2\, m_u^2}{8\pi^2 f^2} \int_0^1 dz\, \theta(\Lambda^2 - \tau(z))\, z \left\{ \ln\left[\frac{\Lambda^2 + M_\pi^2}{\tau(z) + M_\pi^2}\right] \right. \\ & \left. + \; M_\pi^2 \left[\frac{1}{\Lambda^2 + M_\pi^2} - \frac{1}{\tau(z) + M_\pi^2}\right] \right\} \end{aligned} \tag{88}$$

where $\theta(x) = 1$ when $x > 0$ and zero otherwise. Since $m_u \approx m_d$, $\tau(z) = -t_m(m_q = m_{q'}) = m_u^2 z^2/(1-z)$ With $\Lambda \approx 1.169$ GeV, the Gottfried integral becomes $I_G = (1-2a)/3 = 0.278$. Increasing Λ decreases I_G.

The anti-quark distribution as a function of x is [77,78]

$$\overline{q}_i(x) = \sum_{j,k,l} \left(\delta_{jl}\delta_{ik} - \frac{\delta_{jk}\delta_{il}}{n_f} \right)^2 \int_x^1 \frac{dy}{y} \int_{x/y}^1 \frac{dz}{z}\, \overline{q}_i^{(\Pi)}\left(\frac{x}{yz}\right) P_{\Pi k \leftarrow j}(z)\, q_{v\,j}^N(y) \tag{89}$$

where the indices j, k, and l are summed over flavor. The $\overline{d} - \overline{u}$ difference $\overline{d} - \overline{u}$ is calculated at $Q^2 = 54$ GeV^2 using the formulation of Szczurek *et al.* [80] and compared with the E866 and HERMES data in Fig. 10. The difference in the chiral approach is concentrated in the small x region, even more so than in the meson-cloud model, as seen in the dashed curve of Fig. 10. This concentration at low x occurs because pions are coupled to constituent quarks in the chiral model and the constituent quarks carry a smaller fraction of the nucleon momentum than the virtual pions in the meson cloud.

3.1.5 Charge Symmetry Violation

Charge symmetry, Eq. (24), is respected to a high degree of precision in nuclear physics with most low energy tests finding that it holds to $\approx 1\%$ in reaction amplitudes [87]. Thus, charge symmetry is generally assumed to be valid in strong interactions and all global analyses of parton distributions [88].

Experimental verification of charge symmetry is difficult for two reasons: any violation effects are expected to be small and charge symmetry violation may mix with or be misinterpreted as flavor symmetry violation. Thus, Ma [89] suggested that the interpretation of the Gottfried sum rule violation and the Drell-Yan ratio as flavor symmetry violation could instead be the result of charge symmetry violation. Given such ambiguities, experiments that could distinguish between charge and flavor symmetry violation are needed. Some have already been proposed [90].

Possible effects of charge symmetry violation have recently been examined by Boros *et al.* [21]. They define charge symmetry violating ,CSV, distributions

$$\delta u(x) = u_p(x) - d_n(x) \qquad \delta d(x) = d_p(x) - u_n(x) \tag{90}$$

$$\delta\overline{u}(x) = \overline{u}_p(x) - \overline{d}_n(x) \qquad \delta\overline{d}(x) = \overline{d}_p(x) - \overline{u}_n(x)\ , \tag{91}$$

which would disappear if charge symmetry holds. The isoscalar structure functions defined in Eqs. (29)-(33) are then modified to include the violation [21]

$$F_{2\,\mathrm{CSV}}^{\gamma N_0}(x) = F_2^{\gamma N_0} - \frac{x}{18}[4(\delta d(x) + \delta\overline{d}(x)) + \delta u(x) + \delta\overline{u}(x)] \tag{92}$$

$$F_{2\,\mathrm{CSV}}^{W^+N_0}(x) = F_2^{W^+N_0}(x) - x[\delta u(x) + \delta\overline{d}(x)] \tag{93}$$

$$xF_{3\,\mathrm{CSV}}^{W^+N_0}(x) = xF_3^{W^+N_0}(x) - x[\delta u(x) - \delta\overline{d}(x)] \tag{94}$$

$$F_{2\,\mathrm{CSV}}^{W^-N_0}(x) = F_2^{W^-N_0}(x) - x[\delta d(x) + \delta\overline{u}(x)] \tag{95}$$

$$xF_{3\,\mathrm{CSV}}^{W^-N_0}(x) = xF_3^{W^-N_0}(x) - x[\delta d(x) - \delta\overline{u}(x)] \tag{96}$$

Likewise, one can form a charge ratio relating the neutrino structure function to the charged lepton structure function similar to Eq. (39) [21]

$$\begin{aligned} R_c(x) &\equiv \frac{F_2^{\gamma N_0}(x)}{\frac{5}{18}F_2^{W^+N_0}(x) - \frac{x}{6}(s(x)+\overline{s}(x))} \\ &\approx 1 - \frac{s(x)-\overline{s}(x)}{\overline{Q}(x)} + \frac{4\delta u(x) - \delta\overline{u}(x) - 4\delta d(x) + \delta\overline{d}(x)}{5\overline{Q}(x)} \end{aligned} \tag{97}$$

where $\overline{Q}(x) \equiv \sum_{q=u,d,s}(q(x)+\overline{q}(x)) - \frac{3}{5}(s(x)+\overline{s}(x))$. The denominator of Eq. (97) was expanded retaining only leading terms in the small quantities $s(x)-\overline{s}(x)$ and $\delta q(x)$. If $R_c(x) \neq 1$ at any x, then either $s(x) \neq \overline{s}(x)$ or charge symmetry is violated. The CCFR collaboration compared their neutrino structure function $F_2^{W^+\mathrm{Fe}}$ [22] with $F_2^{\gamma\mathrm{D}}$ measured by the NMC collaboration [13] and found that for $x < 0.1$, $R_c \approx 0.9$ in the region of Q^2 overlap between the two experiments. When nuclear shadowing corrections were applied to the targets, R_c remained inconsistent with unity. It therefore appears that in this region, $s(x) \neq \overline{s}(x)$ or charge symmetry is violated.

The CCFR data allow $s(x)$ and $\overline{s}(x)$ to be determined independently. Such an analysis by the CCFR collaboration [22] will be discussed in more detail in Section 3.2.1. Here, the CCFR dimuon data were used to set limits on charge symmetry violation effects [21]. Dimuon production from ν_μ and $\overline{\nu}_\mu$ interactions with the strange nucleon sea is defined as

$$xs^{\mu\mu}(x) = \frac{1}{2}\,x\,[s(x)+\overline{s}(x)] + \frac{1}{2}(2\beta'-1)\,x\,[s(x)-\overline{s}(x)]\ , \tag{98}$$

where experimentally $\beta' = N_\nu^{\mu\mu}/(N_\nu^{\mu\mu} + N_{\overline{\nu}}^{\mu\mu}) \approx \beta$ in Eq. (39). Combining Eq. (98) with Eq. (39), one can simultaneously solve for $s(x)$ and $\overline{s}(x)$. The anti-strange distribution determined in this fashion is negative and thus unphysical [21]. If charge symmetry is assumed to be violated, the difference between Eqs. (39) and (98) can be used to estimate the size of the violation [21]

$$\begin{aligned} &\frac{5}{6}F_2^{W^\pm N_0}(x) - 3F_2^{\gamma N_0}(x) - xs^{\mu\mu}(x) = \frac{x(2\beta-1)}{3}[s(x)-\overline{s}(x)] \\ &\quad + \frac{x}{6}\left[(5\beta-1)(\delta d(x)-\delta u(x)) + (4-5\beta)(\delta\overline{d}(x)-\delta\overline{u}(x))\right] \\ &\approx \frac{x(2\beta-1)}{3}[s(x)-\overline{s}(x)] + \frac{1}{2}\,x\,[\delta\overline{d}(x)-\delta\overline{u}(x)]\ . \end{aligned} \tag{99}$$

In the last line, it is assumed that $\beta = \beta'$ and $\delta q^v = \delta q - \delta\overline{q} \approx 0$. The assumption $\delta q^v \approx 0$ means that charge symmetry violation should manifest itself most strongly in the sea. Fig. 13 show the magnitude of the effect obtained for the two extremes $s(x) = \overline{s}(x)$ and $\overline{s}(x) = 0$ [21]. The result is surprisingly

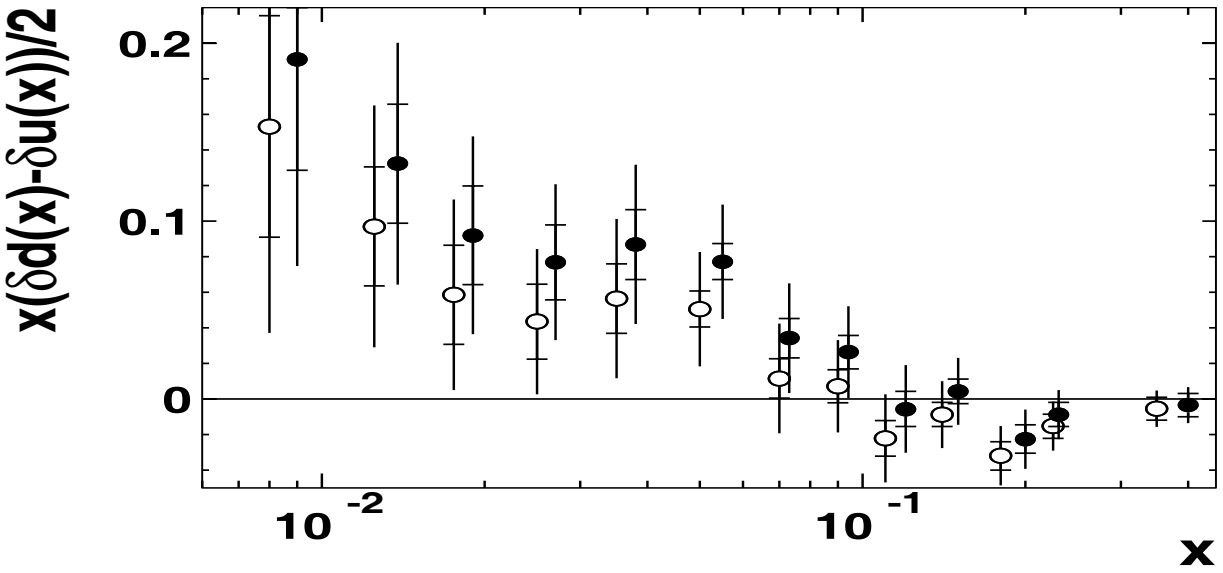

Fig. 13. Degree of charge symmetry violation obtained from Eq. (99) assuming that $s(x) = \overline{s}(x)$ (open circles) and $\overline{s}(x) = 0$ (filled circles). Statistical and systematic errors have been added in quadrature. Reproduced from Ref. [21]. Copyright 1998 by the American Physical Society.

large. Theoretically, $\delta\overline{d}(x) \approx -\delta\overline{u}(x)$ [91] which has the effect that $\overline{u}_p + \overline{d}_p = \overline{u}_n + \overline{d}_n$. The results of Fig. 13 suggest a charge symmetry violation of $\approx 25\%$ at low x. Such large effects, if they exist, would necessarily have to be incorporated into future fits of parton distribution functions.

This rather large charge symmetry violation at low x would be mixed with flavor asymmetry in the DIS and Drell-Yan studies of the Gottfried sum rule violation. In this case, with $-\delta\overline{u} \approx \delta\overline{d}$, Eq. (44) would be rewritten as

$$\frac{1}{x}\left(F_2^{\gamma p}(x) - F_2^{\gamma n}(x)\right) = \frac{1}{3}\left[u^v(x) - d^v(x)\right] + \frac{2}{3}\left[\overline{u}(x) - \overline{d}(x) + \delta\overline{d}\right] . \tag{100}$$

Since measurements of I_G suggest that the second term on the right hand side of Eq. (100) is negative and $\delta\overline{d}$ is positive in Fig. 13, charge symmetry violation would still require a large SU(2) flavor asymmetry, even larger than that suggested without charge symmetry violation. Note that the magnitude of I_G

would not change, only the interpretation of the result if charge symmetry violation mixes with flavor asymmetry [92]. The $\overline{d}/\overline{u}$ ratio with and without charge symmetry violating effects is shown in Fig. 14. The open points show how the flavor asymmetry would need to be enhanced for I_G to remain the same after charge symmetry violation is accounted for. This would indeed require a substantial modification of the low x $\overline{d}$ and $\overline{u}$ distributions in the global analyses of parton distribution functions.

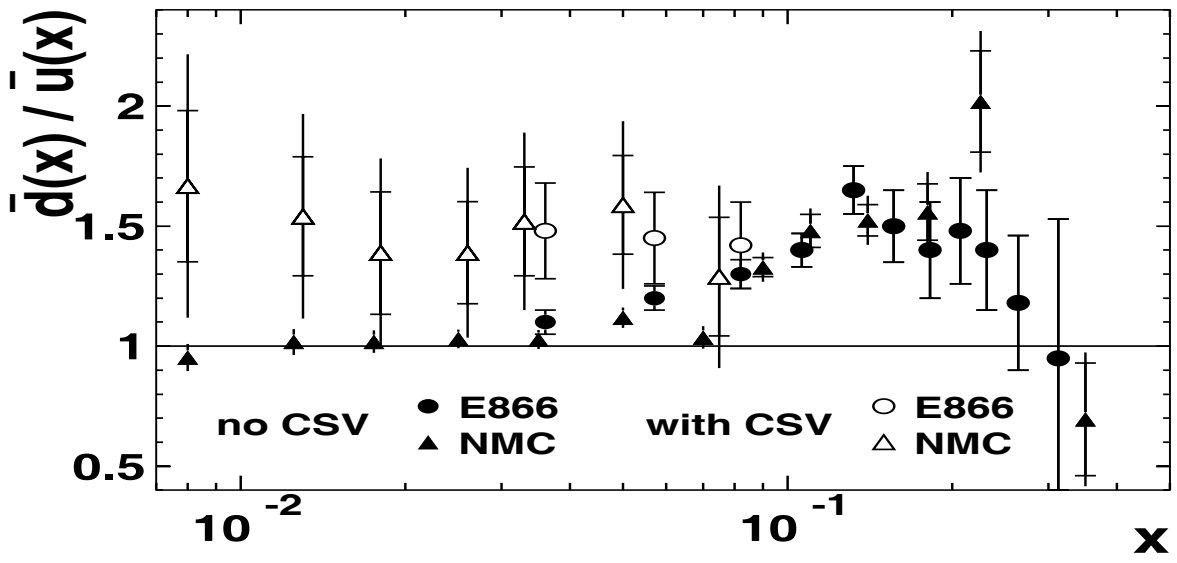

Fig. 14. The ratio $\overline{d}/\overline{u}$ as a function of x for the NMC [39] (triangles) and E866 [41] (circles) data. The solid points do not assume any charge symmetry violation while the open points include charge symmetry violation at low x as parameterized in Fig. 13. Reproduced from Ref. [92]. Copyright 1999 by the American Physical Society.

Another test of charge symmetry violation can be made with $W^{\pm}$ production at hadron colliders. Boros *et al.* [92] suggest comparing W^+ and W^- production in pD collisions at the Relativistic Heavy Ion Collider [93] at Brookhaven National Laboratory, BNL, and the Large Hadron Collider [94] at CERN. However, as recently pointed out by Bodek *et al.* [95], the DIS and Drell-Yan measurements discussed here cannot extract charge symmetry violating effects alone. Measurements of d_p/u_p or d_n/u_n would isolate these effects more definitively. At the Fermilab Tevatron, W^+ and W^- are produced by $u\overline{d} \to W^+$ and $d\overline{u} \to W^-$ respectively. The u quarks carry more of the proton momentum than the d quarks, see Figs. 4-6, so that the W^+ follows the incoming proton while the W^- follows the anti-proton, creating a charge asymmetry between the two in rapidity. This asymmetry, measured through the decay leptons,

is directly sensitive to the d_p/u_p ratio [95]. Bodek *et al.* parameterized the charge symmetry violation of Fig. 13 in two different ways. In the first, the average of the $\overline{d}$ and $\overline{u}$ distributions is unchanged by charge symmetry violation while in the second, the entire violation is placed on the $\overline{d}$, leading to a shift in the total sea quark distribution. Both parameterizations are compared to the Tevatron CDF data at 1.8 TeV [96] in Fig. 15. The large charge symmetry violation suggested in Refs. [21,92] overpredicts the asymmetry for $y > 0$ while calculations with parton distribution functions assuming no charge symmetry violation agree with the data. Bodek *et al.* proposed that even though there is no evidence for charge symmetry violation in the CDF data, the large violation proposed by Boros *et al.* [21,92] can be preserved if charge symmetry is violated only in the neutron parton distributions. In this case, the neutron sea would be larger than the proton sea. Thus, while the results of Ref. [95] weaken the case for charge symmetry violation, they cannot eliminate it until better measurements can be made. Note however that the treatment of $F_3^{W^\pm N}$ by Boros *et al.* [21,92] is at leading order [95]. A treatment beyond leading order might eliminate the need for charge and flavor symmetry violations in the neutron.

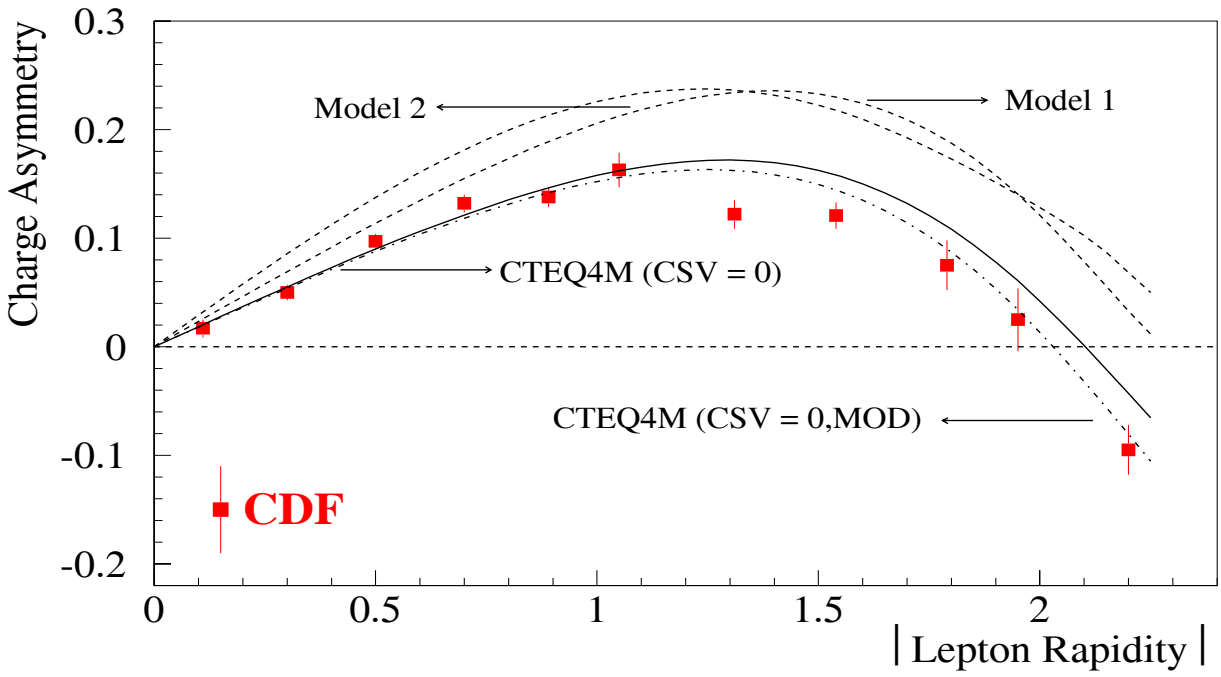

Fig. 15. The CDF $W^\pm$ asymmetry as a function of rapidity [96] compared to calculations without charge symmetry violation, labeled CTEQ4M (CSV=0) and CTEQ4M (CSV=0,MOD), and with the effect of Fig. 13 using the two parameterizations of Bodek *et al.* [95], labeled Model 1 and Model 2. Reproduced from Ref. [95]. Copyright 1999 by the American Physical Society.

3.1.6 Light sea summary

Experiments have clearly shown that not only is $\overline{u} \neq \overline{d}$ but also that the difference is a strong function of x [39,41]. A number of models have been proposed to describe this difference, including meson clouds, Pauli blocking, chiral models, and charge symmetry violation. All but the last assume that $\overline{u} \neq \overline{d}$ is due to SU(2) flavor asymmetry. Meson cloud models have generally had the most success describing the difference $\overline{d} - \overline{u}$ but, with the exception of Ref. [68], generally have not had as much success with the ratio $\overline{d}/\overline{u}$. Chiral models tend to concentrate the difference at low x, underestimating $\overline{d} - \overline{u}$ as a function of x. The proposed charge symmetry violation would also require a large flavor asymmetry [21,92] but relies on the accuracy of the CCFR strange quark measurements [22].

3.2 The strange sea

Possible manifestations of nonperturbative effects in the strange sea are now discussed along with some phenomenological explanations. The CCFR data which might imply a difference between the s and $\overline{s}$ distributions [22] are discussed first. Three experiments which indirectly measure strange form factors, two low-energy elastic ep scattering determinations of the parity-violating asymmetry [97,98] and neutral current ν and a $\overline{\nu}$ scattering experiment on nucleons [99], are also introduced.

3.2.1 Experiments

The CCFR collaboration has performed LO and NLO evaluations of dilepton production in neutrino scattering off nucleons to more directly study the strange quark distributions [20,22]. Although, as mentioned earlier, they found $s(x) = \overline{s}(x)$ within their uncertainties, the result is not inconsistent with $s(x) \neq \overline{s}(x)$ in some x regions, as is now discussed.

Pairs of opposite sign muons can be produced via charm production in ν_μ and $\overline{\nu}_\mu$ scattering off nucleons:

$$\begin{aligned} \nu_\mu \; + \; N \; &\longrightarrow \; \mu^- + c \; + \; X \\ &\hookrightarrow \; \mu^+ \; + \; \nu_\mu \end{aligned} \tag{101}$$

$$\begin{aligned} \overline{\nu}_\mu \; + \; N \; &\longrightarrow \; \mu^+ + \overline{c} \; + \; X \\ &\hookrightarrow \; \mu^- \; + \; \overline{\nu}_\mu \; . \end{aligned} \tag{102}$$

In the first case, the neutrino interacts with an s or d quark, $\nu + s, d \rightarrow c + \mu^-$, to produce a charm quark which then decays semileptonically to a μ^+. Because the d-induced channel is Cabibbo suppressed relative to that of the strange quark, this process can provide a determination of the strange sea. Likewise, the anti-neutrino-induced interaction is an independent measurement of the anti-strange distribution.

The non-strange quark and anti-quark components of the sea were assumed to be symmetric so that $\overline{u}(x) = u_s(x)$ and $\overline{d}(x) = d_s(x)$. An isoscalar correction was also applied assuming $\overline{u}(x) = \overline{d}(x)$. The strange sea was allowed to have a different magnitude and shape than the non-strange sea. Shape parameters were determined from two fits, both starting from the same set of proton parton distributions at initial scale $\mu_0^2 = 1$ GeV^2 [100]. In the first fit, $s(x) = \overline{s}(x)$, while in the second $s(x)$ and $\overline{s}(x)$ were determined independently. The x-integrated strange fraction of the sea is set by the parameter

$$\kappa = \frac{\int_0^1 dx\,[xs(x,\mu^2) + x\overline{s}(x,\mu^2)]}{\int_0^1 dx\,[x\overline{u}(x,\mu^2) + x\overline{d}(x,\mu^2)]}\ , \tag{103}$$

where $\kappa = 1$ indicates an SU(3) flavor symmetric sea. The shape of the strange quark distribution is related to that of the non-strange sea by a shape parameter δ. If $\delta = 0$, the strange sea would have the same x dependence as the non-strange sea.

Assuming that $s(x) = \overline{s}(x)$, the sea quark distributions were parameterized as

$$xs(x,\mu^2) = A_s(1-x)^\delta \left[\frac{x\overline{u}(x,\mu^2) + x\overline{d}(x,\mu^2)}{2}\right] \tag{104}$$

$$x\overline{q}(x,\mu^2) = (2 + A_s(1-x)^\delta) \left[\frac{x\overline{u}(x,\mu^2) + x\overline{d}(x,\mu^2)}{2}\right]\ . \tag{105}$$

The normalization A_s in Eq. (104) is defined in terms of κ and δ. With the requirement $s(x) = \overline{s}(x)$, the parameters are

$$\kappa = 0.477\ ^{+\ 0.051}_{-\ 0.050}\ ^{-\ 0.017}_{+\ 0.036} \tag{106}$$

$$\delta = -0.02\ ^{+\ 0.66}_{-\ 0.60}\ ^{+\ 0.08}_{-\ 0.20} \tag{107}$$

$$m_c = 1.70 \pm 0.19 \pm 0.02\ \text{GeV}\,. \tag{108}$$

Note that the charm quark mass enters the fit through the original charm production reaction in Eqs. (101) and (102).

The strange quark, Eq. (104), and the total anti-quark, Eq. (105), $x\overline{q} = x\overline{u} + x\overline{d} + x\overline{s}$, distributions in this fit are shown in Fig. 16 at the initial scale $\mu_0^2 = 1$ GeV^2. The strange quark distribution is scaled up by a factor of 2.5 in Fig. 16(a) to show its similarity to the anti-quark distribution. Since $\delta \neq 0$ would indicate a shape difference between $x\overline{q}(x)$ and $xs(x)$, the fit value $\delta = -0.02\ ^{+\ 0.66}_{-\ 0.60}$ indicates no shape difference at NLO. In a previous leading order fit, they found that the strange quark distribution was softer than the total quark sea by $(1-x)^{2.5\pm0.7}$. The difference between the LO and NLO fits may be attributable to a softer $x\overline{q}(x)$ at NLO than LO. This similarity is highlighted in Fig. 16(b) where the ratio of the strange quark distribution to $x\overline{q}$ is shown. The ratio is essentially constant over all x.

If one allows the momentum distributions of the s and $\overline{s}$ quarks to be different, the sea quark distribu-

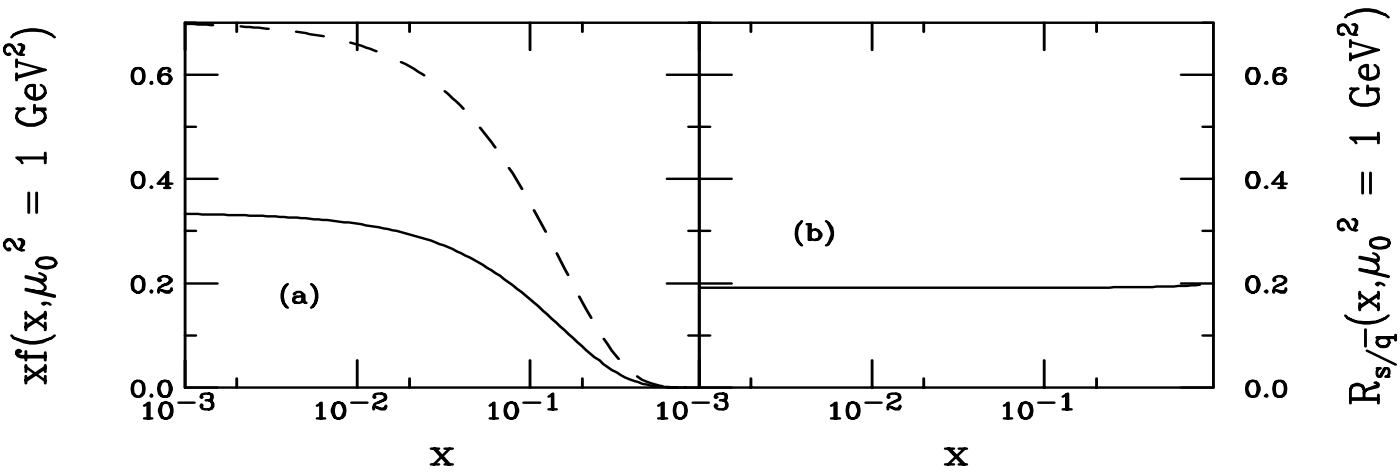

Fig. 16. The CCFR $x\overline{q}$ and xs distributions in the $s(x) = \overline{s}(x)$ fit are compared at the initial scale 1 GeV^2. In (a) the individual distributions are shown with the strange quark distribution (solid curve) multiplied by a factor of 2.5. In (b), the ratio $xs/x\overline{q}$ is shown.

tions can be parameterized by:

$$xs(x,\mu^2) = A_s(1-x)^{\delta}\left[\frac{x\overline{u}(x,\mu^2)+x\overline{d}(x,\mu^2)}{2}\right] \tag{109}$$

$$x\overline{s}(x,\mu^2) = A'_s(1-x)^{\delta-\Delta\delta}\left[\frac{x\overline{u}(x,\mu^2)+x\overline{d}(x,\mu^2)}{2}\right] \tag{110}$$

$$\begin{aligned} x\overline{q}(x,\mu^2) = (2+\frac{1}{2}(&A_s(1-x)^{\delta} \\ &+ A'_s(1-x)^{\delta-\Delta\delta}))\left[\frac{x\overline{u}(x,\mu^2)+x\overline{d}(x,\mu^2)}{2}\right] . \end{aligned} \tag{111}$$

The fit required the number of s and $\overline{s}$ quarks to be equal:

$$\int_0^1 dx\, s(x,\mu^2) = \int_0^1 dx\, \overline{s}(x,\mu^2) \ . \tag{112}$$

The normalization factors A_s and A'_s are defined in terms of κ, δ and $\Delta\delta$. In this case they found

$$\kappa = 0.536 \pm 0.030 \pm 0.036\ ^{-\ 0.064}_{+\ 0.098} \pm 0.009 \tag{113}$$

$$\delta = -0.78 \pm 0.40 \pm 0.56 \pm 0.98 \pm 0.50 \tag{114}$$

$$\Delta\delta = -0.46 \pm 0.42 \pm 0.36 \pm 0.65 \pm 0.17 \tag{115}$$

$$m_c = 1.66 \pm 0.16 \pm 0.07\ ^{+\ 0.04}_{-\ 0.01} \pm 0.01 \text{ GeV} \ . \tag{116}$$

In this analysis, the total strange quark content, given by κ, is slightly higher and the shape of the

s quark distribution is different from the non-strange sea. Compare Eqs. (113) and (114) with the values of κ and δ in Eqs. (106) and (107). The charm quark mass parameters in the two fits are very similar. The uncertainty in $\Delta\delta$ is large enough for the s and $\overline{s}$ momentum distributions to be consistent with a difference limited to $-1.9 < \Delta\delta < 1.0$ at the 90% confidence level. The resulting $s(x)$ and $\overline{s}(x)$ distributions in Eqs. (109) and (110) are compared to the $\overline{q}$ distribution, Eq. (111), in Fig. 17 at the initial scale $\mu_0^2 = 1$ GeV^2. Both the s and $\overline{s}$ distributions are multiplied by a factor of 2.5 to facilitate comparison with the larger $\overline{q}$ distribution. The strange quark distribution is larger than the anti-strange distribution and deviates more from the total anti-quark distribution than does the anti-strange distribution.

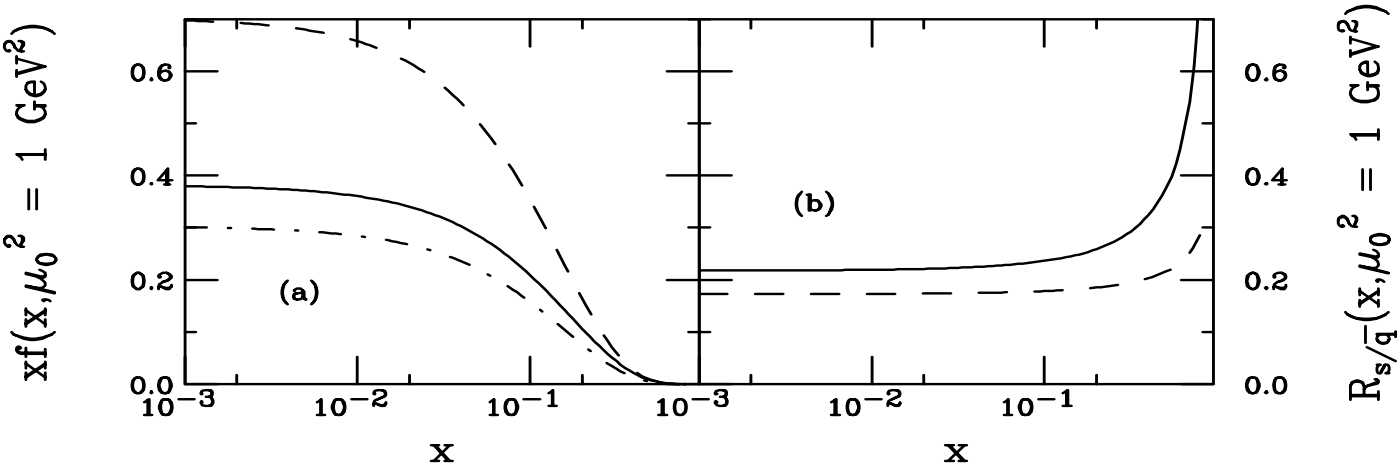

Fig. 17. The CCFR $x\overline{q}$, xs, and $x\overline{s}$ distributions in the $s(x) \neq \overline{s}(x)$ fit are compared at the initial scale 1 GeV^2. In (a) the individual distributions are shown with the strange quark (solid curve) and anti-strange quark (dot-dashed curve) multiplied by a factor of 2.5. In (b), the ratios $xs/x\overline{q}$ (solid curve) and $x\overline{s}/x\overline{q}$ (dashed curve) are shown.

It is important to note that the starting distributions [100] used in the fits assume flat sea and gluon distributions as $x \to 0$ and a flavor symmetric light quark sea. Both these assumptions have had to be modified recently. If the analysis was repeated with newer starting distributions which take these new developments into account, perhaps the results would change. In particular, the discrepancy between these data and the muon-induced DIS data which led Boros *et al.* to argue for a large charge symmetry violation [21] could be reduced and the difference, if any, between $s(x)$ and $\overline{s}(x)$ could be more clearly delineated.

A step in this direction was recently taken by Barone *et al.* [101] in an analysis of DIS data that emphasized the ν and $\overline{\nu}$ induced cross section data. The CCFR data were not used in their global fit but the fitted strange quark distribution was shown to agree with their data. Barone *et al.* also allowed $s(x) \neq \overline{s}(x)$ in one of their fits to all DIS data but did not constrain the shapes to be proportional to $0.5[\overline{u}(x)+\overline{d}(x)]$ as in Eqs. (109) and (110). Since the DIS data included in the Barone *et al.* fit was more

balanced between ν and $\overline{\nu}$ induced events with better statistics, tighter constraints on the difference between $s(x)$ and $\overline{s}(x)$ were set. They note that the assumption $s(x) \neq \overline{s}(x)$ gave a better overall fit to the data with $xs(x)$ harder than $x\overline{s}(x)$. The difference is largest at $x > 0.4$, as seen in Fig. 18 [101].

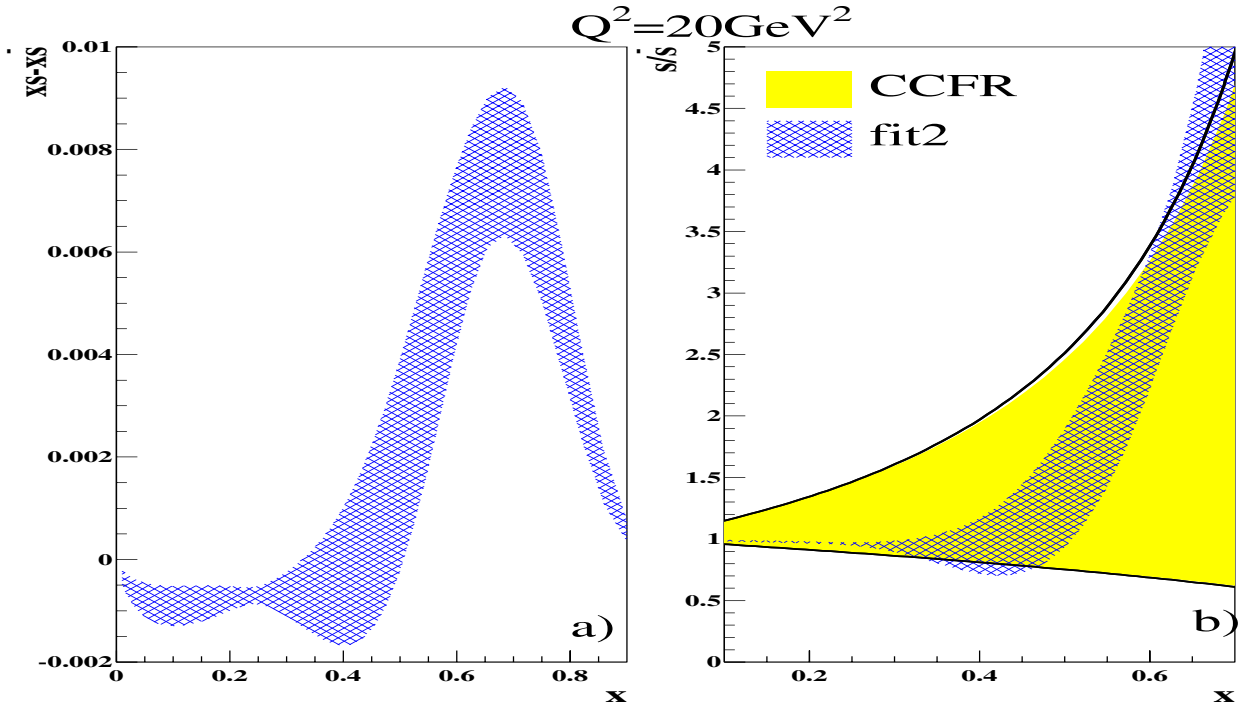

Fig. 18. Results of a fit to all DIS data allowing $s(x) \neq \overline{s}(x)$ [101]. The results for the difference $xs(x) - x\overline{s}(x)$ is shown in (a) while the ratio $s(x)/\overline{s}(x)$ of the fit is compared to the CCFR result at $Q^2 = 20$ GeV^2 in (b). Reproduced from Ref. [101] with permission from Springer-Verlag.

Strange form factors have been inferred from the parity violating asymmetry in electron-proton elastic scattering

$$A = \frac{\sigma_R - \sigma_L}{\sigma_R + \sigma_L} = \frac{-G_F Q^2}{\pi\alpha\sqrt{2}} \frac{\epsilon G_E^\gamma G_E^Z + \tau G_M^\gamma G_M^Z - 0.5(1 - 4\sin^2\theta_W)\epsilon' G_M^\gamma F_A^Z}{\epsilon (G_E^\gamma)^2 + \tau (G_M^\gamma)^2} , \quad (117)$$

where $\tau = Q^2/4m^2$, $\epsilon = 1/(1 + 2(1+\tau)\tan^2(\theta/2))$, $\epsilon' = \sqrt{\tau(1+\tau)(1-\epsilon^2)}$, and θ is the scattering angle. This asymmetry between right and left handed incident electrons is due to the interference of the electromagnetic and neutral weak amplitudes. The electromagnetic electric and magnetic form factors

are G_E^γ and G_M^γ while the neutral weak electric, magnetic, and axial form factors are G_E^Z, G_M^Z and F_A^Z. To leading order, the proton weak magnetic form factor is

$$G_M^Z = \frac{1}{4}\left[G_M^{\gamma p}(1 - 4\sin^2\theta_W) - G_M^{\gamma n} - G_M^s\right] \ . \tag{118}$$

The electroweak radiative corrections to Eq. (118) have been calculated [102]. The weak mixing angle θ_W has been determined with high precision and $G_M^{\gamma p}$ and $G_M^{\gamma n}$ are known.

The strange magnetic form factor has been determined by the SAMPLE collaboration [97] at backward angles. A 200 MeV polarized electron beam is directed on a liquid hydrogen target. The polarized electron source is a GaAs photoemission crystal. The photoemission is stimulated by a laser beam incident on the crystal. The laser beam is circularly polarized and the electron beam helicity is reversed by changing the voltage to the cell which polarizes the laser beam, reversing the circular polarization of the light. The helicity is chosen at random for ten consecutive pulses and the complement helicities are used for the next ten pulses. The scattered electrons are detected by a large Cerenkov detector which accepts momentum transfers of $Q^2 \sim 0.1$ GeV^2. The asymmetry is found for pairs of pulses separated by 1/60 s to minimize systematic uncertainties. Each "pulse pair" asymmetry is equivalent to a measurement of the parity violating asymmetry, Eq. (117).

The SAMPLE collaboration determined G_M^Z from A. The strange magnetic form factor G_M^s can be obtained from A since the backward scattering angles and low Q^2 cause the second term in the numerator of Eq. (117) to dominate the asymmetry. They found

$$A = -6.34 \pm 1.45 \pm 0.53 \text{ ppm} \ , \tag{119}$$

$$G_M^Z = 0.34 \pm 0.09 \pm 0.04 \pm 0.05 \text{ n.m.} \tag{120}$$

at $Q^2 = 0.1$ GeV^2. The last uncertainty on G_M^Z is due to theoretical uncertainties in the form factors. If $G_M^s = 0$, then $G_M^Z = 0.40$ n.m. [97]. Thus the difference between the expected and the measured G_M^Z corresponds to [97]

$$G_M^s(Q^2 = 0.1\,\text{GeV}^2) = 0.23 \pm 0.37 \pm 0.15 \pm 0.19 \text{ n.m.} \ , \tag{121}$$

consistent with zero.

The HAPPEX collaboration performed a similar measurement of A at a higher energy, with 3.356 GeV electrons, and the scattered electrons were measured at more forward angles $\langle\theta_{\text{lab}}\rangle \sim \pm 12.3^\circ$ [98]. The polarized source was a GaAs photocathode excited by a circularly polarized laser. The helicity was set every 33.3 ms and structured as pairs of consecutive 33.3 ms periods of opposite helicity. The presence of false asymmetry was ruled out by inserting a half-wave plate in the laser beam. The correlation between the half-wave plate and the sign of the asymmetry was an unambiguous signal of parity violation. The measured asymmetry was

$$A = -14.5 \pm 2.0 \pm 1.1\,\text{ppm} \tag{122}$$

at $Q^2 = 0.48$ GeV^2. Since τ and ϵ are of the same order at forward angles, G_E^s and G_M^s cannot be separated from each other. Thus the combination of the strange electric and magnetic form factors was reported [98]

$$G_E^s + \frac{\tau}{\epsilon}\frac{G_M^\gamma}{G_E^\gamma}G_M^s = 0.023 \pm 0.034 \pm 0.022 \pm 0.026(\delta G_E^{\gamma n})\,\text{n.m.}\,. \tag{123}$$

The last uncertainty is an estimate of the theoretical uncertainty on $G_E^{\gamma n}$. A new run should improve the precision of Eq. (123) by a factor of two [103].

Both the SAMPLE and HAPPEX results are consistent with strong suppression of the strange sea at low energies [104]. To separate G_E^s from G_M^s at fixed Q^2, a number of scattering angles and thus beam energies are needed [103]. An isoscalar target would also help separate G_E^s and G_M^s [98]. Additional measurements of weak currents and strange form factors are planned at Mainz [105] and the Thomas Jefferson Nation Accelerator Facility, TJNAF [106].

Information about the strange form factors of the nucleon can also be obtained from scattering of ν and $\overline{\nu}$ on nucleons. The BNL experiment E734 [99] performed such an investigation using wideband neutrino and anti-neutrino beams on a ^{12}C target with an average energy of 1.3 GeV and momentum transfer $0.5 < Q^2 < 1$ GeV^2. The majority, 80%, of the data were due to quasielastic proton knockout from the carbon nuclei, $\nu n \to \mu^- p$ and $\overline{\nu} p \to \mu^+ n$, charged current processes, and the remaining 20% arose from ν and $\overline{\nu}$ elastic scattering on free protons, $\nu p \to \nu p$ and $\overline{\nu} p \to \overline{\nu} p$, governed by neutral current interactions. Since the quasielastic interactions do not involve strange quarks, the strange form factors only appear in neutral current processes.

Experimental differential cross sections are obtained by a convolution of the expected differential distribution with the neutrino/anti-neutrino energy spectrum, $\phi_\nu(\epsilon_\nu)$, so that

$$\langle\frac{d\sigma_\nu}{dQ^2}\rangle = \frac{1}{\Phi_\nu}\int_{\epsilon_{\min}}^{\epsilon_{\max}} d\epsilon_\nu \frac{d\sigma_\nu}{dQ^2}\phi_\nu(\epsilon_\nu) \tag{124}$$

where $\epsilon_{\min} = 0.2$ GeV and $\epsilon_{\max} = 5$ GeV. In Eq. (124), ν represents either neutrinos or anti-neutrinos. The total neutrino flux is Φ_ν. In the elastic scattering events, Q^2 is directly obtained from the kinetic energy of the scattered proton, T_p, in the laboratory frame, $Q^2 = 2m_p T_p$. In the quasielastic knockout events, an effective momentum transfer for ν and $\overline{\nu}$ scattering off free nucleons was obtained by correcting for the binding energy and Fermi motion of the struck nucleon. The total cross sections, $\langle\sigma_\nu\rangle$, were obtained by integrating Eq. (124) over Q^2 in the range of the data. The cross section ratios were [99]:

$$R = \frac{\langle \sigma_{\overline{\nu}p \to \overline{\nu}p} \rangle}{\langle \sigma_{\nu p \to \nu p} \rangle} = 0.302 \pm 0.019 \pm 0.037 \tag{125}$$

$$R_\nu = \frac{\langle \sigma_{\nu p \to \nu p} \rangle}{\langle \sigma_{\nu n \to \mu^- p} \rangle} = 0.153 \pm 0.007 \pm 0.017 \tag{126}$$

$$R_{\overline{\nu}} = \frac{\langle \sigma_{\overline{\nu}p \to \overline{\nu}p} \rangle}{\langle \sigma_{\overline{\nu}p \to \mu^+ n} \rangle} = 0.218 \pm 0.012 \pm 0.023 \tag{127}$$

where R is the elastic $\overline{\nu}/\nu$ scattering ratio while R_ν and $R_{\overline{\nu}}$ are the ratios of elastic scattering to quasielastic knockout cross sections after the correction to "free scattering". Thus R_ν and $R_{\overline{\nu}}$ are ratios of charged to neutral current processes while R involves only neutral current scattering.

In the following sections, models of the interactions discussed here are introduced and compared to the data.

3.2.2 $s/\overline{s}$ asymmetry

The CCFR NLO evaluation of the strange quark distributions did not exclude the possibility that the strange and anti-strange quark distributions are different. The analysis indicated that this asymmetry is small, on the order of $(1-x)^{-0.46}$ [22], as suggested by Eqs. (109), (110), and (115). There is actually no reason why the sea quark and anti-quark distributions must be the same besides phenomenological prejudices as long as their total numbers are identical. Nothing in the QCD Lagrangian explicitly relates the sea quark and anti-quark distributions in the nucleon. Charge conjugation symmetry only tells us that the quark distribution in a proton is the same as the anti-quark distribution in an anti-proton [107].

Ji and Tang showed that for every sea quark interaction, the corresponding sea anti-quark interaction may be obtained by changing the direction of quark propagation in the Feynman diagram [107]. However, different color factors are associated with the quark line direction, changing the relative interaction strengths. They found that while the quark and anti-quark diagrams are of the same order in $1/N_c$ (N_c is the number of colors) the numerical coefficients are not constrained to be identical.

A difference between the strange and anti-strange quark distributions can arise naturally in the meson cloud-type models introduced in Section 3.1.2. Since the proton can fluctuate into a virtual kaon-hyperon intermediate state, the strange anti-quark distribution in the kaon is different from the strange quark distribution in the hyperon [108]. The results of meson cloud model calculations [109–112] will be discussed in this section followed by a calculation of the strange and anti-strange distributions based on the locality of the strange sea [107].

The first model, by Paiva *et al.* [109], follows directly from the one outlined in Eqs. (65)-(71). If the kaon is assumed to be the intermediate meson state and the Λ, Σ, and Σ^* are the intermediate hyperon

states, the strange anti-quark distribution in the nucleon is

$$x\overline{s}_N(x,Q^2) = \sum_Y \tau_Y \int_x^1 dy\, f_{KY}(y)\, \frac{x}{y}\, \overline{s}_K^v(\frac{x}{y},Q^2)\ . \tag{128}$$

following Eq. (71) where τ_Y are the kaon-hyperon spin-flavor SU(6) Clebsch-Gordon coefficients. The kaon distribution in the nucleon cloud, $f_{KY}(y)$, is calculated as in Eq. (66) with $M \to K$ and $B \to Y$. An exponential form factor, Eq. (70), was used with $\Lambda_e = 1.2$ GeV, corresponding to $\Lambda_m = 0.94$ GeV. The strange valence quark distribution in the kaon was assumed to be identical to the pion valence quark distributions. In Ref. [109] the SMRS [113] pion structure function was used to obtain $x\overline{s}_K^v(x,Q^2)$. Paiva *et al.* refer to the distribution in Eq. (128) as the intrinsic anti-strange quark distribution, after the intrinsic charm model of Brodsky *et al.* [114]. Their intrinsic distribution is compared to the CCFR data and another meson-cloud model calculation [62] based on the GRV pion distribution functions [72] in Fig. 19. The shape of the intrinsic distribution is valence-like, as expected in such models [114].

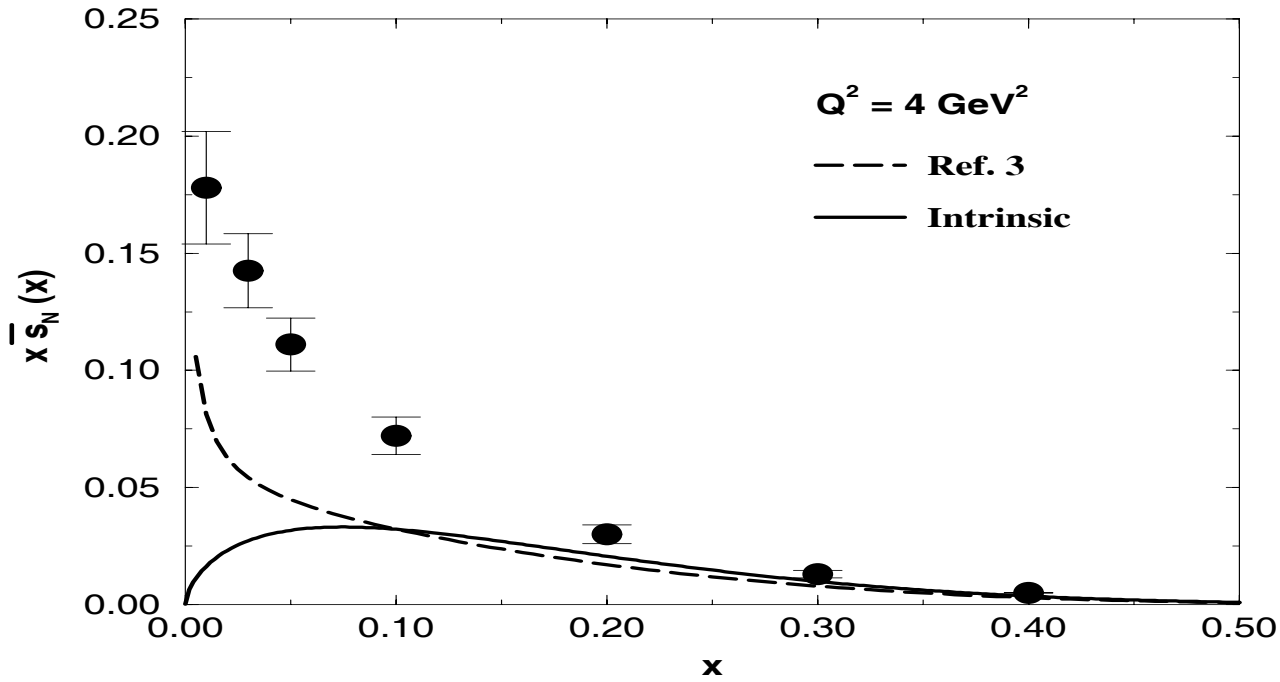

Fig. 19. The intrinsic $x\overline{s}_N$ distribution calculated with the meson cloud model (solid curve). The result is compared to the CCFR [22] data and the model calculation of [62] (dashed curve), labeled Ref. 3 on the figure. Reproduced from Ref. [109] with permission from World Scientific.

The GRV pion-based result, labeled Ref. 3 on Fig. 19, has the opposite behavior at low x. While both calculations agree with the CCFR data for $x > 0.3$, neither can describe the low x behavior of the data.

Christiansen and Magnin [110] developed their approach in the context of the valon model [70], described in Section 3.1.2. In this case, the gluon emitted by the valon can decay into an $s\overline{s}$ pair. This three valon + $s\overline{s}$ state can then rearrange itself to form a kaon-hyperon bound state. They point out that the strange meson and baryon distributions inside the nucleon are not independent but are constrained by the requirements of zero strangeness in the nucleon and momentum conservation of the meson-baryon state,

$$\int_0^1 dx\,[P_B(x) - P_M(x)] = 0 \tag{129}$$

$$\int_0^1 dx\,[xP_B(x) + xP_M(x)] = 1\ . \tag{130}$$

Both conditions are satisfied if $P_M(x) = P_B(1-x)$ where $P_M(x)$ is the strange meson distribution in the proton, corresponding to f_{KY} in Eq. (128). Note that in this model, no explicit form factor is required since the valon model is defined on the light cone. Thus, the conditions in Eqs. (129) and (130) can be satisfied.

They use the recombination model [73] in Eq. (79) with $a = 1$ in Eq. (78) to predict the rearrangement of the valons and the strange partons in the proton so that

$$P_M(x) = \int_0^x \frac{dy}{y} \int_0^{x-y} \frac{dz}{z} F(y,z) R(x,y,z)\ . \tag{131}$$

The normalizations of $F(y,z)$ and $R(x,y,z)$ are fixed by assuming the probability of $s\overline{s}$ pair production by a valon is $\sim 4 - 10\%$ [110].

The nonperturbative strange and anti-strange quark densities in the nucleon are

$$s^{\rm NP}(x) = \int_x^1 \frac{dy}{y} P_B(y)\ s_B\left(\frac{x}{y}\right) \tag{132}$$

$$\overline{s}^{\rm NP}(x) = \int_x^1 \frac{dy}{y} P_M(y)\ \overline{s}_M\left(\frac{x}{y}\right)\ . \tag{133}$$

Two different approximations of $s_B(x)$ and $\overline{s}_M(x)$ were tested,

$$\overline{s}_M(x) = 6x(1-x) \qquad s_B(x) = 12x(1-x)^2 \tag{134}$$

$$\overline{s}_M(x) = q^\pi(x)(1-x)^{0.18} \qquad s_B(x) = \frac{1}{2} u_p^v(x)\ . \tag{135}$$

The strange and anti-strange densities in the proton, Eqs. (132) and (133), are shown in Fig. 20 along with the difference $s^{\rm NP}(x) - \overline{s}^{\rm NP}(x)$. Although they do not compare the calculations directly to data, it is clear that the kaon and hyperon distributions in Eq. (135) agree better with the trends of the CCFR data since the differences between the s and $\overline{s}$ distributions are small except at low x where the valon model is expected to break down. An "intrinsic"-type meson cloud model calculation was performed

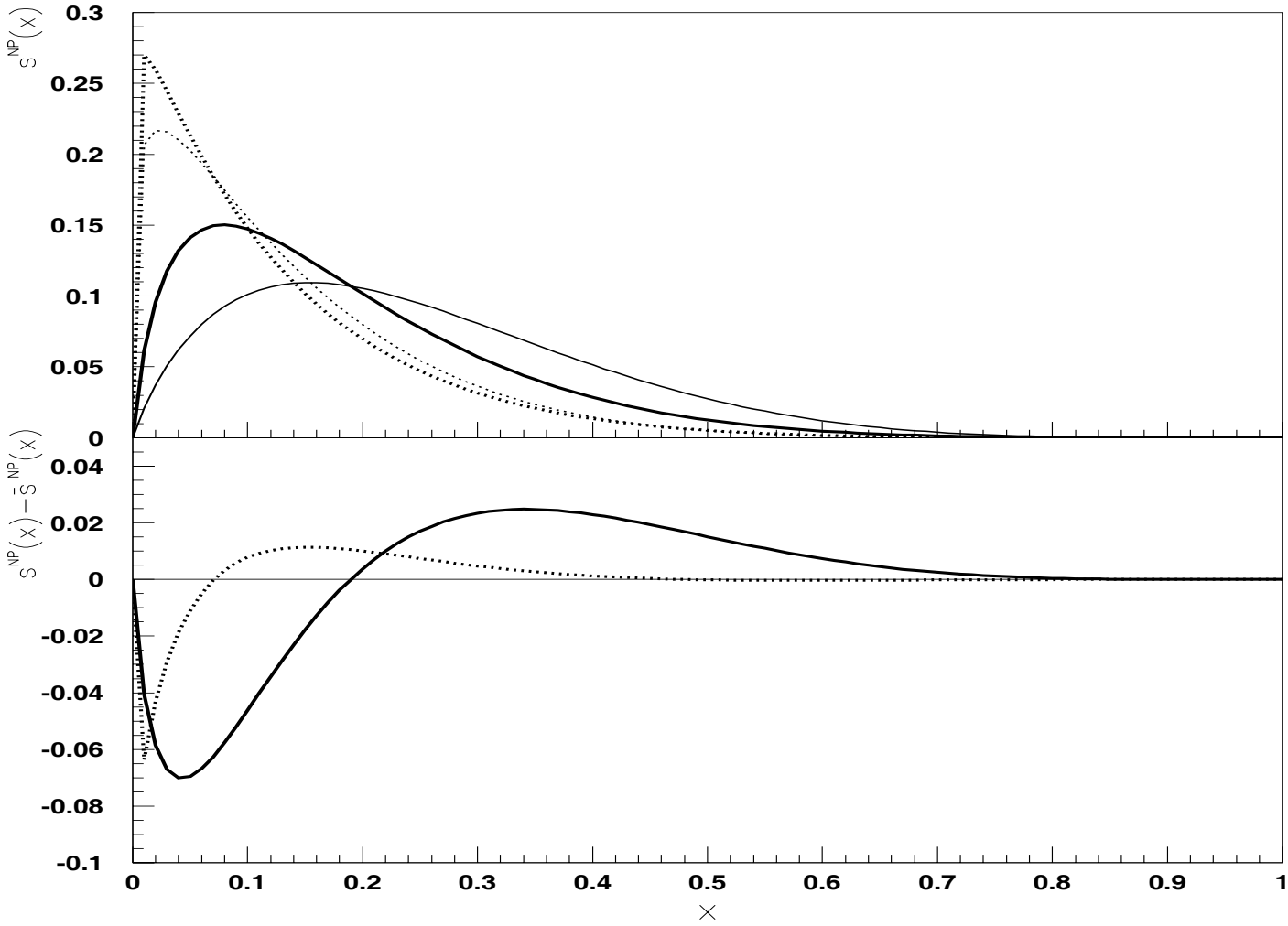

Fig. 20. The upper plot shows the nonperturbative strange (thin lines) and anti-strange (thick lines) distributions in the nucleon. The solid curves are calculated assuming the schematic kaon and hyperon distributions of Eq. (134) while the dotted curves are calculated with Eq. (135). The lower plot gives the difference $s^{\rm NP}(x) - \overline{s}^{\rm NP}(x)$ obtained with Eq. (134) (solid curve) and Eq. (135) (dotted curve). Reproduced from Ref. [110] with permission from Elsevier Science.

by Brodsky and Ma [111] with results similar to those shown in the solid curve in Fig. 20. A light-cone calculation of $s(x) - \overline{s}(x)$ by Melnitchouk and Malheiro shows the opposite behavior: $s(x) - \overline{s}(x)$ is positive at low x and negative at large x [112].

Ji and Tang discussed the implications of the CCFR data on the "locality" of the strange sea [107]. They define two limits on the locality. If the s and $\overline{s}$ are bound in pairs or if they move independently of each other but have similar interactions with other partons, the s and $\overline{s}$ have essentially the same spatial and momentum wavefunctions. This limit corresponds to small locality. If, instead, the quarks and anti-quarks move independently of each other with different interactions with other partons, their distributions should be different, corresponding to large locality. The locality in coordinate space, the strangeness radius, is

$$\langle r_s^2 \rangle = \int d\vec{r}\, r^2 \left(|s(\vec{r})|^2 - |\overline{s}(\vec{r})|^2 \right) . \tag{136}$$

The corresponding locality in momentum space is [107]

$$L_s = \int_0^1 dx\, |s(x) - \overline{s}(x)| . \tag{137}$$

A small L_s or $\langle r_s^2 \rangle$ is equivalent to a large locality while a large L_s or $\langle r_s^2 \rangle$ represents a small locality.

They concluded that the standard meson cloud picture of the s and $\overline{s}$ distributions, as in Eq. (128) [62,109], predicts a larger locality than the CCFR data can accommodate, see Fig. 20. They attempted to model the s and $\overline{s}$ distributions in a manner that could correlate coordinate and momentum space localities. One obvious way of doing this is to assume that $g \to s\overline{s}$ is the dominant $s\overline{s}$ production mechanism at scale $\mu^2 = 1$ GeV^2. This perturbative production is regulated by introducing effective s and $\overline{s}$ masses which could arise from mean-field interactions between the s and $\overline{s}$ with other components of the sea. They allow $m_s \neq m_{\overline{s}}$ to account for differences between the s and $\overline{s}$ interactions in the nucleon. The larger the effective mass, the harder the momentum distributions. They calculate the strange quark distribution in the gluon by [107]

$$\begin{aligned} f_s(x,\mu^2) = \frac{\alpha_s}{4\pi} \int_0^{\mu^2} dk_\perp^2 [(k_\perp^2 + m_{\overline{s}}^2) + (1-x)(m_s^2 - m_{\overline{s}}^2)]^{-2} \{ & 2x(1-x) m_s m_{\overline{s}} \\ & + (k_\perp^2 + m_{\overline{s}}^2)[x^2 + (x-1)^2] + (1-x)^2 (m_s^2 - m_{\overline{s}}^2) \Big\} \end{aligned} \tag{138}$$

where $\alpha_s = 0.5$ and $f_{\overline{s}}(x,\mu^2) = f_s(1-x,\mu^2)$.

The strange quark distribution in the nucleon is obtained by convoluting $f_s(x,\mu^2)$ with the nucleon gluon distribution,

$$xs(x, m_s, m_{\overline{s}}) = \int_x^1 \frac{dy}{y}\, x f_s(\frac{x}{y}, m_s, m_{\overline{s}})\, G(y, \mu^2 = 1\,\mathrm{GeV}^2) . \tag{139}$$

They fit Eq. (139) and the corresponding anti-strange distribution to the CCFR s and $\overline{s}$ results by adjusting m_s and $m_{\overline{s}}$. With the CTEQ3 gluon distribution [115], they found $m_s = 260 \pm 70$ MeV and $\overline{m}_s = 220 \pm 70$ MeV. Note that the lower limit of $m_{\overline{s}}$ is correlated with the upper limit of m_s. Within the range of uncertainties, the effective masses are equivalent and the agreement with the data is good, as seen in Fig. 21.

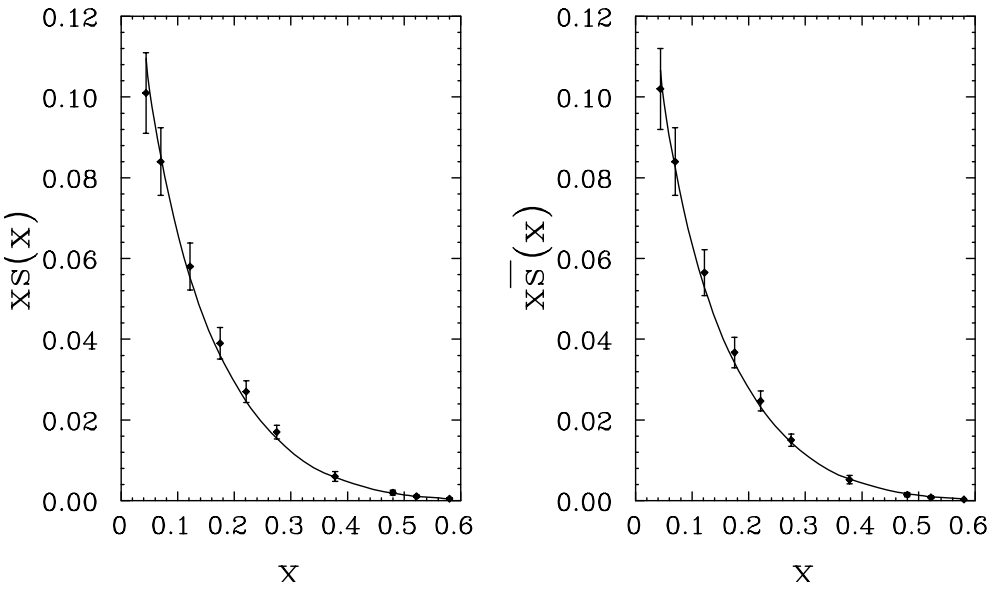

Fig. 21. Comparison of the strange and anti-strange quark distributions calculated with Eq. (139) with the CCFR data [22]. The effective masses $m_s = 260$ MeV and $m_{\overline{s}} = 220$ MeV are used. Reproduced from Ref. [107] with permission from Elsevier Science.

Comparing the meson-cloud type models of Figs. 19 and 20 with the gluon splitting picture of Fig. 21, it appears that the s and $\overline{s}$ distributions are more strongly correlated than allowed by the meson cloud model unless rather hard valence distributions are assumed for the valence quark distributions in the strange mesons and baryons, such as in the dotted curves of Fig. 20. The data thus seem to imply that the s and $\overline{s}$ quarks undergo similar interactions and their distributions have a high degree of locality.

The rather significant correlation between the s and $\overline{s}$ distributions suggests that the strangeness radius, Eq. (136), is small. The strangeness radius can be extracted by measuring the strange quark contribution to the nucleon elastic form factor, as done by SAMPLE [97]. Both Paiva *et al.* [109] and Ji and Tang [107] provided estimates of the strangeness radius within their models.

In the intrinsic strangeness calculation of Paiva *et al.* the integral over $\overline{s}_N$ is equivalent to the probability of finding an intrinsic $s\overline{s}$ pair in the proton wavefunction. They obtain $P_{\rm IS} = \int dx\, \overline{s}_N(x) = 0.12$. The

probability is related to the strangeness radius by

$$P_{\rm IS} = \frac{|\langle r_s^2 \rangle|}{|\langle r_p^2 \rangle|} \ , \tag{140}$$

where, using $r_p = 0.72$ fm and the integrated value of $P_{\rm IS}$, they find [109]

$$|\langle r_s^2 \rangle| = 0.0622 \text{ fm}^2 \ . \tag{141}$$

They also note that if they only considered $K\Lambda$ components in the cloud, the strangeness radius would be reduced by more than a factor of two. However, they can only predict the absolute value of $|\langle r_s^2 \rangle|$, not its sign.

Ji and Tang translate their small locality in momentum space into a coordinate space locality by dimensional analysis [107]

$$|\langle r_s^2 \rangle| \sim \frac{(m_s - \overline{m}_s)}{\mu^3} \leq 0.005 \text{ fm}^2 \ , \tag{142}$$

considerably smaller than the prediction of Paiva *et al.* [109] as well as other earlier theoretical predictions [104,107] although the result is similar to that of Ref. [112].

3.2.3 Strange form factors

The strange form factors have been studied phenomenologically in the context of the E734 ν and $\overline{\nu}$ scattering experiment [99]. The neutral current cross section is sensitive to the electric, magnetic, and axial strange form factors of the nucleon while the charged current interactions do not access the strange quarks in the nucleon sea at low Q^2.

The neutral current elastic scattering cross sections are [116]

$$\begin{aligned} \frac{d\sigma_{\nu p \to \nu p}}{dQ^2} = \frac{G_F^2}{2\pi} \Big\{ & C_M \left[\epsilon_W G_M^{\gamma p} - G_M^{\gamma n} - G_M^s \right]^2 \\ & + C_E \left[\epsilon_W G_E^{\gamma p} - G_E^{\gamma n} - G_E^s \right]^2 + C_A (F_A - F_A^s)^2 \\ & + C_{AM} (F_A - F_A^s) \left(\epsilon_W G_M^{\gamma p} - G_M^{\gamma n} - G_M^s \right) \Big\} \end{aligned} \tag{143}$$

$$\begin{aligned} \frac{d\sigma_{\overline{\nu} p \to \overline{\nu} p}}{dQ^2} = \frac{G_F^2}{2\pi} \Big\{ & C_M \left[\epsilon_W G_M^{\gamma p} - G_M^{\gamma n} - G_M^s \right]^2 \\ & + C_E \left[\epsilon_W G_E^{\gamma p} - G_E^{\gamma n} - G_E^s \right]^2 + C_A (F_A - F_A^s)^2 \\ & - C_{AM} (F_A - F_A^s) \left(\epsilon_W G_M^{\gamma p} - G_M^{\gamma n} - G_M^s \right) \Big\} \end{aligned} \tag{144}$$

where $\epsilon_W = 1 - 4\sin^2\theta_W$ and G_F is the Fermi constant. The Q^2 dependence of the form factors has been suppressed in Eqs. (143) and (144). The kinematic quantities C_M, C_E, C_A, and C_{AM} above are defined as

$$C_M = \frac{1}{2}y^2 \tag{145}$$

$$C_E = 1 - y - \frac{My}{2E_\nu} \tag{146}$$

$$C_A = 1 - y + \frac{1}{2}y^2 + \frac{My}{2E_\nu} \tag{147}$$

$$C_{AM} = 2y\left(1 - \frac{1}{2}y\right) \tag{148}$$

where $y = Q^2/(2m_pE_\nu)$ and E_ν is the incident neutrino energy. The neutral current cross sections include terms independent of the strange form factors as well as terms with linear and quadratic dependencies on G_M^s, G_E^s, and F_A^s.

The corresponding charged current cross sections are [116]

$$\frac{d\sigma_{\nu n\to\mu^- p}}{dQ^2} = \frac{G_F^2}{2\pi}|V_{ud}|^2\left\{C_M\left(G_M^{\gamma p} - G_M^{\gamma n}\right)^2 + C_E\left(G_E^{\gamma p} - G_E^{\gamma n}\right)^2 + C_A F_A^2 + C_{AM}F_A\left(G_M^{\gamma p} - G_M^{\gamma n}\right)\right\} \tag{149}$$

$$\frac{d\sigma_{\overline{\nu}p\to\mu^+ n}}{dQ^2} = \frac{G_F^2}{2\pi}|V_{ud}|^2\left\{C_M\left(G_M^{\gamma p} - G_M^{\gamma n}\right)^2 + C_E\left(G_E^{\gamma p} - G_E^{\gamma n}\right)^2 + C_A F_A^2 - C_{AM}F_A\left(G_M^{\gamma p} - G_M^{\gamma n}\right)\right\} \tag{150}$$

where $|V_{ud}|^2$ is the square of the Cabibbo-Kobayashi-Maskawa matrix element mixing up and down quarks. The Q^2 dependence of the form factors has again been suppressed in Eqs. (149) and (150). It is necessary to check whether the equivalent free scattering cross section obtained by E734 for quasielastic knockout is appropriate to use to extract the relative strengths of the strange magnetic form factors from the E734 charged current data. Alberico *et al.* showed that while including final-state interactions between the ejected nucleon and the residual nucleus suggests that only half of the ^{12}C reactions correspond to elastic proton knockout, the ratios, Eqs. (125)-(127) are affected at the percent level for neutrino energies greater than 1 GeV [117]. Since E734 reported ratios, Eqs. (125)-(127), only elastic scattering of neutrinos on free protons were considered.

Integrating the cross sections over Q^2, it is possible to compare these results with the ratios reported by E734. The neutral current ratio R, Eq. (125), is formed by the ratio of Eq. (144) to Eq. (143). The charged current ratios R_ν, Eq. (126), and $R_{\overline{\nu}}$, Eq. (127), are the ratios of Eq. (143) to Eq. (149) and Eq. (144) to Eq. (150) respectively.

By forming the asymmetry of neutral current to charged current interactions, defined as the ratio of the difference between Eqs. (143) and (144) to the difference between Eqs. (149) and (150),

$$\mathcal{A}(Q^2) = \frac{(d\sigma_{\nu p\to\nu p}/dQ^2) - (d\sigma_{\overline{\nu}p\to\overline{\nu}p}/dQ^2)}{(d\sigma_{\nu n\to\mu^- p}/dQ^2) - (d\sigma_{\overline{\nu}p\to\mu^+ n}/dQ^2)} \ , \tag{151}$$

model independent information on the axial, F_A^s, and magnetic, G_M^s, strange form factors of the nucleon can be obtained [117]. The differences in the cross sections can be written in terms of the form factors so that the asymmetry becomes

$$\mathcal{A}(Q^2) = \frac{1}{4|V_{ud}|^2}\left(1 - \frac{F_A^s}{F_A}\right)\left(1 - 2\sin^2\theta_W \frac{G_M^{\gamma p}}{G_M^3} - \frac{G_M^s}{2G_M^3}\right) \ , \tag{152}$$

where F_A is the charged current axial form factor and $G_M^3 = 0.5(G_M^{\gamma p} - G_M^{\gamma n})$ is the charged current isovector magnetic form factor of the nucleon. Note that $\mathcal{A}$ is independent of the electric form factors.

To compare the calculations to the neutrino energy and momentum transfer averaged BNL E734 ratios, in Eqs. (125)-(127), they integrated over the neutrino energy spectrum, Eq. (124), and Q^2 to obtain the integral asymmetry

$$\langle\mathcal{A}\rangle = \frac{\langle\sigma_{\nu p\to\nu p}\rangle - \langle\sigma_{\overline{\nu}p\to\overline{\nu}p}\rangle}{\langle\sigma_{\nu n\to\mu^- p}\rangle - \langle\sigma_{\overline{\nu}p\to\mu^+ n}\rangle} \tag{153}$$

$$= \frac{R_\nu(1-R)}{1 - RR_\nu/R_{\overline{\nu}}} \tag{154}$$

$$= 0.136 \pm 0.008 \pm 0.019 \tag{155}$$

from the data, Eqs. (125)-(127).

Dipole parameterizations of the non-strange and strange form factors were assumed. The strange axial and vector form factors are [117]

$$F_A^s(Q^2) = \frac{g_A^s M_A^4}{(M_A^2 + Q^2)^2} \tag{156}$$

$$G_M^s(Q^2) = \frac{\mu_s M_V^4}{(M_V^2 + Q^2)^2} \tag{157}$$

$$G_E^s(Q^2) = \frac{\rho_s Q^2}{4m_p^2}\frac{M_V^4}{(M_V^2 + Q^2)^2} \tag{158}$$

where the strange couplings g_A^s, μ_s and ρ_s are left as free parameters. The vector and axial cutoff masses are $M_V = 0.84$ GeV and $M_A = 1.032$ GeV respectively. Other Q^2 parameterizations of the form factors

stronger than the dipole would reduce the overall effect of strangeness at high Q^2 but in the range $0.5 < Q^2 < 1$ GeV^2 changing the Q^2 dependence has a very weak effect on the results.

The ratios R_ν, $R_{\overline{\nu}}$, and R and the asymmetry $\mathcal{A}$ are shown in Fig. 22 along with several choices of g_A^s, μ_s, and ρ_s. Note that $\mathcal{A}$ is independent of ρ_s. The ratios and asymmetry are given as a function of μ_s for

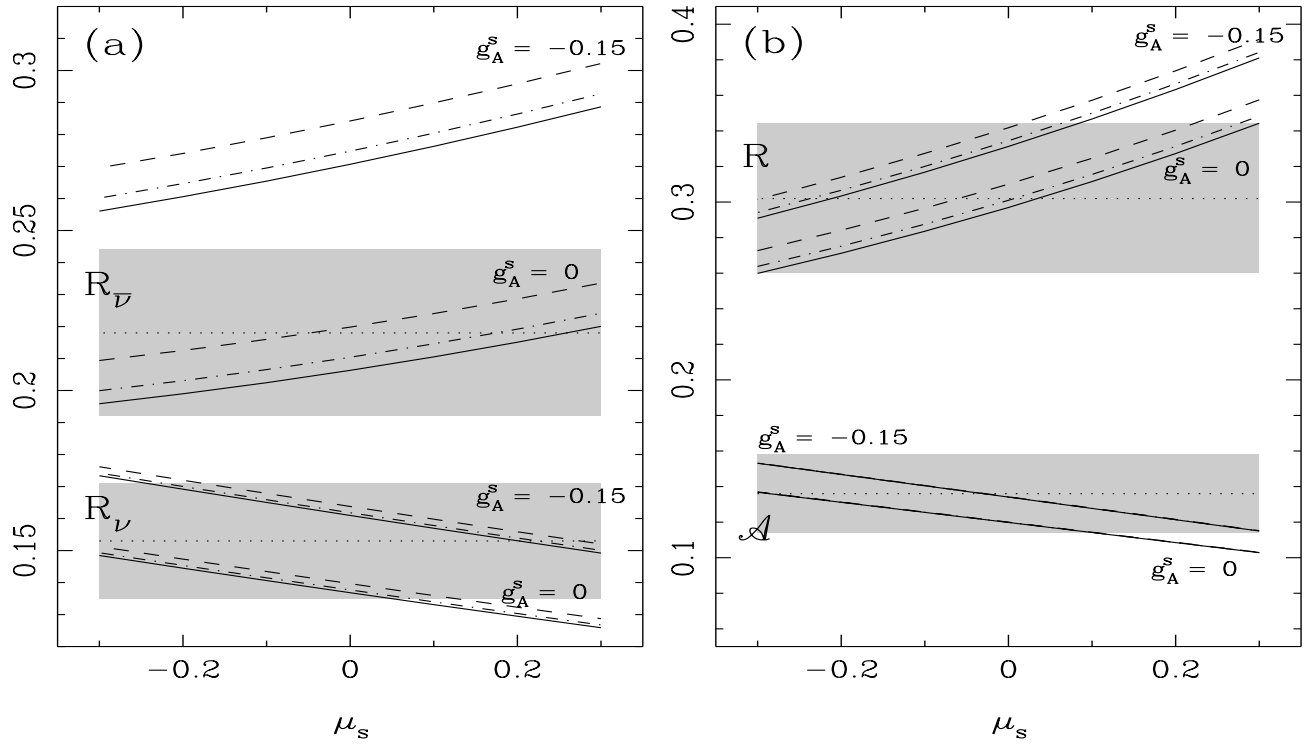

Fig. 22. The ratios R_ν, $R_{\overline{\nu}}$ (a), and R and the asymmetry $\mathcal{A}$ (b) are calculated as a function of μ_s and compared to the E734 data (shaded areas). All the calculations correspond to elastic scattering. Two choices of the axial coupling g_A^s are shown: 0 and -0.15. For each value of g_A^s, three values of ρ_s are chosen: -2 (dot-dashed), 0 (solid), and 2 (dashed). Reproduced from Ref. [117] with permission from Elsevier Science.

$g_A^s = 0$ and -0.15 with $\rho_s = -2$, 0, and 2. Changing g_A^s influences the ratios more than does changing ρ_s, especially for $R_{\overline{\nu}}$. In fact, the sensitivity of $R_{\overline{\nu}}$ to g_A^s excludes $g_A^s \leq -0.15$. The calculations of R_ν and $\mathcal{A}$ are most consistent with the E734 data when g_A^s is close to zero and μ_s is negative. Varying the axial cutoff M_A by $\pm 3.5\%$ only has a significant effect on $R_{\overline{\nu}}$. Lowering M_A increases the allowed range of g_A^s if $\mu_s = \rho_s = 0$ while increasing M_A restricts g_A^s to values close to zero.

Although the results obtained by the SAMPLE collaboration, Eq. (121), suggest that μ_s should be positive, the large uncertainties cannot rule out $\mu_s \leq 0$. Thus so far the E734, SAMPLE, and HAPPEX results are consistent with each other. As pointed out in Ref. [117], if the parity-odd asymmetry measurements are improved, then the more stringent bounds on μ_s can place better constraints on g_A^s and

ρ_s. The strange form factors have also been computed in a light-cone approach [118] and compared to the HAPPEX data. In this case, Melnitchouk and Malheiro calculated the combination of G_E^s and G_M^s in Eq. (123) and found that the strange electric and magnetic form factors were small and positive, consistent with the experiments.

3.2.4 Strange sea summary

The difference between the s and $\overline{s}$ distributions determined by the CCFR collaboration [22] has been studied in the context of meson cloud models [109–112] and has been modeled by gluon splitting into s and $\overline{s}$ quarks with different effective masses [107]. Meson cloud models tend to produce larger differences between $s(x)$ and $\overline{s}(x)$ than can be accommodated by the data, leading Ji and Tang to suggest that the strange sea is highly localized [107]. However, further measurements are needed with analyses based on more recent parton distribution functions. A reanalysis of the neutrino data is underway which could provide some answers [95].

Information on strange form factors in the nucleon has been obtained by the SAMPLE [97], HAPPEX [98], and E734 [99] collaborations. The results are consistent with each other and show that the strange form factors could be small and positive but are also consistent with zero [117].

3.3 Heavy quark contributions to the sea

Quarks more massive than the strange quark, *e.g.* charm and bottom quarks, have also been included in global analysis of parton distribution functions. (See Ref. [25] for a recent discussion and further references.) Early treatments of heavy quark parton distributions assumed that below a scale $Q^2 \sim m_Q^2$, there are n_f flavors in the perturbative sea and in the calculation of α_s. When $Q^2 > m_Q^2$, n_f+1 massless flavors are included in the perturbative sea and the running coupling constant. Thus above $Q^2 = m_Q^2$, the heavy quark is treated as massless [26]. This scheme is now generally referred to as the Variable Flavor Number scheme. At the opposite extreme, the heavy quark is never treated as part of the nucleon sea but is produced perturbatively through photon-gluon fusion. The number of flavors remains fixed, regardless of Q^2. This treatment, used in the GRV 94 parton densities [27], is referred to as the Fixed Flavor Number scheme. Obviously neither of these schemes is correct at all Q^2. The Fixed Flavor Number scheme is good near threshold but cannot incorporate large logarithms at $Q^2 \gg m_Q^2$ while the heavy quark should not be treated as massless near $Q^2 \sim m_Q^2$, as in the Variable Flavor Number scheme. Interpolating schemes, such as the one used by CTEQ [25,119], have been introduced which reproduce relevant features of both schemes. The heavy quarks are essentially as produced by photon-gluon fusion when $Q^2 \sim m_Q^2$ and behave as massless quarks when $Q^2 \gg m_Q^2$. All three schemes have been included in the recent global analysis by the CTEQ collaboration. The charm quark distribution from three of their fits is shown in Fig. 23.

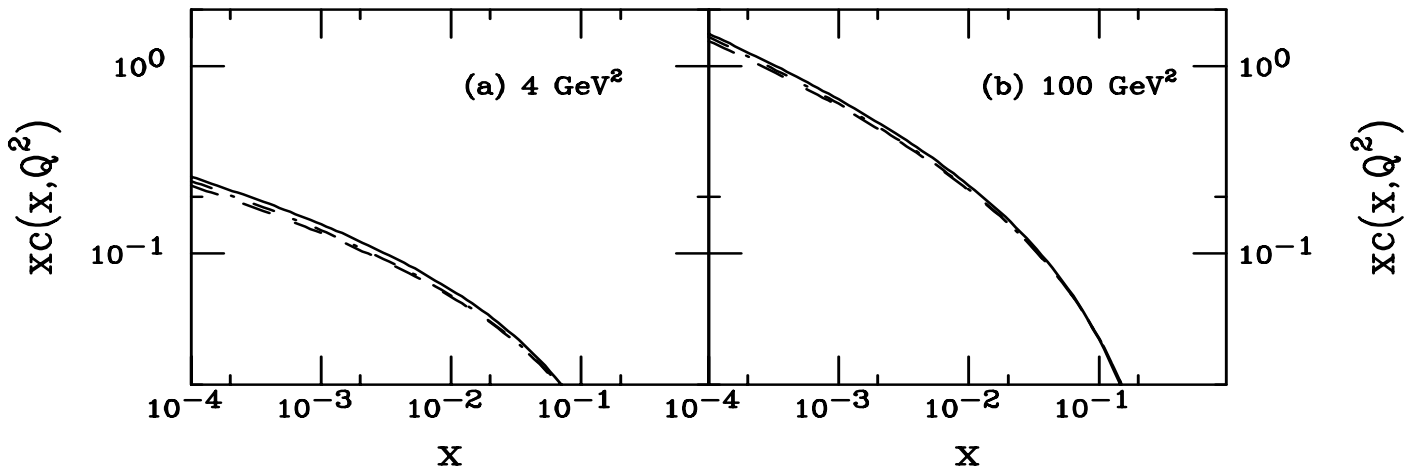

Fig. 23. Charm quark parton distribution in the Variable Flavor Number scheme, CTEQ 5M (solid), the Fixed Flavor Number scheme, CTEQ 5FF (dashed), and the interpolating scheme of Ref. [119], CTEQ 5HQ (dot-dashed).

Charm DIS data are discussed first. The EMC large x charm data [120] implied some nonperturbative source of charm production. These data have not been followed up with subsequent large x charm measurements. More recent HERA data [121,122] suggest that only perturbative production is needed at low x. Models of nonperturbative charm production are then introduced which could be important at large x.

3.3.1 Current experimental evidence

The European Muon Collaboration, EMC, [120] at CERN first measured the charm structure function, $F_{2\,c}^{\gamma p}$. In the relatively large x region of the EMC measurement, charm only contributed $\approx 1\%$ to the total structure function $F_2^{\gamma p}$. Charm was identified by dimuon events, where one muon was consistent with charm meson decay, and trimuon events, which were consistent with a $\mu^+\mu^-$ pair produced by the semileptonic decays of a pair of charm mesons. In both cases, the additional final-state muon was the scattered projectile muon. They compared their results to a leading order photon-gluon fusion calculation. In their analysis, they assumed a simple gluon momentum distribution, $xg(x) = 3(1-x)^5$ and used the $c\overline{c}$ pair mass in the scale of the strong coupling constant, $\mu^2 = Q^2 + m_{c\overline{c}}^2$. They included $\sim 83\%$ of the $c\overline{c}$ cross section below the $D\overline{D}$ threshold in the total charm cross section. Their data, which has never been incorporated into global analyses of parton distributions, are shown in Fig. 24 as a function of Q^2 with uncertainties on both x and Q^2 given. A nonnegligible Q^2 dependence is clearly indicated.

More recently, the charm structure function has been measured to very low x at HERA [121,122]. At these low x values, $F_{2\,c}^{\gamma p}/F_2^{\gamma p} \sim 0.25$ at $Q^2 \sim 11$ GeV^2, a surprisingly large fraction. The charm structure

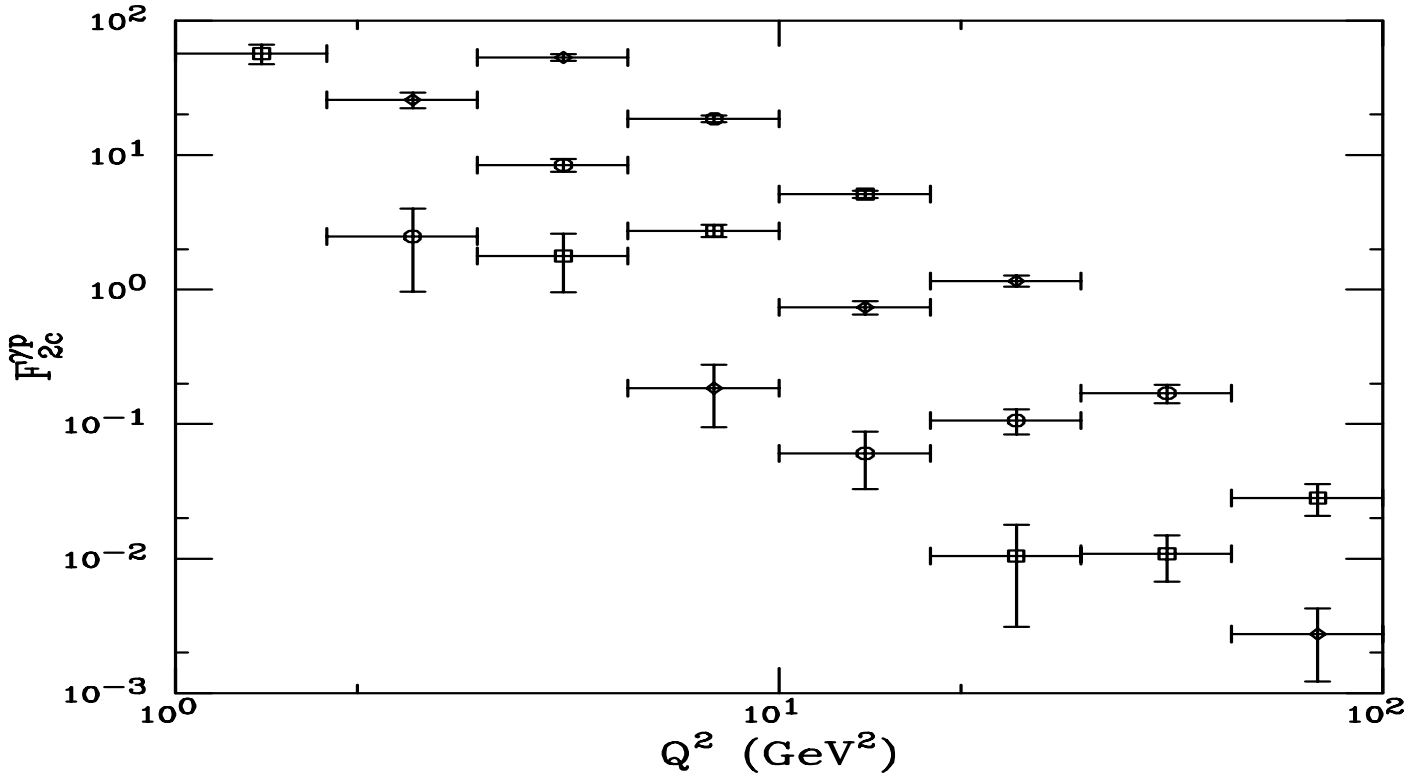

Fig. 24. The charm structure function $F_{2\,c}^{\gamma p}$ as a function of Q^2 measured by the European Muon Collaboration [120]. From top to bottom the values of the x bins are: 0.0044, 0.0078, 0.014, 0.025, 0.044, 0.078, 0.14, 0.25, and 0.44. To separate the data, $F_{2\,c}^{\gamma p}$ in each x bin is scaled by a factor of 4 from the next higher x bin. Therefore, only the highest x data (lowest points) have the correct scale. Only the statistical uncertainty is shown.

function is measured in the reactions $e^+p \to e^+D^{*\pm}X$ by studying the decay channels $D^{*+}(2010) \to D^0(1864)\pi_s^+ +$ charge conjugate where π_s^+ is a slow π^+. The D^0 and $\overline{D}^0$ from $D^{*\pm}$ decays subsequently decay into $K(n\pi)$ final states, $D^0 \to K^-\pi^+$ or $K^-\pi^+\pi^-\pi^+$ (+ charge conjugates) resulting in $D^{*\pm}$ decays with two or four pions in the final state. Once the final states have been reconstructed, the $c\overline{c}$ cross section is obtained from the $D^{*\pm}$ production cross section, extrapolating to the full kinematical phase space, and employing the hadronization fraction $F(c \to D^{*+})$ to obtain the total charm cross section. The extrapolations necessary to go to full phase space were significant, resulting in a factor of ten correction for the four-pion final state at low Q^2 and a factor of four at high Q^2, and neglect charm production by processes other than photon-gluon fusion. The $c\overline{c}$ production cross section is then

$$\frac{d^2\sigma^{c\overline{c}}(x,Q^2)}{dxdQ^2} = \frac{2\pi\alpha^2}{xQ^2}\left\{\left[1+(1-y)^2\right]F_{2c}^{\gamma p}(x,Q^2) - y^2 F_{Lc}^{\gamma p}(x,Q^2)\right\} \ , \tag{159}$$

where the contribution from the second term is negligible. Equation (159) can be obtained from Eq. (11) for the virtual photon by changing integration variables from y to Q^2 and taking the $m_h/E \ll 1$ limit.

The hadronization fraction of charm to D^*, assuming that final state production of charm hadrons is the same in e^+e^- annihilation and DIS, is $F(c \to D^*) = 0.222 \pm 0.014 \pm 0.014$ [123]. They assume $m_c = 1.4$ GeV and the renormalization and factorization scales used in the photon-gluon fusion production of charm at NLO are $\mu = \sqrt{4m_c^2 + Q^2}$. Recall that the EMC data were analyzed with $\mu = \sqrt{m_{c\bar{c}}^2 + Q^2}$. The data from the two different decay modes are combined in the final data set and the charm structure function is extracted from Eq. (159). The ZEUS data are shown as a function of Q^2 in Fig. 25. The structure function shows significant Q^2 dependence as well as a steep rise as x decreases with Q^2 fixed. The ZEUS data and the low x EMC data are consistent with each other and with perturbative generation of the charm sea.

Since H1 has a smaller charm sample, they only present the ratio $F_{2\,c}^{\gamma p}/F_2^{\gamma p}$ averaged over the kinematic range $10 < Q^2 < 100$ GeV^2 and $0.0008 < x < 0.008$. They found $F_{2\,c}^{\gamma p}/F_2^{\gamma p} = 0.237 \pm 0.021\,^{+\,0.043}_{-\,0.039}$, an order of magnitude greater than at larger x. Their result is compatible with the ZEUS result in the same kinematic interval.

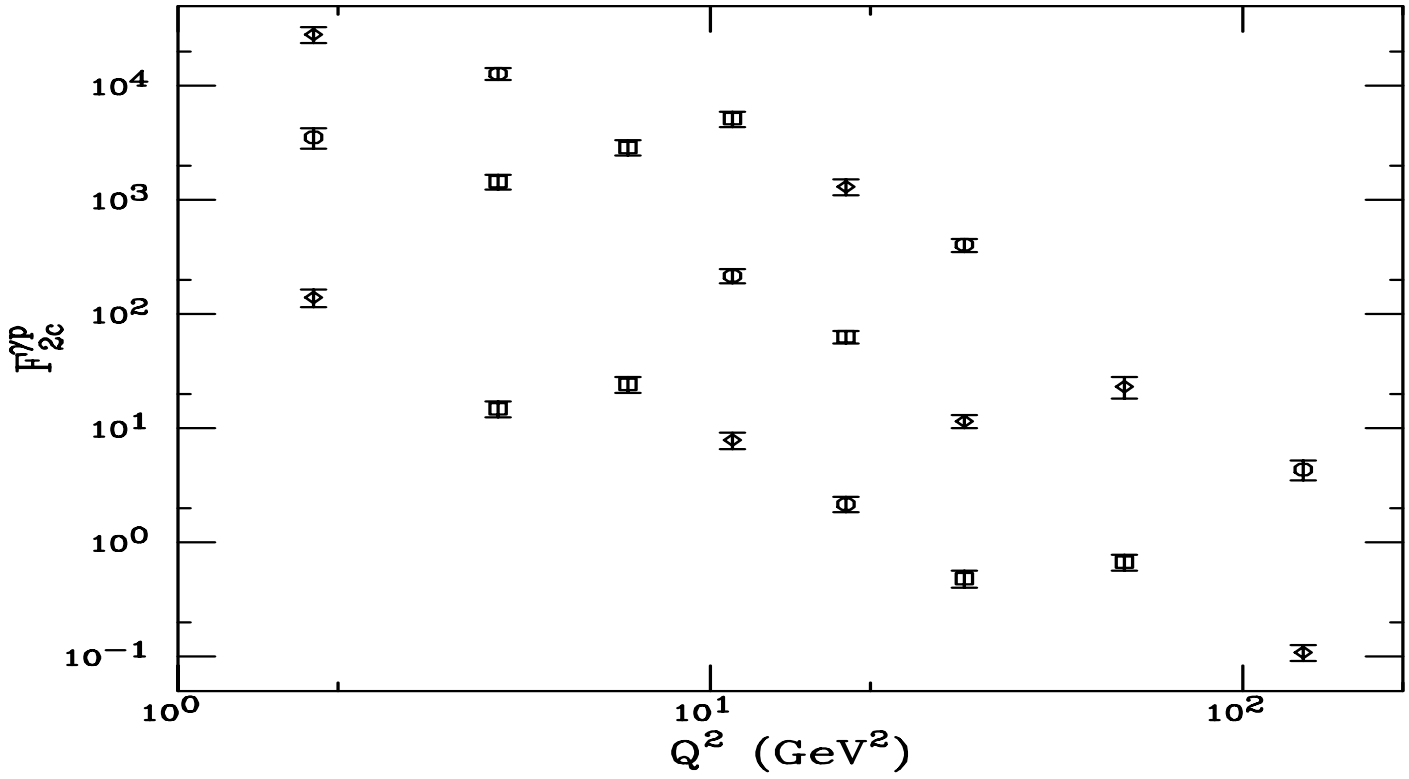

Fig. 25. The charm structure function $F_{2\,c}^{\gamma p}$ as a function of Q^2 measured by ZEUS [121]. From top to bottom the values of the x bins are: 0.00005, 0.00013, 0.0003, 0.0005, 0.0008, 0.0012, 0.002, 0.004, 0.008, and 0.02. To separate the data, $F_{2\,c}^{\gamma p}$ in each x bin is scaled by a factor of 4 from the next higher x bin. Therefore, only the highest x data (lowest points) have the correct scale. Only the statistical uncertainty is shown.

3.3.2 Nonperturbative heavy quarks

The inclusion of heavy quarks in the perturbative generation of the sea and global analyses of the parton distributions has already been discussed. However, the large x and Q^2 EMC charm structure function data hinted that these results were inconsistent with production of charm by photon-gluon fusion. This led to the speculation that charm could be generated in the sea by a higher-twist mechanism. Two nonperturbative models of charm in the sea are discussed here, intrinsic charm [114] and the meson cloud model [109,124].

3.3.3 Intrinsic charm

The QCD wavefunction of a hadron can be represented as a superposition of quark and gluon Fock states. For example, at fixed light-cone time, a hadron wavefunction can be expanded as a sum over the complete basis of free quark and gluon states: $|\Psi_h\rangle = \sum_m |m\rangle\, \psi_{m/h}(x_i, k_{T,i})$ where the color-singlet states, $|m\rangle$, represent the fluctuations in the hadron wavefunction with the Fock components $|q_1q_2q_3\rangle$, $|q_1q_2q_3g\rangle$, $|q_1q_2q_3c\overline{c}\rangle$, *etc.* The boost-invariant light-cone wavefunctions, $\psi_{m/h}(x_i, k_{T,i})$ are functions of the relative momentum coordinates $x_i = k_i^+/P^+$ and $k_{T,i}$. Momentum conservation demands $\sum_{i=1}^n x_i = 1$ and $\sum_{i=1}^n \vec{k}_{T,i} = 0$ where n is the number of partons in state $|m\rangle$. For example, intrinsic charm, IC, fluctuations [114] can be liberated by a soft interaction which breaks the coherence of the Fock state [125] provided the system is probed during the characteristic time that such fluctuations exist.

Microscopically, the intrinsic heavy quark Fock component in the proton wavefunction, $|uudc\overline{c}\rangle$, is generated by virtual interactions such as $gg \to Q\overline{Q}$ where the gluons couple to two or more valence quarks. The probability for $c\overline{c}$ fluctuations to exist in a hadron is higher twist since it scales as $1/m_c^2$ relative to the extrinsic, EC, leading-twist production by photon-gluon fusion [126].

The dominant Fock state configurations are not far off shell and thus have minimal invariant mass, $M^2 = \sum_i^n \widehat{m}_i^2/x_i$ where $\widehat{m}_i^2 = m_i^2 + \langle \vec{k}_{T,i}^2 \rangle$ is the square of the average transverse mass of parton i. The general form of the Fock state wavefunction appropriate to any frame at fixed light-cone time is

$$\Psi(x_i, \vec{k}_{\perp i}) = \frac{\Gamma(x_i, \vec{k}_{\perp i})}{m_h^2 - M^2} \tag{160}$$

where Γ is a vertex function, expected to be a slowly-varying, decreasing function of $m_h^2 - M^2$. The particle distributions are then controlled by the light-cone energy denominator and phase space. This form for the higher Fock components is applicable to an arbitrary number of light and heavy partons. Intrinsic $c\overline{c}$ Fock components with minimum invariant mass correspond to configurations with equal rapidity constituents. Thus, unlike extrinsic heavy quarks generated from a single parton, intrinsic heavy quarks carry a larger fraction of the parent momentum than the light quarks in the state [114].

The parton distributions reflect the underlying shape of the Fock state wavefunction. Assuming it is sufficient to use $\langle k_T^2 \rangle$ for the transverse momentum, the probability distribution as a function of x in a general n–particle intrinsic $c\overline{c}$ Fock state is

$$\frac{dP_{\rm IC}}{dx_i \cdots dx_n} = N_n \, \frac{\delta(1 - \sum_{i=1}^n x_i)}{(m_h^2 - \sum_{i=1}^n (\widehat{m}_i^2/x_i))^2} \, , \tag{161}$$

where N_n normalizes the n-particle Fock state probability.

The intrinsic charm structure function at leading order, LO, and next-to-leading order, NLO, is now described. At LO in the heavy quark limit, $\widehat{m}_c$, $\widehat{m}_{\overline{c}} \gg m_h$, $\widehat{m}_q$,

$$\begin{aligned} \frac{dP_{\rm IC}}{dx_i \cdots dx_n} &= N_n \frac{x_c x_{\overline{c}}}{(x_c + x_{\overline{c}})^2} \, \delta(1 - \sum_{i=1}^n x_i) \\ F_{2\,c}^{\rm IC\,LO}(x) &= \frac{8}{9} x c(x) = \frac{8}{9} x \int dx_1 \cdots dx_{\overline{c}} \frac{dP_{\rm IC}}{dx_i \cdots dx_{\overline{c}} dx_c} \\ &= \frac{8}{9} x \frac{1}{2} N_5 x^2 [\frac{1}{3}(1-x)(1 + 10x + x^2) + 2x(1+x)\ln x] \, . \end{aligned} \tag{162}$$

If $n = 5$, the minimal intrinsic charm Fock state of the proton, $|uudc\overline{c}\rangle$, is assumed and $P_{\rm IC} = 1\%$ [114], then $N_5 = 36$. In what follows, a 1% intrinsic charm contribution is assumed unless otherwise noted.

Hoffmann and Moore [127] incorporated mass effects into the analysis. They first included threshold effects by introducing a scaling variable $\xi = 2ax/[1+(1+4x^2 m_p^2/Q^2)^{1/2}]$ with $a = [1+(1+4m_c^2/Q^2)^{1/2}]/2$. The $c\overline{c}$ mass threshold requires $\xi \leq \gamma < 1$ where $\gamma = 2a\hat{x}[1 + (1 + 4\hat{x}^2 m_p^2/Q^2)^{1/2}]^{-1}$ and $\hat{x} = Q^2/[Q^2 + 4m_c^2 - m_p^2]$. Then Eq. (162) is replaced by

$$F_{2\,c}^{\rm IC\,LO}(x, Q^2, m_c^2) = \frac{8}{9} \xi c(\xi, \gamma) \, , \tag{163}$$

with $c(z, \gamma) = c(z) - z c(\gamma)/\gamma$ for $z \leq \gamma$ and zero otherwise. The final LO result can be written more generally as in Eq. (18) of Ref. [127],

$$F_{2\,c}^{\rm IC\,LO}(x, Q^2, m_c^2) = \frac{8x^2 Q^3}{9(Q^2 + 4x^2 m_p^2)^{3/2}} \left[\frac{(Q^2 + 4m_c^2)}{\xi Q^2} c(\xi, \gamma) + \hat{g}(\xi, \gamma) \right] \tag{164}$$

where

$$\hat{g}(\xi, \gamma) = \frac{6x m_p^2}{(Q^2 + 4x^2 m_p^2)} \int_\xi^\gamma \frac{dt}{t} c(t, \gamma) \left(1 - \frac{m_c^2}{m_p^2 t^2}\right) \left[1 + \frac{2xt m_p^2}{Q^2} + \frac{2x m_c^2}{tQ^2}\right] .$$

The NLO IC component of the structure function is given by

$$F_{2\,c}^{\mathrm{IC\,NLO}}(x,Q^2,m_c^2) = \frac{8}{9}\xi \int\limits_{\xi/\gamma}^{1} \frac{dz}{z} c(\xi/z,\gamma)\sigma_2^{(1)}(z,\lambda)\,. \tag{165}$$

The lowest order cross section is normalized to $\sigma_2^{(0)}(z,\lambda) = \delta(1-z)$. The NLO QCD corrections to the IC contribution are given in Eq. (51) of Ref. [127]. The IC results at NLO are the sum of the kinematically corrected LO result, Eq. (164), and the full NLO correction.

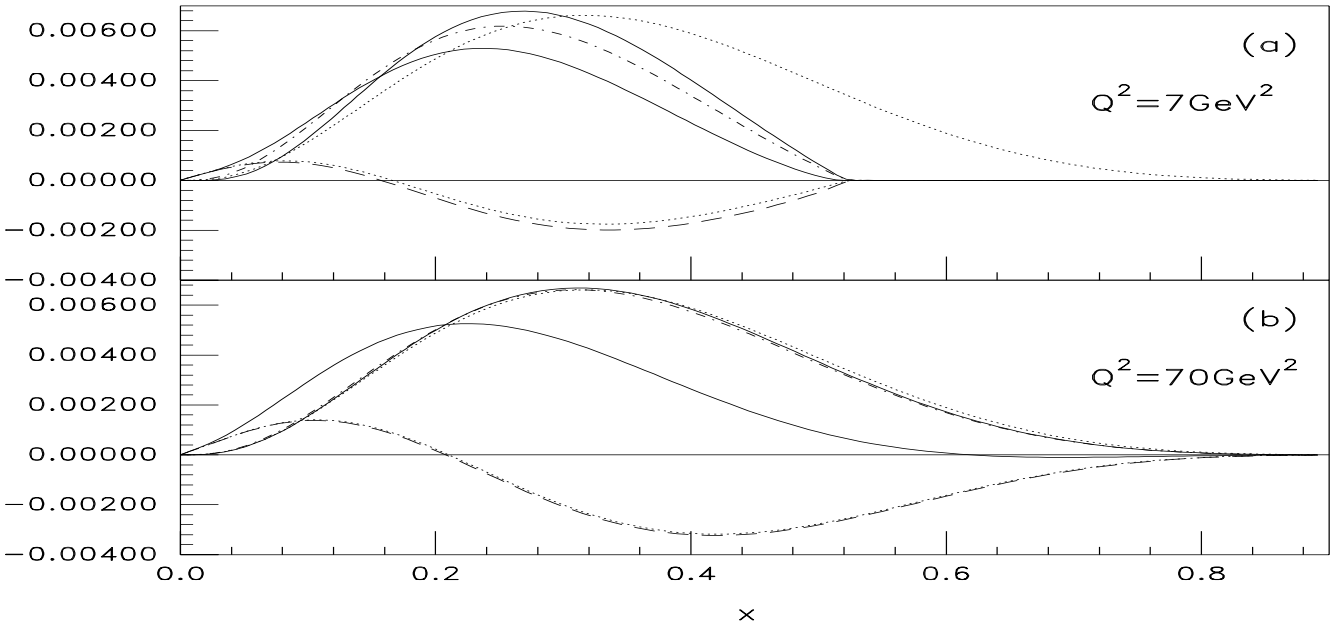

Fig. 26. (a) The contributions to the structure function $F_{2\,c}^{\mathrm{IC}}(x,Q^2,m_c^2)$ at $Q^2 = 7$ GeV^2: the massless result, Eq. (162), (upper dotted line); the ξ-scaling result, Eq. (163), (dot-dashed line); and the kinematically corrected formula, Eq. (164), (top solid line). Also shown are the NLO corrections given by Eq. (165) with the leading-log result, Eq. (54) in [127], (dashed line), and the full result, Eq. (51) in [127], (lower dotted line). The sum of Eqs. (164) and (165) using the full result, Eq. (51) in [127], represents the total IC contribution to $F_{2\,c}^{\mathrm{IC\,NLO}}(x,Q^2,m_c^2)$ (lower solid line). (b) Same as part (a) for $Q^2 = 70$ GeV^2. Reproduced from Ref. [128] with permission from Elsevier Science.

Figure 26 shows the LO and NLO IC contributions to $F_2(x,Q^2,m_c^2)$ for $Q^2 = 7$ and 70 GeV^2. At LO the massless, Q^2 independent, result, Eq. (162), the ξ scaling formula, Eq. (163), and the full calculation, Eq. (164), show substantial differences at low Q^2 while the three are nearly indistinguishable when Q^2 is large. The NLO corrections calculated using Eq. (165) are also shown. The leading-logarithmic approximation, Eq. (54) in [127], and the complete result, Eq. (51) in [127], differ at small Q^2 but are almost identical at large Q^2. The total NLO IC results are actually negative at large x and Q^2, indicating that even higher order terms are needed in the perturbative expansion.

The EMC data have been analyzed with a combination of photon-gluon fusion and intrinsic charm, first by Hoffmann and Moore [127] and later by Harris *et al.* [128]. In both cases, the intrinsic charm calculation was carried to next-to-leading order. While only leading order photon-gluon fusion was available for the first study [127], in the more recent analysis, the photon-gluon fusion calculation was carried to next-to-leading order as well [128]. Photon-gluon fusion is used to generate charm perturbatively because at the measured Q^2 of the EMC experiment, the mass of the charm quark is not small.

To NLO [129], the extrinsic charm structure function $F_{2\,c}^{\gamma p}$ is calculated from the inclusive virtual photon-induced reaction at the parton level, $\gamma^* + a_1 \to c + \overline{c} + a_2$ where a_1 and a_2 are massless partons. In an inclusive calculation, the $\overline{c}$ and a_2 momenta are integrated over. The charm structure function is the sum of the longitudinal and transverse virtual photon total cross sections, $F_{2\,c}^{\gamma p} \propto (Q^2/4\pi^2\alpha)(\sigma_T + \sigma_L)$. At NLO, the extrinsic charm structure function is then

$$
\begin{aligned}
F_{2c}^{\gamma p}(x, Q^2, m_c^2) &= \frac{Q^2 \alpha_s(\mu^2)}{4\pi^2 m_c^2} \int_{\xi_0}^{1} \frac{d\xi}{\xi} \Big[e_c^2 f_g(\xi, \mu^2) c_{2,g}^{(0)} \Big] \\
&+ \frac{Q^2 \alpha_s^2(\mu^2)}{\pi m_c^2} \int_{\xi_0}^{1} \frac{d\xi}{\xi} \Bigg\{ e_c^2 f_g(\xi, \mu^2) \Bigg(c_{2,g}^{(1)} + \overline{c}_{2,g}^{(1)} \ln \frac{\mu^2}{m_c^2} \Bigg) \\
&+ \sum_{i=q,\overline{q}} f_i(\xi, \mu^2) \Bigg[e_c^2 \left(c_{2,i}^{(1)} + \overline{c}_{2,i}^{(1)} \ln \frac{\mu^2}{m_c^2} \right) + e_i^2 \, d_{2,i}^{(1)} + e_c \, e_i \, o_{2,i}^{(1)} \Bigg] \Bigg\} \; . \qquad (166)
\end{aligned}
$$

where $\xi_0 = x(4m_c^2 + Q^2)/Q^2$. The quark charges are in units of e. The parton momentum distributions in the proton are denoted by $f_i(\xi, \mu^2)$ where μ, the mass factorization scale, has been set equal to the renormalization scale in α_s. The scale independent parton coefficient functions, $c_{2,i}^{(l)}$, $l = 0, 1$, $\overline{c}_{2,i}^{(1)}$, $d_{2,i}^{(1)}$ and $o_{2,i}^{(1)}$ originate from the coupling of the virtual photon to the partons. The functions $c_{2,i}^{(l)}$ and $\overline{c}_{2,i}^{(1)}$ represent the virtual photon-charm quark coupling, thus appearing for both charged parton and gluon-induced reactions. The virtual photon-light quark coupling gives rise to $d_{2,i}^{(1)}$ while $o_{2,i}^{(1)}$ is an interference term proportional to $e_c e_i$.

The EMC data [130] with $\overline{\nu} = \overline{Q^2}/2m_p\overline{x} = 53, 95,$ and 168 GeV were fit by a sum of the photon-gluon fusion and IC components [128]. The normalization of both the IC and EC components are free parameters so that

$$
F_{2\,c}(x, \mu^2, m_c^2) = \epsilon F_{2\,c}^{\gamma p}(x, \mu^2, m_c^2) + \delta F_{2\,c}^{\rm IC}(x, \mu^2, m_c^2) \; , \qquad (167)
$$

with the scale $\mu = \sqrt{m_{c\overline{c}}^2 + Q^2}$. Since $\mu(m_{c\overline{c}}^2)$, an exclusive $c\overline{c}$ production calculation at NLO [131] was carried out to more precisely match the EMC analysis. The parameter ϵ, typically larger than unity, can be considered an estimate of the NNLO contribution to photon-gluon fusion. Since a 1% normalization of the IC component is already assumed, the fitted δ is the fraction of this normalization. Several different

	$\bar{\nu} = 53$ GeV		$\bar{\nu} = 95$ GeV		$\bar{\nu} = 168$ GeV	
PDF	ϵ	δ	ϵ	δ	ϵ	δ
CTEQ3 [115]	1.0 ± 0.6	0.4 ± 0.6	1.2 ± 0.1	0.4 ± 0.3	1.3 ± 0.1	0.9 ± 0.5
MRS G [132]	1.0 ± 0.7	0.3 ± 0.6	1.4 ± 0.2	0.3 ± 0.3	1.5 ± 0.1	0.8 ± 0.5
GRV 94 [27]	1.2 ± 0.8	0.3 ± 0.6	1.4 ± 0.2	0.3 ± 0.3	1.5 ± 0.1	0.9 ± 0.5

Table 4
Results of the least squares fit of the photon-gluon fusion and IC contributions to the EMC data according to Eq. (167). Adapted from [128].

parton distribution functions were used which produced essentially the same results. The results are presented in Table 4. The errors in the table correspond to a fit at the 95% confidence level. The final results for the combined model of Eq. (167) are shown in Fig. 27 for the CTEQ3, MRS G, and GRV 94 parton densities. Given the quality of the data, no statement can be made about the intrinsic charm content when $\bar{\nu} = 53$ and 95 GeV. However, with $\bar{\nu} = 168$ GeV an intrinsic charm contribution of $(0.86 \pm 0.60)\%$ is indicated. These results are consistent with those of the original analysis by Hoffman and Moore [127].

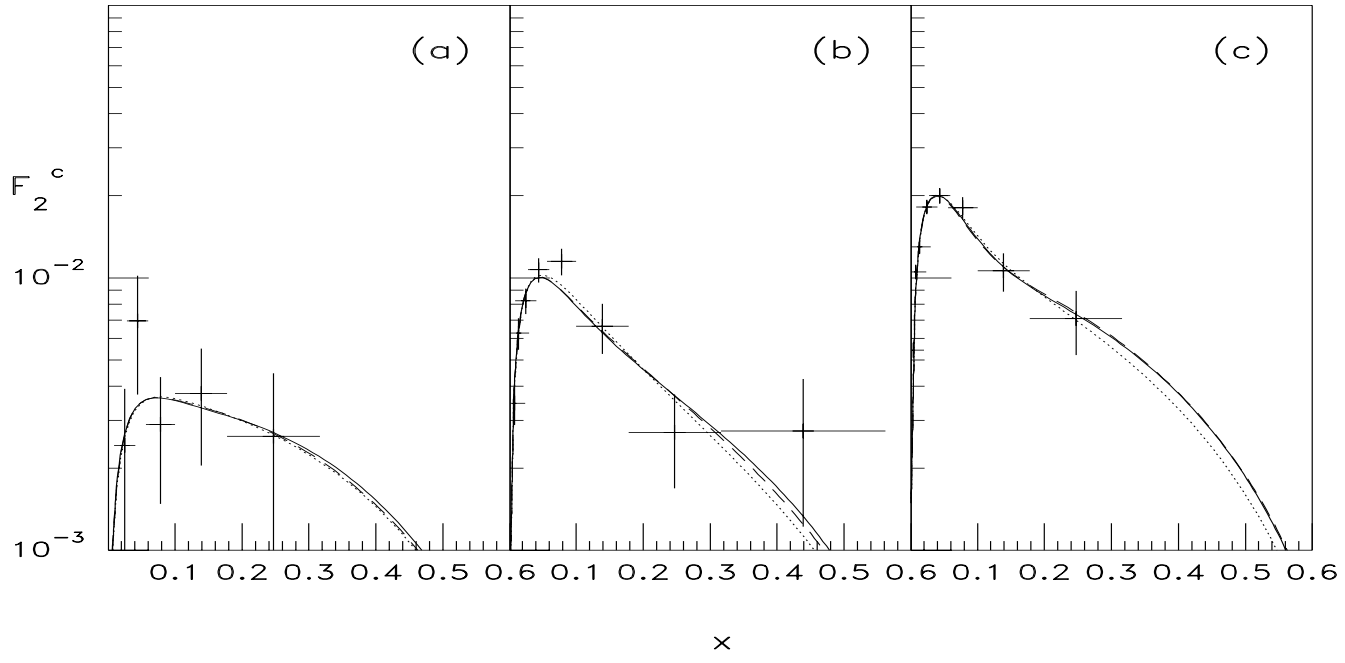

Fig. 27. (a) The EMC data for the structure function $F_{2\,c}(x, Q^2, m_c^2)$ at $\bar{\nu} = 53$ GeV are plotted as a function of x together with the fit from Eq. (167) with ϵ and δ taken from Table 4. The CTEQ3 (solid), MRS G (dashed) and GRV 94 HO (dotted) parton densities are shown. (b) Same as (a) for $\bar{\nu} = 95$ GeV. (c) Same as (a) for $\bar{\nu} = 168$ GeV. Reproduced from Ref. [128] with permission from Elsevier Science.

Only the intrinsic charm contribution to the charm structure function has been discussed here. There are many other applications of intrinsic charm in charm hadron production. See *e.g.* [126,133–136] for more details.

3.3.4 Meson cloud models

Paiva *et al.* have also calculated an "intrinsic" charm component of the nucleon sea within the context of the meson cloud model [109]. They assumed that the nucleon can fluctuate into $\overline{D}\Lambda_c$. The $\overline{c}$ distribution in the nucleon is then

$$x\overline{c}_N(x) = \int_x^1 dy\, f_{\overline{D}}(y)\, \frac{x}{y}\, \overline{c}_{\overline{D}}(\frac{x}{y}) \; . \tag{168}$$

where

$$f_{\overline{D}}(y) = \frac{g^2_{\overline{D}N\Lambda_c}}{16\pi^2}\, y \int_{-\infty}^{t_{\rm max}} dt\, \frac{[-t + (m_{\Lambda_c} - m_N)^2]}{[t - m^2_{\overline{D}}]^2}\, F^2(t) \; , \tag{169}$$

and $t_{\rm max} = m_N^2 y - m^2_{\Lambda_c} y/(1-y)$. In this case they chose a monopole form factor with $\Lambda_m = 1.2$ GeV. The coupling constant was assumed to be $g_{\overline{D}N\Lambda_c} = -3.795$. From heavy quark effective theories [137], the $\overline{c}$ distribution in the $\overline{D}$ is expected to be hard because in the bound state, the $\overline{c}$ exchanges momenta much less than m_c. They make the extreme assumption that the entire $\overline{D}$ momenta is carried by the charm quark, $\overline{c}_{\overline{D}} = x\delta(x-y)$. The resulting $\overline{c}$ distribution is compared to the intrinsic charm quark distribution in the heavy quark limit, Eq. (162), with $x\overline{c}_N = xc_N = 9F_{2\,c}^{\rm IC\,LO}/8$ in Fig. 28.

More recently Steffens *et al.* investigated all the charm structure function data with two variants of intrinsic charm [124]. The first was that of Eq. (162), called IC1 in their paper, while the second was a meson cloud model, IC2. In the second approach, the $\overline{c}$ distribution is obtained from the light cone distribution of $\overline{D}^0$ mesons in the nucleon,

$$\begin{aligned} \overline{c}^{\rm IC2}(x) &\approx f_{\overline{D}}(x) \\ &= \frac{1}{16\pi^2} \int_0^\infty dk_\perp^2 \frac{g^2(x,k_\perp^2)}{x(1-x)(s_{\overline{D}\Lambda_c} - m_N^2)^2} \frac{k_\perp^2 + (m_{\Lambda_c} - (1-x)m_N)^2}{1-x} \; . \end{aligned} \tag{170}$$

A hard charm momentum distribution was assumed in the $\overline{D}$, similar to that of Ref. [109]. The vertex function $g^2(x,k_\perp^2)$ is parameterized as $g^2 = g_0^2(\Lambda^2 + m_N^2)/(\Lambda^2 + s_{\overline{D}\Lambda_c})$ where $s_{\overline{D}\Lambda_c}$ is the square of the center of mass energy of the $\overline{D}\Lambda_c$ system and g_0^2 the coupling constant at $s_{\overline{D}\Lambda_c} = m_N^2$. For an intrinsic charm probability of 1%, $\Lambda \approx 2.2$ GeV. The charm distribution is then

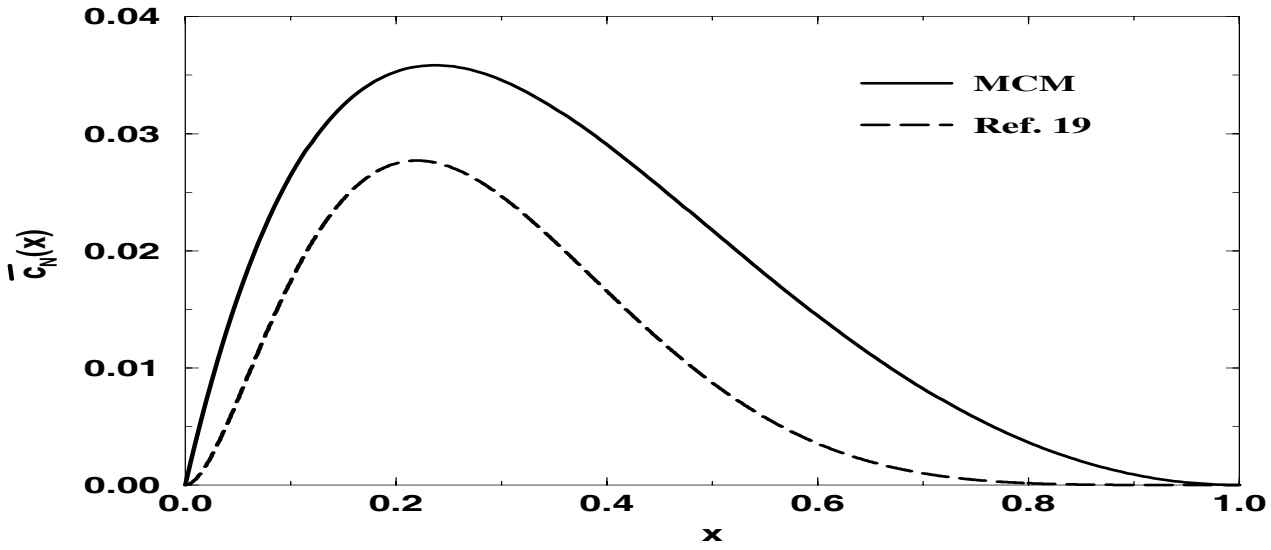

Fig. 28. The $\bar{c}_N$ distribution calculated with the meson cloud model, Eq. (168), (solid curve) compared to the intrinsic $\bar{c}_N$ distribution of Eq. (162) (dashed curve) labeled Ref. 19. Reproduced from Ref. [109] with permission from World Scientific.

$$c^{\mathrm{IC2}}(x) \approx \frac{3}{2} f_{\Lambda_c}\left(\frac{3x}{2}\right) \tag{171}$$

where the charm distribution in the Λ_c is assumed to be $c_{\Lambda_c} \sim \delta(x - 2/3)$ and $f_{\Lambda_c}(x) = f_{\overline{D}}(1-x)$.

Using several different schemes to calculate the extrinsic charm sea, Steffens *et al.* compared their two component model to the combined ZEUS and EMC data. As expected from the agreement of the low x ZEUS data to the perturbative generation of the charm sea, the ZEUS data show no sign of intrinsic charm. However, the EMC data still indicate a need for intrinsic charm at large x and Q^2, as found in Ref. [128]. The best results, shown in Fig. 29, are obtained in the fixed flavor scheme, as outlined at the beginning of this section. They find $P_{\mathrm{IC}} \sim 0.75\%$ for the standard massless intrinsic charm at leading order, their IC1, and $P_{\mathrm{IC}} \sim 0.4\%$ with their meson cloud approach, IC2 [124]. They claim that the data indicate a slight preference for model IC2. However, unlike the results shown in the previous section, they did not include the NLO corrections to $F_{2\,c}^{\mathrm{IC}}$ which reduce the large x structure function relative to Eq. (162), as seen in Fig. 26. Clearly, more data are needed at large x and Q^2 to finally resolve the situation.

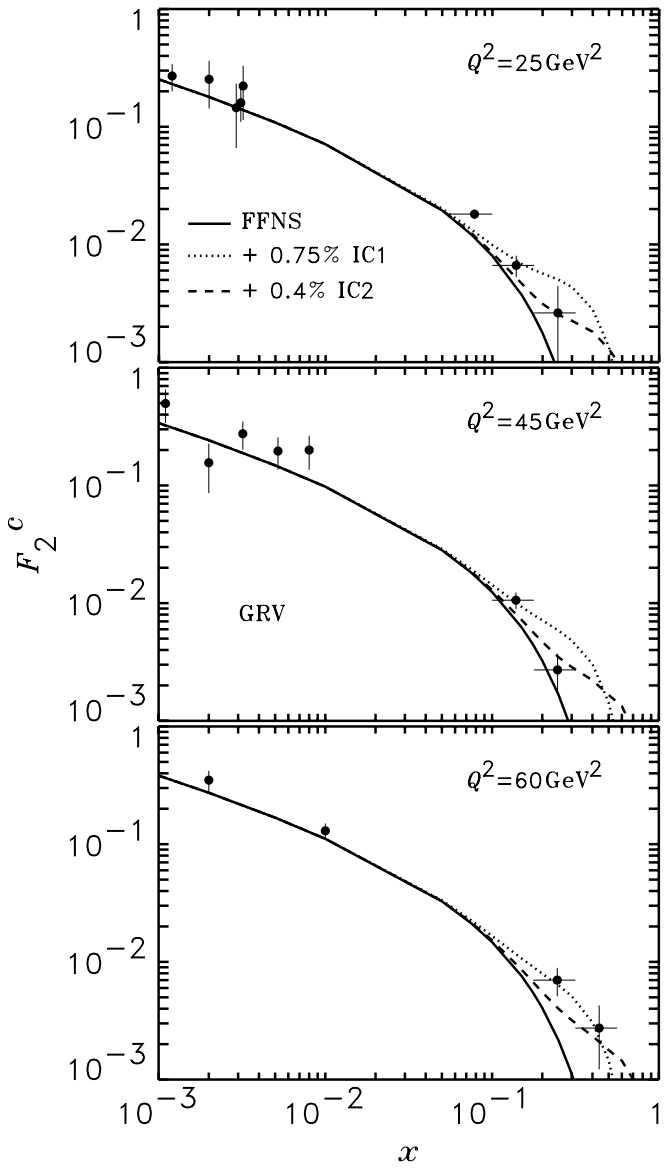

Fig. 29. The charm structure function calculated in the fixed flavor number scheme (FFNS) for three Q^2 bins with the intrinsic charm models IC1, Eq. (162), and IC2, Eqs. (170) and (171). The IC1 result is normalized to 0.75% while IC2 is normalized to 0.4%. The most recent GRV parton distributions [138] are used for the light quark and gluon densities. Reproduced from Ref. [124] with permission from Springer-Verlag.

3.3.5 Heavy sea summary

Considerable progress has been made in the understanding of the charm component in the nucleon sea, particularly at small x. Treating the heavy quark as massless at large Q^2 and massive at $Q^2 \sim m_Q^2$ put the heavy quark contribution to the sea on a firmer theoretical footing. Charm data at HERA [121,122]

are in good agreement with perturbative production of charm. However, the large x and Q^2 EMC data [120] still do not fit into this scheme. Intrinsic charm on the level of $\sim 1\%$ can explain this lower energy data [114,128]. Whether the c and $\overline{c}$ distributions are identical [114] or differ as in an *e.g.* $\overline{D}\Lambda_c$ cloud [124] is unclear. More data in this interesting region are needed.

In addition to the reconstructed charm structure function data at HERA, deep-inelastic scattering data with significant statistics at high Q^2 and high x are now available [139,140] which could also shed some light on charm production processes. There is an excess in the data beyond the predictions based on standard QCD parton distribution functions. These data have been compared to calculations with intrinsic charm that enhance the standard model charm cross section [141,142] in the x and Q^2 regions of interest to the HERA excess. It was found that intrinsic charm could account for a significant enhancement over the standard model predictions in charged current scattering. More data are needed to confirm the effect and to clarify the role of charm in this region.

A nonperturbative bottom sea component in the nucleon has not been discussed here but would be a plausible extension of the models. See Ref. [126] for some predictions of intrinsic bottom effects.

4 Summary

There is only room in this review for discussion of a limited subset of all experimental results and theoretical progress towards understanding the data. For more in-depth discussion of the work described here as well as other results, the reader is encouraged to consult the appropriate references.

As discussed in this review, studies of the nucleon sea have revealed a rich structure compared to early evaluations of parton distribution functions with an SU(3) symmetric sea, *e.g.* Ref. [23]. Of these studies, the Gottfried sum rule violation, which showed that $\overline{d} > \overline{u}$, is the best documented experimentally. Interpretation of the NMC and E866 data as an indication of a cloud of virtual mesons and baryons surrounding the nucleon has proved fruitful.

Fewer data are available so far for the more massive components of the sea such as strangeness and charm. While the CCFR data suggest that a difference between the s and $\overline{s}$ distributions cannot be excluded, the distributions appear to be more strongly correlated than a kaon-hyperon cloud can accommodate. The high x and Q^2 EMC data still indicate the presence of a nonperturbative intrinsic charm component of the nucleon sea but the exact form of such a component is not fixed. In both cases, more data are needed to resolve both the origin and shape of the strange and charm contributions to the sea, particularly at large x and Q^2.

A relatively short time ago, there was a strong bias that the nucleon sea was flavor symmetric and that the quark and anti-quark distributions should be identical. These expectations have been exploded as

experiments are able to probe individual quark and anti-quark distributions more precisely. Increasingly good data and more sophisticated analysis techniques can hopefully resolve some of the issues presented here. This field is obviously very data-driven. More surprises undoubtedly await those who dive deeper into the "cloudy" depths of the nucleon sea.

Acknowledgments I would like to thank W.M. Alberico, D. Armstrong, A.O. Bazarko, S.J. Brodsky, W. Seligman, and W. Melnitchouk for discussions. I would also like to thank all the authors who provided figures for this review, including W.M. Alberico, V. Barone, A. Bodek, C. Boros, H. Christiansen, X. Ji, M. Leitch, J. Magnin, A.D. Martin, P.L. McGaughey, F. Navarra, and F.M. Steffens.

References

[1] M.N. Rosenbluth, High energy elastic scattering of electrons on protons, *Phys. Rev.* **79** (1950) 615–619; R.W. McAllister and R. Hofstadter, Elastic scattering of 188 MeV electrons from the proton and the alpha particle, *Phys. Rev.* **102** (1956) 851–856.

[2] E.D. Bloom *et al.* High-energy inelastic *ep* scattering at 6-degrees and 10-degrees, *Phys. Rev. Lett.* **23** (1969) 930–934; M. Breidenbach *et al.* Observed behavior of highly inelastic electron-proton scattering, *Phys. Rev. Lett.* **23** (1969) 935–939; J.I. Friedman and H.W. Kendall, Deep inelastic electron scattering, *Annu. Rev. Nucl. Part. Sci.* **22** (1972) 203–254.

[3] R.P. Feynman, Very high energy collisions of hadrons, *Phys. Rev. Lett.* **23** (1969) 1415–1417; J.D. Bjorken and E.A. Paschos, Inelastic electron-proton and γ-proton scattering, and the structure of the nucleon, *Phys. Rev.* **185** (1969) 1975–1982.

[4] For tabulated data before 1991 see R.G. Roberts and M.R. Whalley, Data review: a compilation of structure functions in deep inelastic scattering, *J. Phys. G* **17** D1–D151. For more recent data see the HEPDATA web page: http://cpt1.dur.ac.uk:80/HEPDATA.

[5] J. Breitweg *et al.* (ZEUS Collab.), ZEUS results on the measurement and Phenomenology of F_2 at low x and low Q^2, *Eur. Phys. J.* **C7** (1999) 609–630.

[6] A. Ahmed *et al.* (H1 Collab.), A measurement of the proton structure function $F_2(x, Q^2)$, *Nucl. Phys.* **B439** (1995) 471–502.

[7] G. Sterman *et al.* (CTEQ Collab.), Handbook of perturbative QCD, *Rev. Mod. Phys.* **67** (1995) 157–248.

[8] W. Furmanski and R. Petronzio, Lepton-hadron processes beyond leading order in quantum chromodynamics, *Z. Phys.* **C11** (1982) 293–314; T. Matsuura, R. Hamberg, and W.L. van Neerven, The contribution of the gluon-gluon subprocess to the Drell-Yan K factor, *Nucl. Phys.* **B345** (1990) 331–368; R. Hamberg, W.L. van Neerven, and T. Matsuura, A complete calculation of the order α_s^2 correction to the Drell-Yan K factor, *Nucl. Phys.* **B359** (1991) 343–405; W.L. van Neerven and E.B. Zijlstra, Order

α_s^2 contributions to the deep inelastic Wilson coefficient, *Phys. Lett.* **B272** (1991) 127–133; The $\mathcal{O}(\alpha_s^2)$ corrected Drell-Yan K factor in the DIS and $\overline{\rm MS}$ schemes, *Nucl. Phys.* **B382** (1992) 11–62; E.B. Zijlstra and W.L. van Neerven, Contribution of the second order gluonic Wilson coefficient to the deep inelastic structure function, *Phys. Lett.* **B273** (1991) 476–482; Order α_s^2 corrections to the deep inelastic proton structure functions F_2 and F_L, *Nucl. Phys.* **B383** (1992) 525–574.

[9] G. Altarelli, R.K. Ellis, and G. Martinelli, Leptoproduction and Drell-Yan processes beyond the leading approximation in chromodynamics, *Nucl. Phys.* **B143** (1978) 521–545; **B146** (1978) 544(E); Large perturbative corrections to the Drell-Yan process in QCD, *Nucl. Phys.* **B157** (1979) 461–497; J. Abad and B. Humpert, Perturbative QCD corrections in Drell-Yan processes, *Phys. Lett.* **B80** (1979) 286–289; K. Harada, T. Kaneko, and N. Sakai, Hadronic lepton pair production beyond the leading order in perturbative QCD, *Nucl. Phys.* **B155** (1979) 169–188; **B165** (1979) 545(E); J. Kubar-Andre and F.E. Paige, Gluon corrections to the Drell-Yan model, *Phys. Rev.* **D19** (1979) 221–229; B. Humpert and W.L. van Neerven, Infrared and mass regularization in AF field theories 2. QCD, *Nucl. Phys.* **B184** (1981) 225–268.

[10] S.D. Drell and T.M. Yan, Partons and their applications at high energies, *Ann. Phys.* **66** (1971) 578–623.

[11] J.C. Collins, D.E. Soper, and G. Sterman, Factorization for short distance hadron-hadron scattering, *Nucl. Phys.* **B261** (1985) 104–142; Soft gluons and factorization, *Nucl. Phys.* **B308** (1988) 833–856; Factorization of hard processes in QCD, in *Perturbative QCD*, edited by A.H. Mueller, World Scientific, (1989) 1–91; G.T. Bodwin, Factorization of the Drell-Yan cross section in perturbation theory, *Phys. Rev.* **D31** (1985) 2616–2642; erratum **D34** (1986) 3932; J. Qiu and G. Sterman, Power correction in hadronic scattering 1. leading $1/Q^2$ corrections to the Drell-Yan cross section, *Nucl. Phys.* **B353** (1991) 105–136; *ibid.*, Power correction to hadronic scattering 2. factorization, *Nucl. Phys.* **B353** (1991) 137–164.

[12] V.N. Gribov and L.N. Lipatov, Deep inelastic ep scattering in perturbation theory, *Sov. J. Nucl. Phys.* **15** (1972) 438–450; G. Altarelli and G. Parisi, Asymptotic freedom in parton language, *Nucl. Phys.* **B126** (1977) 298–318.

[13] D. Allasia *et al.* (NM Collab.), Measurement of the neutron and the proton F_2 structure function ratio, *Phys. Lett.* **B249** 366–372.

[14] A.C. Benvenuti *et al.* (BCDMS Collab.), A high statistics measurement of the proton structure functions $F_2(x, Q^2)$ and R from deep inelastic muon scattering at high Q^2, *Phys. Lett.* **B223** (1989) 485–489.

[15] E. Oltman *et al.* (CCFR Collab.), Nucleon structure functions from high energy neutrino interactions, *Z. Phys.* **C53** (1992) 51–71.

[16] J.P. Berge *et al.* (CDHSW Collab.), A measurement of differential cross sections and nucleon structure functions in charged current neutrino interactions on iron, *Z. Phys.* **C49** (1991) 187–224.

[17] H. Abramowicz *et al.* (CDHS Collab.), Experimental study of opposite sign dimuons produced in neutrino and anti-neutrino interactions, *Z. Phys.* **C15** (1982) 19–31; Neutrino and anti-neutrino charged current inclusive scattering in iron in the energy range 20 GeV< neutrino energy < 300 GeV, *Z. Phys.* **C17** (1983) 283–307.

[18] G. Quast, Electroweak review at LEP1, presented at the International Europhysics Conference on High Energy Physics, EPS-HEP99, Tampere, Finland, July 1999.

[19] J.J. Aubert *et al.* (EM Collab.), A detailed study of the proton structure functions in deep inelastic muon-proton scattering, *Nucl. Phys.* **B259** (1985) 189–265.

[20] S.A. Rabinowitz *et al.* (CCFR Collab.), Measurement of the strange sea distribution using neutrino charm production, *Phys. Rev. Lett.* **70** (1993) 134–137.

[21] C. Boros, J.T. Londergan, and A.W. Thomas, Evidence for substantial charge symmetry violation in parton distributions, *Phys. Rev. Lett.* **81** (1998) 4075–4078.

[22] A.O. Bazarko *et al.* (CCFR Collab.), Determination of the strange quark content of the nucleon from a next-to-leading order QCD analysis of neutrino charm production, *Z. Phys.* **C65** (1995) 189–198.

[23] D. Duke and J. Owens, Q^2 dependent parameterizations of parton distribution functions, *Phys. Rev.* **D30** (1984) 49–54.

[24] K. Lang *et al.* (CCFR Collab.), Neutrino production of dimuons, *Z. Phys.* **C33** (1987) 483–; C. Foudas *et al.* (CCFR Collab.), Neutrino production of opposite sign dimuons at Tevatron energies, *Phys. Rev. Lett.* **64** (1990) 1207–1210.

[25] H.L. Lai *et al.*, Global QCD analysis of parton structure of the nucleon: CTEQ5 parton distributions, *Eur. Phys. J.* **C12** (2000) 375–392.

[26] A.D. Martin, R.G. Roberts, W.J. Stirling, and R.S. Thorne, Parton distributions: a new global analysis, *Eur. Phys. J.* **C4** (1998) 463–496.

[27] M. Glück, E. Reya, and A. Vogt, Dynamical parton distributions of the proton and small x physics, *Z. Phys.* **C67** (1995) 433–448.

[28] H. Plothow-Besch, PDFLIB: A library of all available parton density functions of the nucleon, the pion and the photon and the corresponding α_s calculations, *Comp. Phys. Comm.* **75** (1993) 396–416.

[29] A.D. Martin, The partonic structure of the proton, *Acta Phys. Polon.* **B27** (1996) 1287–1308.

[30] E.A. Kuraev, L.N. Lipatov, and V.S. Fadin, The Pomeranchuk singularity in non-Abelian gauge theories, *Sov. Phys. JETP* **45** (1977) 199–204; Ya.Ya. Balitsky and L.N. Lipatov, The Pomeranchuk singularity in quantum chromodynamics, *Sov. J. Nucl. Phys.* **28** (1978) 882–829.

[31] F.E. Close, J. Qiu, and R.G. Roberts, QCD parton recombination and applications to nuclear structure functions, *Phys. Rev.* **D40** (1989) 2820–2831.

[32] L.V. Gribov, E.M. Levin, and M.G. Ryskin, Semihard processes in QCD, *Phys. Rep.* **100** (1983) 1–150.

[33] A.H. Mueller and J. Qiu, Gluon recombination and shadowing at small values of x, *Nucl. Phys.* **B268** (1986) 427–452.

[34] K. Gottfried, Sum rule for high-energy electron-proton scattering, *Phys. Rev. Lett.* **18** (1967) 1174–1177.

[35] S. Stein *et al.*, Electron scattering at 4 degrees with energies of 4.5 GeV – 20 GeV, *Phys. Rev.* **12** (1975) 1884–1919; A. Bodek *et al.*, Comparisons of deep inelastic *ep* and *en* cross sections, *Phys. Rev. Lett.* **30** (1973) 1087–1091.

[36] J.J. Aubert *et al.* (EM Collab.), Measurement of the deuteron structure function F_2 and a comparison of proton and neutron structure, *Phys. Lett.* **B123** (1983) 123–126.

[37] J.J. Aubert *et al.* (EM Collab.), Measurements of the nucleon structure functions $F_2(N)$ in deep inelastic muon scattering from deuterium and comparison with those in hydrogen and iron, *Nucl. Phys.* **B293** (1987) 740–786.

[38] P. Amaudruz *et al.* (NM Collab.), The Gottfried sum from the ratio $F_2(N)/F_2(p)$, *Phys. Rev. Lett.* **66** (1991) 2712–2715.

[39] M. Arneodo *et al.* (NM Collab.), A reevaluation of the Gottfried sum, *Phys. Rev.* **D50** (1994) R1–R3.

[40] A.D. Martin, R.G. Roberts, M.G. Ryskin, and W.J. Stirling, Consistent treatment of charm evolution in deep inelastic scattering, *Eur. Phys. J.* **C2** (1998) 287–300.

[41] E.A. Hawker *et al.* (E866 Collaboration), Measurement of the light anti-quark flavor asymmetry in the nucleon sea, *Phys. Rev. Lett.* **80** (1998) 3715–3719. The tabulated $\overline{d}/\overline{u}$ data may be found at http://p25ext.lanl.gov/e866.

[42] P.L. McGaughey, J.M. Moss, and J.C. Peng, High-Energy Hadron-Induced Dilepton Production From Nucleons and Nuclei, hep-ph/9905409, *Ann. Rev. Nucl. Part. Sci.* **49**, in press.

[43] A.D. Martin, R.G. Roberts, and W.J. Stirling, New information on parton distributions, *Phys. Rev.* **D47** (1993) 867–882.

[44] M. Arneodo, Nuclear effects in structure functions, *Phys. Rept.* **240** (1994) 301–393.

[45] B. Badelek and J. Kwiecinski, Shadowing in inelastic lepton-deuteron scattering, *Nucl. Phys.* **B370** (1992) 278–298.

[46] W. Melnitchouk and A. W. Thomas, Shadowing in deuterium, *Phys. Rev.* **D47** (1993) 3783–3793; Role of vector mesons in high Q^2 lepton-nucleon scattering, *Phys. Rev.* **D47** (1993) 3794–3803; W. Melnitchouk, A. W. Schreiber, and A. W. Thomas, Relativistic deuteron structure function, *Phys. Lett.* **B335** (1994) 11–16.

[47] S.D. Ellis and W.J. Stirling, Constraints on isospin breaking in the light quark sea from the Drell-Yan process, *Phys. Lett.* **B256** (1991) 258–264.

[48] P.L. McGaughey *et al.* (E772 Collab.), Limit on the $\overline{d}/\overline{u}$ asymmetry of the nucleon sea from Drell-Yan production, *Phys. Rev. Lett.* **69** (1992) 1726–1728.

[49] A. Baldit *et al.* (NA51 Collab.), Study of the isospin symmetry breaking in the light quark sea of the nucleon from the Drell-Yan process, *Phys. Lett.* **B332** (1994) 244–250.

[50] The definition of x_F is $x_F = (x_1 - x_2) = 2p_l/\sqrt{s}$, where p_l is the longitudinal momenta of the muon pair in the center of mass and s is the total center of mass energy squared.

[51] Distributions of kinematic variables within bins may be obtained by contacting C.N. Brown at chuckb@fnal.gov.

[52] H.L. Lai *et al.*, Improved parton distributions from global analysis of recent deep inelastic scattering and inclusive jet data, *Phys. Rev.* **D55** (1997) 1280–1296.

[53] D.A. Ross and C.T. Sachrajda, Flavor symmetry breaking in anti-quark distributions, *Nucl. Phys.* **B149** (1979) 497–516.

[54] K. Ackerstaff *et al.*, (HERMES Collab.), The flavor asymmetry of the light quark sea from semi-inclusive deep inelastic scattering, *Phys. Rev. Lett.* **81** (1998) 5519–5523.

[55] Proposal for Drell-Yan measurements of nucleon and nuclear structure with the FNAL main injector, FNAL proposal P906 (D.F. Geesaman, spokesperson).

[56] S. Kumano, Flavor asymmetry of anti-quark distributions in the nucleon, *Phys. Rept.* **303** (1998) 183–257.

[57] J.D. Sullivan, One pion exchange and deep inelastic electron-nucleon scattering, *Phys. Rev.* **D5** (1972) 1732–1737.

[58] A. Signal, A.W. Schreiber, and A.W. Thomas, Flavor SU(2) symmetry breaking in deep inelastic scattering, *Mod. Phys. Lett.* **A6** (1991) 271–276; W. Melnitchouk, A.W. Thomas, and A.I. Signal, Gottfried sum rule and the shape of $F_2^p - F_2^n$, *Z. Phys.* **A340** (1991) 85–92; A.W. Schreiber, P.J. Mulders, A.I. Signal, and A.W. Thomas, The pion cloud of the nucleon and its effect on deep inelastic scattering, *Phys. Rev.* **D45** (1992) 3069–3078; A.W. Thomas, A limit on the pionic component of the nucleon through SU(3) flavor breaking in the sea, *Phys. Lett.* **B126** (1983) 97–100; M. Ericson and A.W. Thomas, Evidence for an enhanced nuclear sea from the proton-nucleus Drell-Yan process, *Phys. Lett.* **B148** (1984) 191–193.

[59] W.Y.P. Hwang, J. Speth, and G.E. Brown, Hard form factors for meson baryon strong couplings as derived from deep inelastic lepton scattering, *Z. Phys.* **A339** (1991) 383–389; W.Y.P. Hwang and J. Speth, The origin for the violation of the Gottfried sum rule, *Phys. Rev.* **D46** (1992) 1198–1201; A. Szczurek and J. Speth, Role of meson degrees of freedom in deep inelastic lepton-nucleon scattering, *Nucl. Phys.* **A555** (1993) 249–271; B.C. Pearce, J. Speth, and A. Szczurek, Importance of the meson cloud to hadron structure, *Phys. Rept.* **242** (1994) 193–232; H. Holtmann, A. Szczurek, and J. Speth, Flavor and spin of the proton and the meson cloud, *Nucl. Phys.* **A596** (1996) 631–669.

[60] E.M. Henley and G.A. Miller, Excess of $\overline{d}$ over $\overline{u}$ in the proton sea quark distribution, *Phys. Lett.* **B251** (1990) 453–454.

[61] S. Kumano, πNN form factor for explaining sea quark distributions in the nucleon, *Phys. Rev.* **D43** (1991) 59–63; Effects of πNN form factor on pionic contributions to $\overline{u}(x)$ and $\overline{d}(x)$ distribution in the nucleon, *Phys. Rev.* **D43** (1991) 3067–3070; S. Kumano and J.T. Londergan, Origin of SU(2) flavor symmetry breaking in anti-quark distributions, *Phys. Rev.* **D44** (1991) 717–724.

[62] W. Koepf, L.L. Frankfurt, and M.I. Strikman, The nucleon's virtual meson cloud and deep inelastic lepton scattering, *Phys. Rev.* **D53** (1996) 2586–2598.

[63] W. Melnitchouk, J. Speth, and A.W. Thomas, Dynamics of light anti-quarks in the proton, **Phys. Rev. D59** (1999) 014033–10 p.

[64] K. Holinde and A.W. Thomas, One-boson-exchange potential based on a soft pion form factor, *Phys. Rev.* **C42** (1990) 1195–1199.

[65] S. Théberge and A.W. Thomas, Magnetic moments of the nucleon octet calculated in the cloudy bag model, *Nucl. Phys.* **A393** (1983) 252–282.

[66] G.A. Miller, Towards a QCD derivation of nuclear physics, *Phys. Rev.* **C39** (1989) 1563–1582; S. Kumano, Nucleon structure with pion clouds in a flux tube quark model, *Phys. Rev.* **D41** (1990) 195–202.

[67] L.L. Frankfurt, L. Mankiewicz, and M.I. Strikman, Low limit on the slope of $NN\pi$ and $N\Delta\pi$ vertex form factors from deep inelastic lepton scattering, *Z. Phys.* **A334** (1989) 343–347.

[68] J. Magnin and H.R. Christiansen, The $\overline{d}\ \overline{u}$ asymmetry of the proton in a pion cloud model approach, *Phys. Rev.* **D61** (2000) 054006 (4 pp.).

[69] F. Carvalho, F.O. Duraes, F.S. Navarra, M. Nielsen, and F.M. Steffens, Meson cloud and SU(3) symmetry breaking in parton distributions, hep-ph/9912378.

[70] R.C. Hwa, Evidence for valence quark clusters in nucleon structure functions, *Phys. Rev.* **D22** (1980) 759–764; Clustering and hadronization of quarks: a treatment of the low p_T problem, *Phys. Rev.* **D22** (1980) 1593–1608.

[71] M. Glück, E. Reya and A. Vogt, Parton distributions for high-energy collisions, *Z. Phys.* **C53** (1992) 127–134.

[72] M. Glück, E. Reya and A. Vogt, Pionic parton distributions, *Z. Phys.* **C53** (1992) 651–656.

[73] K.P. Das and R.C. Hwa, Quark-anti-quark recombination in the fragmentation region, *Phys. Lett.* **B68** (1977) 459–462; *Phys. Lett.* **B73** (1978) 504(E).

[74] R.D. Field and R.P. Feynman, Quark elastic scattering as a source of high transverse momentum mesons, *Phys. Rev.* **D15** (1977) 2590–2616.

[75] A.I. Signal and A.W. Thomas, Calculation of quark distribution functions using bag model wave functions, *Phys. Rev.* **D40** (1989) 2832–2843; F.M. Steffens and A.W. Thomas, The flavor asymmetry of the nucleon sea, *Phys. Rev.* **C55** (1997) 900–908.

[76] S.J. Brodsky and G.R. Farrar, Scaling laws for large momentum transfer processes, *Phys. Rev.* **D11** (1975) 1309–1338.

[77] E.J. Eichten, I. Hinchliffe, and C. Quigg, Flavor asymmetry in the light quark sea of the nucleon, *Phys. Rev.* **D45** (1992) 2269–2275.

[78] S. Kretzer, $SU(2)_f$ violation in the nucleon's light sea within the framework of the effective chiral quark theory, *Phys. Rev.* **D52** (1995) 2701–2708.

[79] T.P. Cheng and L.-F. Li, Chiral quark model of nucleon spin-flavor structure with SU(3) and axial-U(1) breakings, *Phys. Rev.* **D57** (1998) 344–349.

[80] A. Szczurek, A.J. Buchmann, and A. Faessler, On the flavor structure of the constituent quark, *J. Phys.* **G22** (1996) 1741–1750.

[81] J. Stern and G. Clément, Quarks, gluons, pions and the Gottfried sum rule, *Phys. Lett.* **B264** (1991) 426–431.

[82] M. Wakamatsu, Is the $q\overline{q}$ sea in the nucleon isospin symmetric?, *Phys. Rev.* **D44** (1991) R2631–R2634; The chiral quark soliton model and flavor asymmetric $q\overline{q}$ sea in the nucleon, *Phys. Rev.* **D46** (1992) 3762–3777.

[83] A. Blotz, M. Praszalowicz, and K. Goeke, Gottfried sum in the SU(3) NJL model, *Phys. Rev.* **D53** (1995) 551–554.

[84] H. Walliser and G. Holzwarth, The Gottfried sum rule in the soliton model for baryons, *Phys. Lett.* **B302** (1993) 377–380.

[85] B.-A. Li, Flavor symmetry breaking in the quark sea of the nucleon, *Nuovo Cim.* **A107** (1994) 59–68.

[86] S. Forte, The Gottfried sum rule and the light flavor content of the nucleon, *Phys. Rev.* **D47** (1993) 1842–1853.

[87] G.A. Miller, B.M.K. Nefkens, and I. Slaus, Charge symmetry, quarks and mesons, *Phys. Rept.* **194** (1990) 1–116; E.M. Henley and G.A. Miller, Meson theory of charge dependent nuclear forces, in *Mesons in Nuclei, Vol. I*, eds. M. Rho and D.H. Wilkinson, (North-Holland, Amsterdam 1979) 405–434.

[88] J.T. Londergan and A.W. Thomas, The validity of charge symmetry for parton distributions, *Prog. Part. Nucl. Phys.* **41** (1998) 49–124.

[89] E. Sather, Isospin violating quark distributions in the nucleon, *Phys. Lett.* **B274** (1992) 433–438; B.-Q. Ma, A.W. Schäfer and W. Greiner, Flavor distributions in the nucleons, SU(2) sea asymmetry or isospin symmetry breaking, *Phys. Rev.* **D47** (1993) 51–55.

[90] J.T. Londergan, S.M. Braendler, and A.W. Thomas, Testing parton charge symmetry at HERA, *Phys. Lett.* **B424** (1998) 185–190; J.T. Londergan, A. Pang, and A.W. Thomas, Probing charge symmetry violating quark distributions in semi-inclusive leptoproduction of hadrons, *Phys. Rev.* **D54** (1996) 3154–3161.

[91] E. Rodionov, A.W. Thomas, and J.T. Londergan, Charge asymmetry of parton distributions, *Mod. Phys. Lett.* **A9** (1994) 1799–1806; C.J. Benesh and J.T. Londergan, Flavor and charge symmetry in the parton distributions of the nucleon, *Phys. Rev.* **C58** (1998) 1218–1224.

[92] C. Boros, J.T. Londergan, and A.W. Thomas, Evidence for charge symmetry violation in parton distributions, *Phys. Rev.* **D59** (1999) 074021 (14 pp.).

[93] *Conceptual Design for the Relativistic Heavy Ion Collider*, BNL-52195, May, 1989, Brookhaven National Laboratory.

[94] *The LHC Conceptual Design Report–The Yellow Book*, CERN/AC/95-05, 1995, European Center for Nuclear Research (CERN).

[95] A. Bodek, Q. Fan, M. Lancaster, K.S. McFarland, and U.K. Yang, Implication of W-boson charge asymmetry measurements in $p\overline{p}$ collisions for models of charge symmetry violations in parton distributions, *Phys. Rev. Lett.* **83** (1999) 2892–2895.

[96] F. Abe *et al.*, A measurement of the lepton charge asymmetry in W boson decays produced in $p\overline{p}$ collisions, *Phys. Rev. Lett.* **81** (1998) 5754–5759.

[97] B. Mueller *et al.* (SAMPLE Collab.), Measurement of the proton's neutral weak magnetic form factor, *Phys. Rev. Lett.* **78** (1997) 3824-3827.

[98] K.A. Aniol *et al.* (HAPPEX Collab.), Measurement of the neutral weak form factors of the proton, *Phys. Rev. Lett.* **82** (1999) 1096–1100.

[99] L.A. Ahrens *et al.* Measurement of neutrino-proton and anti-neutrino-proton elastic scattering, *Phys. Rev.* **D35** (1987) 785–809.

[100] The parton distributions used in the analysis of Ref. [22] are parameterized at a reference scale μ_0^2 by $xq_{NS}(x,\mu_0^2) = A_{NS}x^{\eta_1}(1-x)^{\eta_2} + B_{NS}x^{\eta_3}$, $xq_{SI}(x,\mu_0^2) = xq_{NS}(x,\mu_0^2) + A_{\rm sea}(1-x)^{\eta_{\rm sea}}$ and $xg(x,\mu_0^2) = A_g(1-x)^{\eta_g}$, and evolved to all other values of μ^2 using the DGLAP [12] evolution equations. A_{NS} is constrained by the fermion conservation sum rule $\int \frac{dx}{x}\, xq_{NS}(x) = 3$, and A_g is constrained by the momentum sum rule $\int dx\ [xq_{SI}(x) + xg(x)] = 1$. The final fit parameter is the strong coupling constant, given by $\Lambda_{\overline{\rm MS}}$, for a total of eight fit parameters. At $\mu_0^2 = 1$ GeV^2/c^2, the parameters are $\Lambda_{\overline{\rm MS}} = 0.210 \pm 0.021$ GeV/c, $\eta_1 = 0.947 \pm 0.027$, $\eta_2 = 3.81 \pm 0.059$, $\eta_3 = 0.405 \pm 0.047$, $B_{NS} = 0.0210 \pm 0.0039$, $A_{\rm sea} = 1.404 \pm 0.047$, $\eta_{\rm sea} = 6.49 \pm 0.22$, $\eta_g = 3.18 \pm 0.70$, where the errors are statistical only.

[101] V. Barone, C. Pascaud, and F. Zomer, A new global analysis of deep inelastic scattering data, *Eur. Phys. J.* **C12** (2000) 243–262.

[102] M.J. Musolf and B.R. Holstein, Electroweak corrections to parity violating neutral current scattering, *Phys. Lett.* **B242** (1990) 461–466.

[103] D. Armstrong, private communication.

[104] P. Geiger and N. Isgur, Strange hadronic loops of the proton: A quark model calculation, *Phys. Rev.* **D55** (1997) 299–310.

[105] Mainz proposal A4/1-93 94-11 (D. von Harrach, spokesperson).

[106] TJNAF experiments E91-017 (G0 Collab., D. Beck, spokesperson); E91-004 (E.J. Beise, spokesperson).

[107] X. Ji and J. Tang, Locality of the strange sea in the nucleon, *Phys. Lett.* **B362** (1995) 182–188.

[108] A.I. Signal and A.W. Thomas, Possible strength of the nonperturbative strange sea of the nucleon, *Phys. Lett.* **B191** (1987) 205–208.

[109] S. Paiva, M. Nielsen, F.S. Navarra, F.O. Duraes, and L.L. Barz, Virtual meson cloud of the nucleon and intrinsic strangeness and charm, *Mod. Phys. Lett.* **A13** (1998) 2715–2724.

[110] H.R. Christiansen and J. Magnin, Strange/anti-strange asymmetry in the nucleon sea, *Phys. Lett.* **B445** (1998) 8–13.

[111] S.J. Brodsky and B.Q. Ma, The quark/anti-quark asymmetry of the nucleon sea, *Phys. Lett.* **B381** (1996) 317–324.

[112] W. Melnitchouk and M. Malheiro, Strangeness in the nucleon on the light cone, *Phys. Rev.* **C55** (1997) 431–440.

[113] P.J. Sutton, A.D. Martin, R.G. Roberts, and W.J. Stirling, Parton distributions for the pion extracted from Drell-Yan and prompt photon experiments, *Phys. Rev.* **D45** (1992) 2349–2359.

[114] S.J. Brodsky, P. Hoyer, C. Peterson, and N. Sakai, The intrinsic charm of the proton, *Phys. Lett.* **B93** (1980) 451–455; S.J. Brodsky, C. Peterson, and N. Sakai, Intrinsic heavy quark states, *Phys. Rev.* **D23** (1981) 2745–2757.

[115] H.L. Lai, J. Botts, J. Huston, J.G. Morfín, J.F. Owens, J.W. Qiu, W.K. Tung, and H. Weerts, Global QCD analysis and the CTEQ parton distributions, *Phys. Rev.* **D51** (1995) 4763–4782.

[116] W.M. Alberico, private communication.

[117] W.M. Alberico *et al.*, Strange form factors of the proton: a new analysis of the ν ($\overline{\nu}$) data of the BNL-734 experiment, *Nucl. Phys.* **A651** (1999) 277–286.

[118] W. Melnitchouk and M. Malheiro, Strange asymmetries in the nucleon sea, *Phys. Lett.* **B451** (1999) 224–232.

[119] M.A.G. Aivazis, J.C. Collins, F.I. Olness, and W.-K. Tung, Leptoproduction of heavy quarks: 2. a unified QCD formulation of charged and neutral current processes from fixed target to collider energies, *Phys. Rev.* **D50** (1994) 3102–3118.

[120] J.J. Aubert *et al.* (EM Collab.), Production of charmed particles in 250 GeV μ^+-iron interactions, *Nucl. Phys.* **B213** (1983) 31–64; A study of dimuon events in 280 GeV muon interactions, *Phys. Lett.* **B94** (1980) 96–100; A study of trimuon events in 280 GeV muon interactions, *Phys. Lett.* **B94** (1980) 101–105; An experimental limit on the intrinsic charm component of the nucleon, *Phys. Lett.* **B110** (1982) 73–76; M. Strovink, Review of multi-muon production by muons, in *$10^{\rm th}$ International Symposium on Lepton and Photon Interactions at High Energy* ed. W. Pfeil (Bonn, 1981) 594–622.

[121] J. Breitweg *et al.* (ZEUS Collab.), Measurement of $D^{*\pm}$ production and the charm contribution to F_2 in deep inelastic scattering at HERA, hep-ex/9908012.

[122] C. Adloff *et al.* (H1 Collab.), Inclusive D^0 and $D^{*\pm}$ production in deep inelastic ep scattering at HERA, *Z. Phys.* **C72** (1996) 593–605.

[123] K. Ackerstaff *et al.* (OPAL Collab.), Measurement of $f(c \to D^{*+}X)$, $f(b \to D^{*+}X)$ and $\Gamma_{c\overline{c}}/\Gamma_{\rm had}$ using $D^{*\pm}$ mesons, *Eur. Phys. J.* **C1** (1998) 439–459.

[124] F.M. Steffens, W. Melnitchouk, and A.W. Thomas, Charm in the nucleon, *Eur. Phys. J.* **C11** (1999) 673–683.

[125] S.J. Brodsky, P. Hoyer, A.H. Mueller, and W.-K. Tang, New QCD production mechanisms for hard processes at large x, *Nucl. Phys.* **B369** (1992) 519–542.

[126] R. Vogt and S.J. Brodsky, Intrinsic charm contribution to double quarkonium hadroproduction, *Phys. Lett.* **B349** (1995) 569–575.

[127] E. Hoffmann and R. Moore, Subleading contributions to the intrinsic charm of the nucleon, *Z. Phys.* **C20** (1983) 71–82.

[128] B.W. Harris, J. Smith, and R. Vogt, Reanalysis of EMC charm production data with extrinsic and intrinsic charm at NLO, *Nucl. Phys.* **B461** (1996) 181–196.

[129] E. Laenen, S. Riemersma, J. Smith, and W.L. van Neerven, Complete $\mathcal{O}(\alpha_s)$ corrections to heavy flavor structure functions in electroproduction, *Nucl. Phys.* **B392** (1993) 162–228.

[130] http://durpdg.dur.ac.uk/HEPDATA.

[131] B.W. Harris and J. Smith, Heavy quark correlations in deep inelastic electroproduction, *Nucl. Phys.* **B452** (1995) 109–160; B.W. Harris and J. Smith, Invariant mass distributions for heavy quark-anti-quark pairs in deep inelastic electroproduction, *Phys. Lett.* **B353** (1995) 535–540; *Phys. Lett.* **B359** (1995) 423(E).

[132] A.D. Martin, R.G. Roberts, and W.J. Stirling, Pinning down the glue in the proton, *Phys. Lett.* **B354** (1995) 155–162.

[133] R. Vogt, S.J. Brodsky, and P. Hoyer, Systematics of J/ψ production in nuclear collisions, *Nucl. Phys.* **B360** (1991) 67–96.

[134] R. Vogt, S.J. Brodsky, and P. Hoyer, Systematics of charm production in hadronic collisions, *Nucl. Phys.* **B383** (1992) 643–684.

[135] R. Vogt and S.J. Brodsky, Charmed hadron asymmetries in the intrinsic charm coalescence model, *Nucl. Phys.* **B478** (1996) 311–334.

[136] T. Gutierrez and R. Vogt, Leading charm in hadron nucleus interactions in the intrinsic charm model, *Nucl. Phys.* **B539** (1999) 189–214.

[137] M. Neubert, Heavy quark symmetry, *Phys. Rep.* **245** (1994) 259–396.

[138] M. Glück, E. Reya, and A. Vogt, Dynamical parton distributions revisited, *Eur. Phys. J.* **C5** (1998) 461–470.

[139] C. Adloff *et al.* (H1 Collab.), Observation of events at very high Q^2 in ep collisions at HERA, *Z. Phys.* **C74** (1997) 191–206.

[140] J. Breitweg *et al.* (ZEUS Collab.), Comparison of ZEUS data with standard model predictions for $e^+p \to e^+X$ scattering at high x and Q^2, *Z. Phys.* **C74** (1997) 207–220.

[141] J.F. Gunion and R. Vogt, Intrinsic Charm at High Q^2 and HERA Data, LBNL-40399, UCD-97-14, hep-ph/9706252.

[142] W. Melnitchouk and A.W. Thomas, HERA anomaly and hard charm in the nucleon, *Phys. Lett.* **B414** (1997) 134–139.